

VILNIUS UNIVERSITY

CENTER FOR PHYSICAL SCIENCES AND TECHNOLOGY

Jonas Klevas

THE INFLUENCE OF CONVECTION  
AND NON-LOCAL RADIATIVE FIELD  
ON SPECTRAL LINE FORMATION IN STELLAR ATMOSPHERES

Doctoral Dissertation

Physical sciences, Physics (02 P)

Vilnius, 2017

Doctoral Dissertation was completed during 2012–2017 at Vilnius University.

Scientific supervisor:

Dr. Arūnas Kučinskas (Vilnius University, Physical sciences,  
Physics – 02 P)

VILNIAUS UNIVERSITETAS

FIZINIŲ IR TECHNOLOGIJOS MOKSLŲ CENTRAS

Jonas Klevas

KONVEKCIJOS  
IR NELOKALIAUS SPINDULIUOTĖS LAUKO  
ĮTAKA SPEKTRO LINIJŲ FORMAVIMUISI ŽVAIGŽDŽIŲ ATMOSFEROSE

Daktaro disertacija

Fiziniai mokslai, fizika (02 P)

Vilnius, 2017

Disertacija rengta 2012–2017 metais Vilniaus universitete.

Mokslinis vadovas:

Dr. Arūnas Kučinskas (Vilniaus universitetas, fiziniai mokslai,  
fizika – 02 P)

## Abstract

In this dissertation spectral line formation in stellar atmospheres is explored, focusing on the interplay between convection, radiative transfer, and spectral line formation. For this purpose we use three-dimensional (3D) hydrodynamical CO<sup>5</sup>BOLD model atmospheres, which allow to model convection in an explicit way.

As a first step in this investigation, we studied the influence of convection on the asymmetries and Doppler shifts of Fe I spectral lines in the metal-poor red giant HD 122563. In general, a good agreement between the theoretically predicted and observed Doppler shifts of Fe I line cores was found, with somewhat larger discrepancies seen in the cases of weaker (equivalent width  $W < 5$  pm) and stronger lines ( $W > 11$  pm).

Next, we investigated the influence of convection on the formation of spectral lines in the atmospheres of red giant stars. For this, we used model atmospheres with the parameters similar to red giants located at the tip and bottom of the RGB. For the giant located at the RGB tip ( $T_{\text{eff}} = 3660$  K,  $\log g = 1.0$ ,  $[M/H] = 0.0$ ), we studied weak fictitious spectral lines of Li I, Na I, Mg I, Mg II, and K I. While the 3D–1D abundance corrections for the neutral species were found to be small, at the level of  $\approx \pm 0.1$  dex, the corrections for Mg II spanned over the range between +0.2 dex and –0.6 dex, with the extreme values corresponding to the transitions originating at the highest atomic energy levels investigated (10 eV).

For giants located at the lower part of the RGB ( $T_{\text{eff}} = 5000$  K,  $\log g = 2.5$ ,  $[M/H] = 0.0, -1.0, -2.0, -3.0$ ), we studied the formation of weak fictitious lines of Li I, Na I, Mg I, Mg II, K I, Ca I, and Ca II. At  $[M/H] = 0.0$ , 3D–1D abundance corrections for neutral species are of the same order as for the giant located at the RGB tip and do not exceed  $\approx \pm 0.1$  dex. For the ionized species 3D–1D corrections are in the same range. However, the magnitude of 3D–1D corrections for neutral species changes with metallicity and generally becomes largest (in its absolute value) at the lowest metallicity. For example, in the extreme case of Mg I, the 3D–1D abundance correction is equal to –0.7 dex at  $[M/H] = -3.0$ .

We also investigated the influence of convection and non-local thermodynamic equilibrium (NLTE) radiative transfer on the formation of resonance Li I doublet ( $\lambda = 670.8$  nm) in the atmospheres of main sequence (MS), main sequence turn-off (TO), subgiant branch (SGB), and RGB stars, all at two metallicities,  $[M/H] = 0.0$  and  $-2.0$ . This investigation was carried out using 3D hydro-

dynamical CO<sup>5</sup>BOLD and 1D hydrostatic LHD model atmospheres, with 3D NLTE spectral synthesis calculations performed using NLTE3D code and the new model atom of Li I that was constructed for this purpose during the course of this study. In general, convection was found to play significant role in the spectral line formation, mostly by strengthening of lines due to horizontal inhomogeneities of Li I number densities in the stellar atmosphere. At the same time, we found that non-equilibrium radiative transfer, due to overionization of Li I, may lead to the formation of Li I lines that are significantly weaker than those that would be forming in a given stellar atmosphere in LTE. Overall, the 3D NLTE–1D LTE abundance corrections for the resonance Li I line in the spectra of MS, TO, SGB and RGB stars were found to be  $-0.06$  to  $+0.27$  dex.

## **Acknowledgments**

First of all, I would like to thank my supervisor Arūnas Kučinskas, without whose guidance this dissertation would not have seen the light and I would not have given a go at a scientific path.

Secondly, I would like to thank my senior co-authors and colleagues H. -G. Ludwig, M. Steffen, P. Bonifacio, E. Caffau, S. Korotin, L. Mashonkina, V. Tsymbal, V. Vansevičius, G. Tautvaišienė and numerous others who helped me shape my growth.

I would also like to thank my colleagues G. Valiauga, V. Dobrovolskas, D. Prakapavičius, A. Černiauskas and others for having me working with them.

I would also like to acknowledge all of those people, who may never read this work, but nevertheless significantly helped me completing it, including but not limited to my family and friends.

## **Abbreviations**

1D – one-dimensional

3D – three-dimensional

LTE – local thermodynamic equilibrium

MS – main sequence

NLTE – non-local thermodynamic equilibrium

RGB – red giant branch

SGB – subgiant branch

TO – main sequence turn-off point

# Contents

<b>Introduction</b>	<b>11</b>
Motivation . . . . .	11
Aims of the study . . . . .	15
Main tasks . . . . .	15
Results and statements to defend . . . . .	15
Novelty . . . . .	16
Publications on the Thesis topic in in the Clarivate Analytics WoS journals . . . . .	17
Other publications in the Clarivate Analytics WoS journals . . . . .	17
Presentations at the conferences . . . . .	18
Personal contribution . . . . .	19
Thesis outline . . . . .	20
<b>1 Stellar model atmospheres</b>	<b>21</b>
1.1 3D hydrodynamical CO <sup>5</sup> BOLD model atmospheres . . . . .	22
1.1.1 3D hydrodynamical models . . . . .	22
1.1.2 Averaged ⟨3D⟩ models . . . . .	24
1.2 1D hydrostatic LHD model atmospheres . . . . .	25
<b>2 Spectral line synthesis</b>	<b>27</b>
2.1 3D/1D NLTE/LTE spectral line synthesis with the Linfor3D code . . . . .	27
2.2 3D NLTE software package NLTE3D . . . . .	28
2.2.1 3D NLTE spectral line sythesis . . . . .	28
2.2.2 Model atom of lithium . . . . .	29
<b>3 The influence of convection on spectral line asymmetries and shifts</b>	<b>33</b>
3.1 Observed spectrum of HD 122563 . . . . .	34
3.2 3D hydrodynamical CO <sup>5</sup> BOLD model atmospheres and spectral line synthesis . . . . .	34
3.3 Line asymmetry measurements . . . . .	35
3.4 Results and discussion . . . . .	36
<b>4 The influence of convection on spectral line strength</b>	<b>41</b>
4.1 Line strength under the influence of convection in the atmosphere of a star located at the RGB tip . . . . .	41
4.1.1 Model atmospheres and spectral line synthesis . . . . .	42
4.1.2 3D–1D abundance corrections . . . . .	45
4.1.3 The influence of thermodynamical structure of atmosphere on spectral line formation . . . . .	46
4.2 Line strength under the influence of convection in the atmospheres of stars located in the lower part of RGB . . . . .	53
4.2.1 Model atmospheres and spectral line synthesis . . . . .	53

4.2.2	The influence of thermodynamical structure of atmosphere on spectral line formation . . . . .	56
<b>5</b>	<b>The influence of convection and non-equilibrium radiative transfer on the formation of Li I 670.8 nm resonance doublet</b>	<b>65</b>
5.1	Model atmospheres and spectral line synthesis . . . . .	65
5.2	The influence of convection and NLTE effects on the strength of Li I 670.8 nm resonance doublet . . . . .	68
5.3	The influence of scattering on the Li I 670.8 nm resonance doublet strength . . . . .	75
	<b>Summary and conclusions</b>	<b>79</b>
	<b>References</b>	<b>81</b>
	<b>Appendix A. Selecting a representative snapshot subsample of 3D hydrodynamical model atmospheres</b>	<b>87</b>
	<b>Appendix B. Atomic data for the model atom of Li</b>	<b>91</b>

# Introduction

## Motivation

Convection is an important physical phenomenon responsible for the energy transport in stellar atmospheres and interiors. In cool stars (such as the Sun), convection zone may reach close to (or even into) the atmospheric layers where formation of spectral lines takes place, and therefore may directly influence line strengths, shapes, and Doppler shifts. A direct imprint of convection is the granulation pattern seen on the surface of the Sun, which is comprised of hot rising granules and cooler intergranular downflows. Granulation cannot be directly resolved in other stars yet, with the exception of the nearest supergiants, such as Betelgeuse (e.g., Kervella et al. 2009), therefore it can be only detected indirectly, for example, through the analysis of line asymmetries and their Doppler shifts.

To interpret the observed stellar spectra one has to rely on stellar model atmospheres. Inevitably, the confidence with which one can derive chemical composition (or other properties) of real stars is determined by the accuracy and physical realism of the model atmospheres that are used in the analysis of observed data. Classical 1D model atmospheres are the most widely used for such tasks today. Stellar atmospheres in these models are treated as static and one-dimensional, thus the resulting model structures are functions of the radial coordinate alone. Convection in such models is usually described using the mixing-length theory (MLT; see, e.g., Böhm-Vitense 1958), with a number of free parameters that have to be set *a priori*, such as the mixing-length parameter,  $\alpha_{\text{MLT}}$ . Due to their static 1D nature and various simplifications involved, such models are fast to compute, which allowed large model grids to be produced using a variety of 1D model atmosphere codes, such as ATLAS9 (Castelli & Kurucz 2003), MARCS (Gustafsson et al. 2008), and PHOENIX (Brott & Hauschildt 2005), for various combinations of stellar atmosphere parameters. Despite numerous simplifications, 1D model atmospheres have aided in gaining enormous amount of information about the processes taking place in stellar atmospheres and their deeper interiors.

Nevertheless, convection in its nature is not homogeneous and therefore convective stellar atmospheres are not expected to be such either. To account for

both spatial and temporal inhomogeneity of a stellar atmosphere, one has to add one or two horizontal dimensions that are missing in 1D hydrostatic model atmospheres. This makes the task of modeling a stellar atmosphere significantly more difficult, with a result of a rather slow advance in application of such model atmospheres in the studies of stars, even though theoretical basis for computation of such model atmospheres is already available for more than a few decades. The past decade, however, has seen a sharp increase in the application of 3D hydrodynamical model atmospheres in the field of stellar astrophysics (see, e.g., Asplund et al. 2000; Caffau et al. 2008; González Hernández et al. 2009; Behara et al. 2010). This growing interest stems from the discovery that classical 1D and 3D hydrodynamical model atmospheres used in the elemental abundance analysis predict significantly different stellar compositions, especially at lower metallicities. For certain elements, these differences may be as large as  $-1.0$  dex (see, e.g., Collet et al. 2007; Dobrovolskas et al. 2010; Ivanauskas et al. 2010). This shows that our knowledge of convection applied to the study of stars in the Galaxy and beyond may be inaccurate and therefore may impart various implications regarding our knowledge about stellar populations, Galaxy, and the history of Universe at large.

Red giants are amongst the brightest objects in the intermediate age and old stellar populations. They may therefore provide us with the information about stellar populations that would be not accessible via analysis of fainter stars, such as those located on the MS or TO. Thus, to accurately interpret the observations, understanding the role of convection in these stars is crucial. For this, 3D hydrodynamical model atmospheres may be particularly useful. There are very few studies of these stars with 3D hydrodynamical model atmospheres, however Kučinskis et al. (2005) have shown that convection may significantly influence thermal structure of the red giant atmosphere which may affect its observed spectral energy distribution. This may result in a difference of  $\sim 0.2 - 0.3$  mag in the broad-band photometric colors predicted by 3D hydrodynamical and classical 1D model atmospheres. Collet et al. (2007) showed that red giants ( $T_{\text{eff}} \approx 4700 - 5100$  K,  $\log g = 2.2$ ,  $[\text{Fe}/\text{H}] = 0.0$  to  $-3.0$ ) may have significantly different thermal structures depending on how convection is accounted for, especially at lowest metallicities. This may lead to differences of up to  $-1.0$  dex in the abundances of chemical elements derived with the 3D hydrodynamical and classical 1D model atmospheres. These studies were later extended by Dobrovolskas et al. (2010) and Ivanauskas et al. (2010), who inves-

tigated spectral line formation in the red giant atmospheres using considerably larger samples of chemical elements. These results suggest, that convection may significantly influence internal structure of the red giant atmospheres, as well as their observable properties, therefore requiring further, more detailed studies.

Another important physical phenomenon that needs to be considered when modeling stellar atmospheres and their emergent radiation field is that spectral lines in stellar atmospheres frequently form in the conditions that may deviate significantly from the LTE. This is normally taken into account by solving statistical equilibrium equations coupled with NLTE radiative transfer computations. Fortunately, except for the hottest stars, NLTE effects have relatively minor influence on thermal structure of the model atmospheres (e.g., Short & Hauschildt 2006). However, in many cases NLTE treatment in the computation of synthetic spectral line profiles becomes important, especially at lower metallicities where NLTE effects may be significant (see, e.g., Asplund et al. 2005, for a review). So far, however, attempts to include NLTE effects have been mostly limited to 1D hydrostatic model atmospheres.

It would therefore be desirable if abundances of chemical elements in stellar atmospheres could be derived using the full 3D NLTE approach, i.e., with NLTE spectral synthesis computations performed using 3D hydrodynamical model atmospheres, which would be the most realistic way to model spectral line formation. This, however, has rarely been possible until now since the majority of current spectral synthesis codes lack the capability to perform statistical equilibrium computations in 3D NLTE, even though several successful steps in this direction have already been made, with more very likely to come in the near future (see, for example, Asplund et al. 2003, 2004; Cayrel et al. 2007; Steffen et al. 2010, 2012; Lind et al. 2012, 2013; Holzreuter & Solanki 2013; Prakashavičius et al. 2013; Steffen et al. 2015; Amarsi et al. 2016). Frequently then, various simplifications are still used to substitute for the full 3D NLTE approach. For example, sometimes elemental abundances are derived in 1D NLTE and subsequently corrected for the 3D hydrodynamical effects, with the size of these 3D–1D abundance corrections evaluated under the assumption of LTE (3D+NLTE approach); or average  $\langle 3D \rangle$  model atmospheres are used with the standard 1D NLTE analysis tools. However, since the properties of spectral line formation in full 3D NLTE are still poorly explored, many details of the interaction between hydrodynamical and NLTE effects in 3D are still unknown. Therefore, it is not clear at all whether such strategies may be generalized to substitute for the full 3D NLTE

computations.

Studies based on 3D NLTE methodology are even more computationally demanding than those carried out in 3D LTE. Since the model atoms with smaller number of electrons have less complex networks of both radiative and non-radiative transitions, it is reasonable to investigate lightest chemical elements first. One of potentially very interesting candidates is lithium. Lithium is an important cosmological tracer element and one way of measuring its primordial (cosmological) abundance is using stellar spectra (mostly of MS, TO, and sub-giant branch SGB stars; it is possible though, that red giant branch RGB stars may be useful, too: see, for example, Mucciarelli et al. 2012). However, lithium spectral line formation is known to be prone to both 3D hydrodynamical and NLTE effects, and it is thought that these effects typically tend to work in opposite directions in stellar atmospheres, at least in those of MS and SGB stars. This leads to generally small 3D NLTE abundance corrections (Asplund et al. 2003; Steffen et al. 2010). Nevertheless, it is still not entirely clear whether less sophisticated tools/approaches could be used in the case of lithium to circumvent the full 3D NLTE calculations, which are still computationally expensive and less accessible to wider astronomical community.

To summarize, convection in stellar atmospheres is still poorly understood. From the theoretical side, 3D hydrodynamical model atmospheres, while realistically accounting for convection, are still expensive computationally, resulting in few applications in studies of convection in stellar atmospheres. Currently, applications of 3D hydrodynamical model atmospheres provided new insights about the nature of convection and its role in shaping the observable properties of different types of stars. However, one would want to combine 3D hydrodynamical models with non-equilibrium radiative transfer to model line formation more realistically and to understand the interplay between the two processes better. This is an even more computationally demanding task, thus the combined role of both 3D hydrodynamical and NLTE effects in stellar atmospheres still remains essentially unexplored.

## Aim of the study

The goal of this work was to study the influence of convection and non-local radiation field on the spectral line formation in stellar atmospheres.

## Main tasks

1. Using 3D–1D LTE abundance corrections, investigate the influence of convection on the formation of spectral lines of Li I, Na I, Mg I, Mg II, Al I, K I, Ca I, Ca II in the atmospheres of red giant stars.
2. Study the influence of convection and non-equilibrium radiative transfer on the formation of Li I 670.8 nm resonance doublet in the atmospheres of main sequence, subgiant branch, and red giant branch stars.

## Results and statements to defend

1. Differences between the coreshifts of medium strength Fe I lines ( $5 \text{ pm} < W < 11 \text{ pm}$ ) observed in spectrum of the metal-poor red giant HD 122563 and those predicted using 3D hydrodynamical model atmosphere of this star range from  $-0.21$  to  $+0.33$  km/s. Mean difference is  $+0.015 \pm 0.076$  km/s (the error is standard deviation).
2. The 3D–1D LTE abundance corrections for the spectral lines of Li I, Na I, Mg I, Al I, and K I calculated using 3D hydrodynamical model atmosphere with  $T_{\text{eff}} = 3600$  K,  $\log g = 1.0$  [cgs],  $[M/H] = 0.0$  are not significant and do not exceed  $\pm 0.06$  dex.
3. The 3D–1D LTE abundance corrections for the spectral lines of Mg II calculated using 3D hydrodynamical model atmosphere with  $T_{\text{eff}} = 3600$  K,  $\log g = 1.0$  [cgs],  $[M/H] = 0.0$  range from  $-0.08$  dex at  $\chi = 0.0$  eV to  $-0.42$  dex at  $\chi = 10.0$  eV.
4. The 3D–1D LTE abundance corrections for the spectral lines of Li I, Na I, Mg I, Al I, K I, and Ca I calculated using 3D hydrodynamical model atmosphere with  $T_{\text{eff}} = 5000$  K,  $\log g = 2.5$  [cgs],  $[M/H] = 0.0$  are not significant and do not exceed  $\pm 0.06$  dex.
5. Spectral lines of Li I, Na I, Mg I, Al I, K I, Ca I calculated with 3D hydrodynamical CO<sup>5</sup>BOLD model atmospheres  $T_{\text{eff}} = 5000$  K,  $\log g = 2.5$  [cgs],

$[M/H] = 0.0, -1.0, -2.0, -3.0$  were used to obtain 3D–1D LTE abundance corrections, which increase in magnitude with decreasing metallicity. In case of Mg I ( $\chi = 0.0$  eV,  $\lambda = 850$  nm) they change from  $-0.02$  dex ( $[M/H] = 0.0$ ) to  $-0.78$  dex ( $[M/H] = -3.0$ ).

6. The 3D–1D LTE abundance corrections for the spectral lines of Mg II and Ca II calculated using 3D hydrodynamical model atmospheres of red giants with  $T_{\text{eff}} = 5000$  K,  $\log g = 2.5$  [cgs],  $[M/H] = 0.0, -1.0, -2.0, -3.0$  do not exceed  $\pm 0.12$  dex.
7. The 3D NLTE–1D LTE abundance corrections for the Li I 670.8 nm resonance doublet calculated using the model atmospheres with  $4500 \leq T_{\text{eff}} \leq 6500$  K,  $2.5 \leq \log g \leq 4.5$  [cgs],  $[M/H] = 0.0, -2.0$  range from  $+0.27$  dex ( $T_{\text{eff}} = 4480$  K,  $\log g = 2.5$  [cgs],  $[M/H] = 0.0$ ) to  $-0.06$  dex ( $T_{\text{eff}} = 6320$  K,  $\log g = 4.5$  [cgs],  $[M/H] = -2.0$ ). Abundance corrections at solar metallicity are larger than those obtained at  $[M/H] = -2.0$ .
8. A set of 3D NLTE–1D LTE abundance corrections for the Li I 670.8 nm resonance doublet was computed using the model atmospheres with  $4500 \leq T_{\text{eff}} \leq 6500$  K,  $2.5 \leq \log g \leq 4.5$  [cgs],  $[M/H] = 0.0, -2.0$  (16 combinations of atmospheric parameters).

## Novelty

Research done in this Thesis is new in several key aspects which are listed below:

1. 3D hydrodynamical model atmospheres were applied to investigate the influence of convection on the formation of spectral lines of different neutral and ionized atoms, for the first time for Mg II, Al I, K I.
2. The influence of convection and non-equilibrium radiative transfer on the formation of Li I 670.8 nm resonance doublet in the atmospheres of main sequence, subgiant branch, and red giant branch stars was investigated for the first time. For this, we used a new model atom of Li which was constructed using state-of-the-art atomic data. In terms of the number of atomic levels and transitions taken into account in the computations of population densities, this is presently one of the most complex model atom of lithium available for 3D NLTE spectral line synthesis computations.

3. The role of scattering in the formation Li I 670.8 nm resonance doublet under the presence of convection and non-local equilibrium radiation field was studied for the first time with the aid of 3D hydrodynamical model atmospheres.

## Publications on the Thesis topic in in the Clarivate Analytics WoS journals

1. **Klevas, J.**, Kučinskas, A., Steffen, M., Caffau, E., Ludwig, H.-G. 2016, *Lithium spectral line formation in stellar atmospheres. The impact of convection and NLTE effects* // *Astronomy and Astrophysics*, 586, A156.
2. Dobrovolskas, V., Kučinskas, A., **Klevas, J.**, Caffau, E., Ludwig, H.-G., Steffen, M. 2013, *Three-dimensional hydrodynamical CO<sup>5</sup>BOLD model atmospheres of red giant stars III. Line formation in the atmospheres of giants located close to the base of RGB* // *Astronomy and Astrophysics*, 559, A102.
3. Kučinskas, A., Steffen, M., Ludwig, H.-G., Dobrovolskas, V., Ivanauskas, A., **Klevas, J.**, Prakupavičius, D., Caffau, E., Bonifacio, P. 2013, *Three-dimensional hydrodynamical CO<sup>5</sup>BOLD model atmospheres of red giant stars. II. Spectral line formation in the atmosphere of a giant located near the RGB tip* // *Astronomy and Astrophysics*, 549, A14.

## Other publications in the Clarivate Analytics WoS journals

1. Prakupavičius, D., Kučinskas, A., Dobrovolskas, V., **Klevas, J.**, Bonifacio, P., Ludwig, H.-G., Steffen, M., Spite, M. *Three-dimensional hydrodynamical CO<sup>5</sup>BOLD model atmospheres of red giant stars V. Oxygen abundance in the metal-poor giant HD 122563 from OH UV lines* // *Astronomy and Astrophysics*, 599, A128.
2. Černiauskas, A., Kučinskas, A., **Klevas, J.**, Dobrovolskas, V., Prakupavičius, D., Korotin, S., Bonifacio, P., Ludwig, H.-G., Caffau, E., Steffen, M. *Abundances of Na, Mg, and K in the atmospheres of red giant branch stars of Galactic globular cluster 47 Tucanae* // *Astronomy and Astrophysics*, 604, A35.
3. Wedemeyer, S., Kučinskas, A., **Klevas, J.**, Ludwig, H.-G. *Three-dimensional hydrodynamical CO<sup>5</sup>BOLD model atmospheres of red giant stars VI. First chromosphere model of a late-type giant* // *Astronomy and Astrophysics*, spaudoje, DOI: <https://doi.org/10.1051/0004-6361/201730405>.

## Presentations at the conferences

1. **Klevas, J.**, Kučinskas, A., Prakupavičius, D., *CO<sup>5</sup>BOLD simulations across the HR diagram // "CO<sup>5</sup>BOLD Workshop 2016"*. Napoli, Italy, 11–13 April, 2016, *Memorie della Societa Astronomica Italiana*, 88, 100 (oral presentation).
2. Prakupavičius, D., Steffen, M., **Klevas, J.**, Kučinskas, A. *Non-LTE spectral line synthesis with CO<sup>5</sup>BOLD model atmospheres // "CO<sup>5</sup>BOLD Workshop 2016"*. Napoli, Italy, 11–13 April, 2016, *Memorie della Societa Astronomica Italiana*, 88, 77 (oral presentation by D. Prakupavičius).
3. **Klevas, J.**, Kučinskas, A., Ludwig, H.-G., Bonifacio, P., Steffen, M., Prakupavičius, D., *Predicting Asymmetries And Shifts Of Spectral Lines In The Metal-Poor Red Giant HD 122563 Spectrum // Open Readings 2013*, Vilnius, 20–23 March, 2013, Programa ir pranešimų tezės, Vilniaus universitetas, 164 p. (poster presentation).
4. **Klevas, J.**, Kučinskas, A., Ludwig, H.-G., Bonifacio, P., Steffen, M., Prakupavičius, D., *Velocity fields in the atmosphere of the metal-poor red giant HD 122563 // 40th Lithuanian National Physics Conference*, Vilnius, 10–12 June, 2013, Programa ir pranešimų tezės, Vilniaus universitetas, 240 p. (poster presentation).
5. **Klevas, J.**, Kučinskas, A., Ludwig, H.-G., Bonifacio, P., Steffen, M., Prakupavičius, D., *Spectral line asymmetries in the metal-poor red giant HD 122563: CO<sup>5</sup>BOLD predictions versus observations // "CO<sup>5</sup>BOLD Workshop 2012"*, Heidelberg, Germany, 01–03 October, 2012, *Memorie della Societa Astronomica Italiana Supplementi*, 24, 78 (oral presentation).
6. Kučinskas, A., Ludwig, H.-G., Steffen, M., Dobrovolskas, V., **Klevas, J.**, Prakupavičius, D., Caffau, E., Bonifacio, P., *The influence of convection on the atmospheric structures and observable properties of red giant stars // "CO<sup>5</sup>BOLD Workshop 2012"*, Heidelberg, Germany, 01–03 October, 2012, *Memorie della Societa Astronomica Italiana Supplementi*, 24, 68 (oral presentation by A. Kučinskas).

## Personal contribution

The author has performed all 3D/1D LTE spectral line synthesis computations used in this work, which included: Fe I lines used in the study of spectral line shifts/asymmetries in HD 122563 (Chapter 3); Li I, Na I, Mg I, Mg II, Al I, K I for a model red giant at the RGB tip (Chapter 4.1); Li I, Na I, Mg I, Mg II, Al I, K I, Ca I, Ca II for the four model red giants at the lower part of the RGB (Chapter 4.2); and Li I spectral lines for main sequence, subgiant and red giant stars in 3D/1D NLTE/LTE (Chapter 5). Using both theoretical and observed Fe I lines of HD 122563, the author has measured their coreshifts and bisectors and analyzed both theoretical and observed data. Results were presented at three international conferences (third, fourth and fifth entries in the list given in the Section “Presentations at the conferences”; co-authors of this study contributed to the developing of methodology, computed 3D hydrodynamical model atmospheres, and took part in analysis of the results). For the analysis of spectral line formation in the atmospheres of RGB stars, the author computed 3D–1D abundance corrections and analyzed part of the results. The findings of this study were presented in two scientific papers, Kučinskas et al. (2013) and Dobrovolskas et al. (2013), second and third entries in the list given in the Section “Publications on the Thesis topic in in the Clarivate Analytics WoS journals”. Co-authors of these papers developed methodology of the study, calculated the model atmospheres used in this work, performed spectral line synthesis calculations, and calculated abundance corrections for other chemical elements not discussed in this Thesis, performed analysis of the obtained results. The author has computed theoretical Li I 670.8 nm resonance doublet profiles in 3D/1D NLTE/LTE using the model atmospheres of main sequence, subgiant and red giant stars. To achieve this, the author has compiled a new model atom of Li I and computed departure coefficients for the NLTE calculations of the Li I 670.8 nm resonance doublet. Using these line profiles, the author has calculated all abundance corrections used in this study. The results were summarized in Klevas et al. (2016), the first entry in the list given in the Section “Publications on the Thesis topic in in the Clarivate Analytics WoS journals”. Together with the co-authors, the author has investigated the influence of convection and non-equilibrium radiative transfer on the formation of Li I 670.8 nm resonance doublet. With the co-authors, the author has developed a method for the automated selection of snapshots of the 3D hydrodynamical model atmospheres for spectral line synthesis computations.

## Thesis outline

The dissertation consists of **Introduction**, five **Chapters**, **Conclusions**, and **References**.

In **Chapter 1** stellar model atmospheres used in this work are described.

In **Chapter 2** spectral synthesis packages used in this work are introduced.

In **Chapter 3** are presented the results obtained during the investigation of the spectral line formation in the atmosphere of a metal-poor red giant HD 122563, focusing on the impact of convection on the asymmetries and Doppler shifts of Fe I lines. These results were presented at three international conferences and were published in their proceedings.

In **Chapter 4** we describe the results obtained during the investigation of spectral line formation in the atmospheres of red giant stars, focusing on the impact of convection on the spectral line strengths. These results were published in Dobrovolskas et al. (2013) and Kučinskas et al. (2013), the second and third papers in the publication list presented in Section "Publications on the Thesis topic in in the Clarivate Analytics WoS journals" above.

In **Chapter 5** we describe results that were obtained in the study of the influence of convection and NLTE radiative transfer on the formation of Li I 670.8 nm resonance doublet in stellar atmospheres accross the HR diagram. These results were published in Klevas et al. (2016), the first paper in the publication list presented in Section "Publications on the Thesis topic in in the Clarivate Analytics WoS journals" above.

## Chapter 1

# Stellar model atmospheres

Radiation emitted by the stellar atmospheres can be observed directly because in these layers stars become optically thin. However, to understand the physical conditions in the radiation forming layers, and the star itself, one has to rely on theoretical modeling. In the first approximation, the star can be assumed to radiate as a black body. This can roughly explain the shape of stellar spectral energy distribution, as well as may help to define a black body temperature to characterize the star. However, to infer anything beyond this, one has to construct much more detailed model atmosphere which would allow to predict how the radiation is forming in its layers. Also, stellar atmosphere consists of different chemical species, which affect the observed spectrum by redistributing spectral energy via ionization/recombination, absorption/emission in spectral lines, free-free absorption, and scattering. Therefore, in order to understand the properties of real stars, realistic theoretical model atmospheres need to be constructed beforehand.

Model atmospheres, that are most widely used today assume homogeneity of the hydrostatic atmosphere, either plane-parallel or spherically-symmetric, and therefore are known as 1D model atmospheres. Outside several special cases, such as pulsating stars, 1D model atmospheres are assumed to be hydrostatic. However, assumption of their 1D hydrostatic nature conflicts with the nature of convection which is inhomogeneous and dynamic. These inconsistencies can be tackled by using more realistic 3D hydrodynamical model atmospheres, the first of which appeared about three decades ago. Unfortunately, this approach is significantly more computationally expensive, therefore 3D hydrodynamical model atmospheres are still less prevalent than their classic 1D hydrostatic counterparts. To investigate the role of convection, 3D hydrodynamical CO<sup>5</sup>BOLD (Freytag et al. 2012) model atmospheres and 1D hydrostatic LHD (Caffau et al. 2008) model atmospheres were used in this study.

Further in this Chapter we therefore outline the details regarding the construction and computation of both 3D hydrodynamical and 1D hydrostatic model atmospheres used in this Thesis.

## 1.1 3D hydrodynamical CO<sup>5</sup>BOLD model atmospheres

### 1.1.1 3D hydrodynamical models

CO<sup>5</sup>BOLD (COnservative COde for the COmputation of COmpressible COnvection in a BOx of L Dimensions, L = 2, 3) model atmospheres computation package (Freytag et al. 2012) used in this work solves coupled non-linear equations of compressible hydrodynamics in an external gravitational field, coupled with radiative transfer. The CO<sup>5</sup>BOLD code uses a Riemann solver of Roe type to calculate the time evolution of the hydrodynamical flow and the radiation field on a 3D Cartesian grid. Hydrodynamical equations consist of mass conservation, momentum conservation, and energy conservation, as follows:

$$\frac{\partial \rho}{\partial t} + \frac{\partial}{\partial x}(\rho v_x) + \frac{\partial}{\partial y}(\rho v_y) + \frac{\partial}{\partial z}(\rho v_z) = 0, \quad (1.1)$$

$$\begin{aligned} \frac{\partial(\rho E)}{\partial t} + \frac{\partial}{\partial x}(\rho E + P)v_x + \frac{\partial}{\partial y}(\rho E + P)v_y + \frac{\partial}{\partial z}(\rho E + P)v_z = \\ = \rho(g_x v_x + g_y v_y + g_z v_z) - \text{div} \vec{F}_{\text{rad}}, \end{aligned} \quad (1.2)$$

$$\begin{cases} \frac{\partial}{\partial t}(\rho v_x) + \frac{\partial}{\partial x}(\rho v_x^2 + P) + \frac{\partial}{\partial y}(\rho v_x v_y) + \frac{\partial}{\partial z}(\rho v_x v_z) = \rho g_x, \\ \frac{\partial}{\partial t}(\rho v_y) + \frac{\partial}{\partial x}(\rho v_y v_x) + \frac{\partial}{\partial y}(\rho v_y^2 + P) + \frac{\partial}{\partial z}(\rho v_y v_z) = \rho g_y, \\ \frac{\partial}{\partial t}(\rho v_z) + \frac{\partial}{\partial x}(\rho v_z v_x) + \frac{\partial}{\partial y}(\rho v_z v_y) + \frac{\partial}{\partial z}(\rho v_z^2 + P) = \rho g_z, \end{cases} \quad (1.3)$$

here  $x, y, z$  are spatial coordinates,  $t$  – time,  $\rho$  – density,  $v$  – velocity,  $E$  – internal energy,  $P$  – gas pressure,  $g$  – surface gravity,  $\vec{F}_{\text{rad}}$  – radiative flux.

The radiative transfer computations utilize monochromatic opacities from the MARCS stellar atmosphere package (Gustafsson et al. 2008) which, to speed up the calculations, are grouped into into a number of opacity bins (typically, five-six). This grouping of opacities relies on a reference 1D model atmosphere to determine where optical surface at each wavelength lies, i.e., with respect to  $\log \tau_{\text{Ross}} = 0$  (here  $\log \tau_{\text{Ross}}$  is Rosseland optical depth). It is then assumed that wavelengths of similar optical surface depths should have similar dependencies on pressure and temperature and thus the corresponding opacities are coadded

into the respective bins. With such approach, one can therefore solve radiative transfer equation using a small number of bins instead of thousands or millions of wavelength points, while still expecting to have a reasonably representative model structure. In fact, it is rather surprising that such small number of opacity bins (sometimes as low as 5–6) is sufficient to produce realistic 3D hydrodynamical model atmospheres (see, e.g. Nordlund 1982; Ludwig 1992; Ludwig et al. 1994; Vögler et al. 2004). In the CO<sup>5</sup>BOLD simulations used in this Thesis, solar elemental abundances as given by Grevesse & Sauval (1998) were assumed, except for carbon, nitrogen, and oxygen, for which the following values were used:  $A(\text{C}) = 8.41$ ,  $A(\text{N}) = 7.8$ , and  $A(\text{O}) = 8.67$  (Caffau et al. 2008), with additional enhancement of  $[\alpha/\text{Fe}] = +0.4$  dex for model atmospheres of subsolar metallicity. The model calculations were made assuming local thermodynamic equilibrium, LTE (for more details about the model setup see, for example, Ludwig & Kučinskas 2012).

The result of the CO<sup>5</sup>BOLD simulation run is a series of so-called ”snapshots”, i.e., momentary structures of the model atmosphere computed at user-defined intervals of time. These structures contain the basic physical quantities that characterize given model atmosphere: coordinates of the grid, density, internal energy, and  $x$ - $y$ - $z$  components of velocity vector at each gridpoint. Using equation-of-state and opacities from the model computations, these quantities can be used to derive other thermodynamical quantities of interest (e.g., gas temperature and pressure, number densities of individual chemical elements, and so forth). Examples of CO<sup>5</sup>BOLD simulations of different types of stars are shown in Fig. 1.1.

Typically, initial structure for model atmosphere is a guess based on another model atmosphere with similar atmospheric parameters. While the code can handle various setups for the initial model structure, a guess that is closer to the expected model structure results in shorter relaxation time. As any guess for the initial structure in general will be inaccurate, one has to check the evolution of the model atmosphere in time to ensure that the model reaches/relaxes to quasi-stationary state. There are two important parameters which may need to be adjusted during the relaxation phase. First, is the geometry of the box. The starting model atmospheres may initially appear to be out of equilibrium with the gravitational field, and the matter in the model box may fall towards the deeper layers to become denser, or expand to become less dense. As one is generally interested in modelling certain range of optical depths and has limited resources for the computations, model box may need to be adjusted after the new pressure-

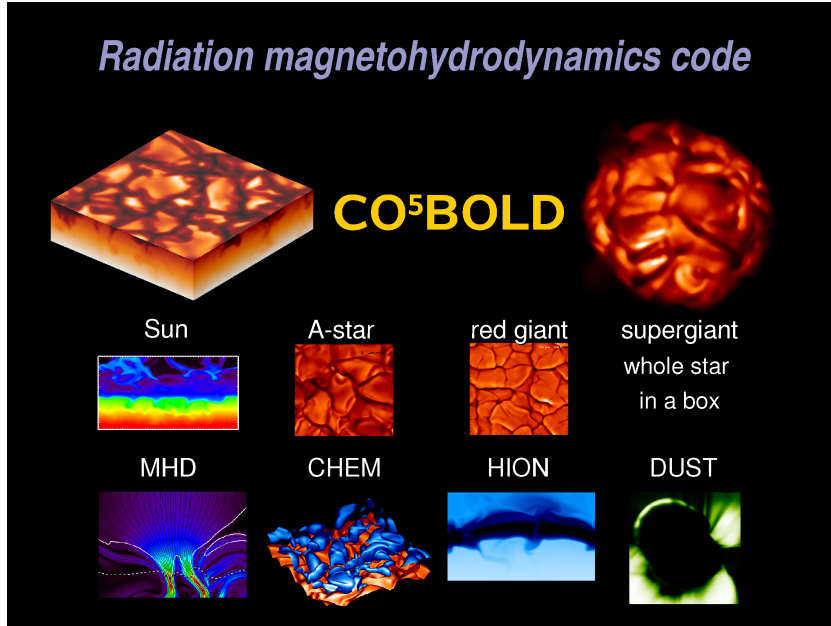


**Fig. 1.1.** Examples of 3D hydrodynamical of model atmospheres computed with the CO<sup>5</sup>BOLD model atmosphere package (from <http://folk.uio.no/svenwe/research/project.html>).

gravity equilibrium is established, so that the entire range of Rosseland optical depths of interest is covered in the simulation box. Second, the radiative flux and, therefore,  $T_{\text{eff}}$  is controlled by adjusting entropy flux at the lower boundary of the model box. This allows to control the heat flow through the model atmosphere but it takes additional time for the model to relax to its new equilibrium state after the entropy influx has been modified.

After the initial relaxation to a quasi-stationary state, the model simulations are run to cover a span of at least ten convective turnover times, as measured by the Brunt-Vaisälä timescales (for a definition see, e.g., Ludwig et al. 2002). This is to ensure that model runs cover a large enough timespan to have sufficient number of statistically independent snapshots that could be used further in, e.g., spectral line synthesis computations. To speed up spectral synthesis computations, a representative subset of momentary model structures is selected based on the criteria that are described in Appendix A.

### 1.1.2 Averaged $\langle 3D \rangle$ models

For each of the selected snapshots, we also computed a corresponding average 3D model,  $\langle 3D \rangle$ , which is obtained by spatially averaging the thermal structure of the 3D model box on surfaces of equal Rosseland optical depth. In the models used throughout this Thesis, we average the fourth moment of temper-

ature ( $\langle T(\tau_{\text{Ross}})^4 \rangle^{0.25}$ ) and the first moment of gas pressure ( $\langle P_{\text{gas}}(\tau_{\text{Ross}}) \rangle$ ) to preserve the radiative properties of the original 3D model, according to the prescription given in Steffen et al. (1995). The product of this procedure is a 1D model atmosphere that retains the averaged vertical profile of the thermodynamical structure of the 3D model but lacks explicit information about the horizontal inhomogeneities.

We also used horizontally-averaged model snapshots from the full sequence of the simulation run, which is automatically saved by the CO<sup>5</sup>BOLD. They are averaged on surfaces of equal physical height and are used to determine properties of the full simulation sequence, e. g.,  $T_{\text{eff}}$ , and to select representative 3D model structures from the time series for spectral synthesis computations.

## 1.2 1D hydrostatic LHD model atmospheres

LHD is a hydrodynamical stellar atmosphere modeling package based on plane-parallel geometry (Caffau et al. 2008). Its main advantage is that it uses the same input data (equation-of-state, opacities) as the 3D hydrodynamical CO<sup>5</sup>BOLD model atmospheres. To serve as a reference point for classic 1D hydrostatic model atmospheres, static stellar structure is enforced by adjusting model viscosity to artificially suppress hydrodynamical motions. The parameters that define LHD model atmosphere are effective temperature,  $T_{\text{eff}}$ , surface gravity,  $\log g$ , and chemical composition. Convection is modeled using the MLT formalism of Mihalas (1978). The efficiency of convection is controlled via the mixing length parameter,  $\alpha_{\text{MLT}}$ , which is defined as the ratio of mixing length,  $l$ , and the pressure scale height,  $H_{\text{P}}$ , i. e.,  $\alpha_{\text{MLT}} = l/H_{\text{P}}$ . For the LHD models used in this Thesis, we used  $\alpha_{\text{MLT}} = 1.0$ .



## Chapter 2

# Spectral line synthesis

To compute a spectrum originating from the given model atmosphere one has to solve a separate problem of radiative transfer. This is because detailed spectral features, such as individual spectral lines of chemical elements, are not computed when the model atmospheres are calculated. For the spectral line synthesis, we used `Linfor3D` package which is compatible both with 3D hydrodynamical `CO5BOLD` and 1D hydrostatic `LHD` model atmospheres. It is important to note that, in many cases, LTE is normally assumed when computing spectral lines. However, this assumption implies that distribution of atomic level populations is defined solely by the local temperature in the line-forming region.

This assumption is valid only if collisions between particles are able to effectively thermalize populations of the atomic levels. This is not necessarily true in the optically thin layers which are above what is generally considered a stellar surface. To account for the departures from LTE, we use spectral synthesis package `NLTE3D` which allows to calculate level populations of a given model atom assuming NLTE and thereby to account for the influence of non-local radiation field. These level populations are then supplied as input to `Linfor3D` to calculate NLTE spectral line profiles.

## 2.1 3D/1D NLTE/LTE spectral line synthesis with the `Linfor3D` code

`Linfor3D`<sup>1</sup> is a spectral synthesis code, primarily designed to work with the 3D model atmospheres (`CO5BOLD`), but it can be used to do 1D spectral synthesis as well. Externally computed level population departure coefficients (such as those obtained with `NLTE3D`) can be used to modify level populations that are otherwise computed in LTE using Saha-Boltzmann equation, thus enabling synthesis of line profiles in NLTE as well.

Generally, `Linfor3D` reads input physical data (equation-of-state, chemical composition) and model atmospheres, interpolates the latter to a refined grid,

---

<sup>1</sup>[http://www.aip.de/Members/msteffen/linfor3d/files/linfor\\_3d\\_manual\\_6\\_1\\_0](http://www.aip.de/Members/msteffen/linfor3d/files/linfor_3d_manual_6_1_0)

then further interpolates 3D model grid for the computation of inclined rays, and averages 3D model on the surfaces of equal optical depth. Having modified the input model atmospheres, spectral synthesis computations of user-specified spectral lines is performed along the given ray system. As it was already mentioned above, there is also an option to modify the Saha-Boltzmann level populations using NLTE departure coefficients in order to account for NLTE effects in the spectral line synthesis calculations. The influence of velocity fields in the 3D hydrodynamical model atmosphere is taken into account both in the computation of LTE and NLTE spectral line profiles. Line depression is calculated at each requested wavelength point and is integrated to obtain the emerging (surface) intensities along the ray system. Further integration over spatial angles gives radiative flux. Besides the spectral line profiles, the code allows to compute contribution functions<sup>2</sup> which allow to study the details of the spectral line formation (e.g., locate the optical depths at which particular spectral lines form).

In this work, spectral synthesis computations typically covered atmospheric layers extending from  $\log \tau_{\text{Ross}} = 2.0$  to  $\log \tau_{\text{Ross}} = -6.0$ , with a step of  $\Delta \log \tau_{\text{Ross}} = 0.08$ . Radiative transfer equation was solved in one vertical and two inclined directions, at four azimuthal angles. Besides the 3D hydrodynamical model atmospheres, in this Thesis we also used averaged ⟨3D⟩ and 1D hydrostatic LHD model atmospheres.

## 2.2 3D NLTE software package NLTE3D

### 2.2.1 3D NLTE spectral line synthesis

The NLTE3D code is used to calculate NLTE–LTE departure coefficients of atomic levels in a model atom of a given chemical element. The model atom itself is used to define the energy levels of a given atom and transition probabilities between them. Departure coefficient,  $b_i$ , is a multiplier to the level populations predicted by the Saha-Boltzmann equation, and is defined as the ratio of NLTE and LTE atomic level populations,  $b_i = n_{i,\text{NLTE}}/n_{i,\text{LTE}}$ , where  $i$  is the index of the level, and  $n_{i,\text{NLTE}}$  and  $n_{i,\text{LTE}}$  are level populations in NLTE and LTE, respectively. The novelty of this code is that it works with the 3D model structures, primarily those computed with the 3D hydrodynamical CO<sup>5</sup>BOLD model atmospheres, as well as with the LHD model atmospheres. This allows to estimate effects of

---

<sup>2</sup>Contribution function is the rate of line equivalent width growth,  $dW/d \log \tau_{\text{Ross}}$ , computed as a function of Rosseland optical depth.

convection and non-equilibrium radiative transfer on the spectral line formation both in 3D and 1D.

In general, the need for a NLTE solution comes from our knowledge that conditions for conventional LTE simplification are not strictly satisfied in the optically thin layers of stellar atmospheres. This, however, does not mean that LTE spectral synthesis techniques are not valid, since numerous spectral lines are insensitive to NLTE effects, and, whenever possible, such lines should be preferred in the abundance analysis. However, in certain cases, such spectral lines are simply not available. Then a model atom has to be devised in order to account for the transitions that may take place under the influence of non-local radiation field. Since continuum forming layers make a smooth transition into optically thin regions, one has to solve radiative transfer equation at all wavelengths where model atom can absorb or emit radiation. Bound-free transition rates are calculated once (not iterated) since a change of population distribution of a single element (apart from hydrogen) is not expected to significantly change the whole continuum radiation. For this purpose, ATLAS9 (Castelli & Kurucz 2003) opacity distribution functions, ODFs, are used in the NLTE3D code. After calculating photoionizing rates, spectral line profiles for each transition are synthesized using an initial assumption about the distribution of the level populations, usually computed using the Saha-Boltzmann equation. If one knows beforehand that some transitions are weak (i.e., indiscernible from the continuum), it is enough to compute their radiative transition rates once, as these rates are anyway very low. For stronger spectral lines, iterative calculations are needed, as such lines can significantly affect the distribution of populations of the radiatively connected levels, thus making initial assumption about the level populations inaccurate. Therefore, additional iterations are usually needed until the final distribution of level populations is obtained. Once the calculations of level departure coefficients completed, the level departure coefficients are produced as output by NLTE3D and can be used in the spectral synthesis with `Linfor3D`.

### **2.2.2 Model atom of lithium**

As a starting point for the construction of the model atom of lithium, we used a simplified model atom of Li I which was originally developed and tested by Cayrel et al. (2007) and Sbordone et al. (2010). For the purposes of the current work, the model atom was updated and now consists of 26 levels and 123 bound-bound transitions of Li I (96 of which are radiative) and the ground level of Li II,

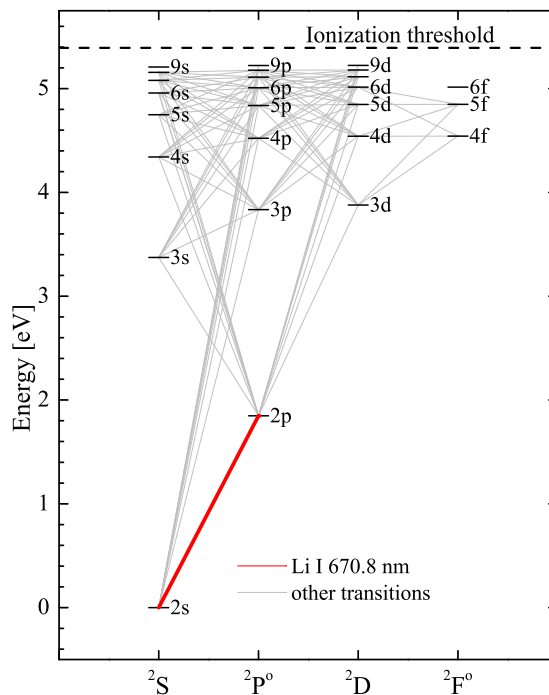


**Fig. 2.1.** Model atom of lithium used in the 3D NLTE spectral line synthesis computations (Chapter 5). The thick red line indicates the transition that corresponds to the lithium 670.8 nm resonance doublet. Other radiative bound-bound transitions are shown as grey lines.

with each level of Li I coupled to the continuum via bound-free transitions. (The ground state of Li II in the current model atom is always in LTE, since lithium is mostly fully ionized throughout the model atmospheres studied in this work.) This renders the model atom complete up to the principal quantum number  $n = 6$  and spectroscopic term  $^2F^{\circ}$ , while selected additional energy levels are included up to  $n = 9$  and term  $^2D$  (Fig. 2.1). Data concerning atomic energy levels and transitions (level energies and statistical weights; wavelengths and Einstein coefficients of the bound-bound transitions) were taken from the NIST database<sup>3</sup>. We used electron collisional excitation and ionization rates from the quantum mechanical computations of Osorio et al. (2011) for the energy levels of up to 5s ( $^2S$ ). Elsewhere, collisional excitation by electrons for radiatively permitted transitions was accounted for by using the classical formula of van Regemorter (1962), while the formula of Seaton (1962) was used to compute collisional electron ionization rates. To account for the collisional excitation by hydrogen, we used collisional excitation rates computed by Barklem et al. (2003), while the classical formula of Drawin (in the formulation of Lambert 1993) was used for

<sup>3</sup><https://www.nist.gov/pml/atomic-spectra-database>

radiatively permitted transitions when no quantum mechanical data were available. Hydrogen H–Li charge transfer rates were taken from Barklem et al. (2003) for the atomic levels up to 4p inclusive. Bound-free transitions resulting from collisions with hydrogen were expected to be inefficient and thus were ignored. Photoionization cross sections were taken from TOPBASE (Cunto et al. 1993). No scaling of collisional rates was applied in the calculations of bound-free and bound-bound transitions, i.e., the scaling factor  $S_{\text{H}}$  was set to  $S_{\text{H}} = 0$ . Information about the energy levels and bound-bound radiative transitions included in the present version of the Li I model atom are provided in Appendix 5.3, Tables B.1, and B.2, respectively. Twenty-seven transitions in the model atom are purely collisional. Collisional radiatively-forbidden transitions involving Li I levels beyond 5s were not accounted for because reliable quantum-mechanical data for these transitions are not available. We note that the role of the omitted transitions between the higher levels is minor: when they are taken into account using the formula of Allen (1973), with the collision strength set to  $\Omega = 1$ , the change in the estimated abundance (which directly applies to abundance corrections, too) is always less than 0.05 dex, with typical values being significantly smaller.



## Chapter 3

# The influence of convection on spectral line asymmetries and shifts

Before investigating the role of convection in stellar atmospheres, it was needed to ensure that the employed model atmospheres are realistic enough to be used in the analysis of spectral line formation in stellar atmospheres. An unique property of 3D hydrodynamical model atmospheres is that they predict the existence of velocity field in any model atmosphere where convection takes place. This field is taken into account when synthesizing spectral lines and is responsible for the Doppler shifts of the spectral line profiles, as well as for their turbulence broadening (in the 1D hydrostatic model the latter is taken into account using a free parameter, depth-independent microturbulence velocity). The existence of velocity fields leads to the formation of asymmetrical line profiles and Doppler shifts of the line cores. These line asymmetries and core shifts are different for different spectral lines and cannot be predicted using classical 1D hydrostatic model atmospheres.

One of the aims of this study therefore was to investigate how accurately the current 3D hydrodynamical model atmospheres may predict spectral line asymmetries and coreshifts that are measured in the spectra of real stars. In this Chapter we describe the results obtained in our study of the asymmetries and coreshifts of Fe I lines in the spectrum of the metal-poor red giant HD 122563. Atmospheric parameters of this star have been re-derived recently by using HIPPARCOS parallaxes to obtain its surface gravity,  $\log g = 1.6$  (van Leeuwen 2007), and CHARA interferometry to determine its effective temperature,  $T_{\text{eff}} = 4600$  K (Creevey et al. 2012). Spectral line coreshifts and bisectors in HD 122563 have been studied also with the aid of STAGGER models (Ramírez et al. 2010). All this makes HD 122563 an interesting target for a study with CO<sup>5</sup>BOLD models, allowing to test the realism of the 3D hydrodynamical CO<sup>5</sup>BOLD model atmospheres in the giant regime, and to compare theoretical predictions obtained with the STAGGER and CO<sup>5</sup>BOLD codes.

### 3.1 Observed spectrum of HD 122563

In this study we used a HARPS spectrum of HD 122563 extracted from the ESO Science Archive Facility<sup>1</sup> (program ID 080.D-0347(A)). The spectrum was obtained in the wavelength range of 380 – 680 nm, with the average signal-to-noise ratio of  $S/N \approx 310$  and spectral resolution of  $R = 115000$ . We used the pipeline-reduced spectrum which was processed with the HARPS Data Reduction Software<sup>2</sup> (DRS). The continuum normalization was done by fitting a second order polynomial with the Dech20T spectral analysis package<sup>3</sup>.

### 3.2 3D hydrodynamical CO<sup>5</sup>BOLD model atmospheres and spectral line synthesis

For the calculation of synthetic Fe I lines, we used two 3D hydrodynamical CO<sup>5</sup>BOLD model atmospheres that were computed using identical effective temperature and gravity (taken from Creevey et al. 2012,  $T_{\text{eff}} = 4590$  K and  $\log g = 1.6$  [cgs]), at two metallicities,  $[M/H] = -2.0$  and  $-3.0$ , thus bracketing  $[Fe/H] = -2.6$  determined for this star by (Mashonkina et al. 2011). Solar-scaled abundances from Grevesse & Sauval (1998) were used, with an additional enhancement of +0.4 dex to the abundances of O, Ne, Mg, Si, S, Ar, Ca, and Ti. In case of C, N, and O, we used abundances from Asplund et al. (2005). The 3D hydrodynamical CO<sup>5</sup>BOLD model atmospheres were calculated using a rectangular box of  $200 \times 200 \times 170$  grid points and covered  $4.2 \times 4.2 \times 2.1$  Gm in physical dimensions (in  $x, y, z$ , respectively). From the entire 3D model run, twenty 3D model snapshots (i.e., 3D model structures obtained at different instants in time) were chosen for the spectral synthesis of the Fe I lines.

Computations of synthetic Fe I line profiles were performed under the assumption of LTE, using for this purpose the Linfor3D spectral synthesis package. Spectral lines were synthesized for different iron abundances to obtain sequences of Fe I line profiles at  $[M/H] = -2.0$  and  $-3.0$ , with the iron abundances changing in steps of 0.2 dex. The obtained line profiles were then interpolated for the metallicity of HD 122563,  $[Fe/H] = -2.6$  (Mashonkina et al. 2011). To speed up the line synthesis calculations, only every third point of the 3D model

---

<sup>1</sup>[http://archive.eso.org/eso/eso\\_archive\\_main.html](http://archive.eso.org/eso/eso_archive_main.html)

<sup>2</sup><https://www.eso.org/sci/facilities/lasilla/instruments/harps/doc.html>

<sup>3</sup><http://www.gazinur.com/DECH-software.html>

structure (in each horizontal direction) was used to synthesize the Fe I lines. Tests made with the full 3D model structures showed that this simplification did not alter the resulting line bisectors by more than  $\sim 0.02$  km/s.

For the line bisector and coreshift analysis (Sect. 3.3), we used 81 non-blended Fe I lines located in the wavelength range of  $\sim 400$ – $670$  nm. Line wavelengths were taken from Nave et al. (1994), line excitation potentials and line broadening parameters were extracted from the VALD database (Kupka et al. 1999). The rotational velocity,  $v \sin i$ , was obtained by simultaneously adjusting the line strength, Doppler shift, and  $v \sin i$  of theoretical profiles and fitting them to the observed line profiles. During this procedure, the instrumental broadening and continuum level were kept fixed.

### 3.3 Line asymmetry measurements

Three quantities characterizing spectral line profiles were used to study the influence of convection on the formation of Fe I lines: equivalent width,  $W$  (used as the line strength indicator), line coreshifts (i.e., Doppler shifts of the deepest points in the spectral line profiles), and line bisectors<sup>4</sup>. Equivalent widths were measured by integrating theoretical line profiles obtained as best-fits to the given observed line profile. Both observed and theoretical coreshifts and bisectors were calculated using the following identical routines:

- coreshifts were computed by fitting Gaussian profile to the five points centered around the deepest point in the observed/synthetic spectral line profile;
- bisectors were calculated utilizing the usual procedure of finding midpoints between the red and blue line wings at a number of different line depression levels.

Errors in the observed line coreshifts were computed by adding uncertainties in quadratures, i.e., those due to uncertainties in laboratory wavelengths, HARPS wavelength calibration, and photon noise (converted into wavelength uncertainty), and by taking a square root of the sum. We assumed that the error in the laboratory wavelength calibration was 2 m/s (taken from Nave et al. 1994) and the error in the wavelength calibration was  $\approx 15$  m/s (HARPS DRS

---

<sup>4</sup>The bisector is a line connecting loci of the midpoints between the blue and red wings of a spectral line profile at different flux (line depression) levels.

estimate). The contribution from the photon noise to the coreshift error was estimated using the  $\chi^2$  fitting procedure. For this, we assigned the measurement error to each flux point in the fitted line profile (calculated from the local  $S/N$ ), fitted it with the Gaussian profile, and obtained the coreshift error corresponding to the  $\chi^2 \pm 1$  brackets. One should note that uncertainty due to the photon noise depends both on the line strength and wavelength, such that  $S/N$  ratio increases towards the red part of the spectrum. In case of the observed line bisectors, we accounted only for the errors due to photon noise which was computed using the formula of Gray (1983).

It is important to remind that theoretical line profiles obtained using each of the twenty 3D model snapshots used in the spectral line synthesis computations are in fact different from each other. Moreover, the properties of spectral lines computed using any different snapshot selection should be slightly different from those obtained using the current snapshot selection. We therefore applied a bootstrap Monte Carlo method to estimate statistical uncertainty in the bisectors and coreshifts of the synthetic spectral lines. To this end, from the initial pool of twenty spectral lines computed using twenty 3D model snapshots we randomly selected twenty line profiles (allowing each profile to be selected several times). This procedure was repeated 1000 times, resulting in 1000 different sets of twenty theoretical line profiles. We then computed average core shifts and bisectors for each of these 1000 sets of spectral line profiles, and calculated their standard deviations (in the case of bisectors we computed standard deviations at a number of different flux levels). These standard deviations were then used as uncertainties in the theoretical line bisectors and coreshifts.

### 3.4 Results and discussion

Before comparing observed and theoretical coreshifts, we determined the radial velocity ( $v_{\text{rad}}$ ) of HD 122563 by subtracting theoretical coreshifts from the observed ones. The mean residual was then added to the mean observed line shift to obtain the radial velocity,  $v_{\text{rad}} = -25.57 \pm 0.11$  km/s (the error represents the standard deviation). An identical approach was utilized by Ramírez et al. (2010) who obtained a  $v_{\text{rad}} = -25.39 \pm 0.09$  km/s using 3D hydrodynamical STAGGER atmosphere models. The agreement between the two values obtained with different 3D hydrodynamical model atmospheres is indeed very good; the difference of 0.16 km/s is remarkably small.

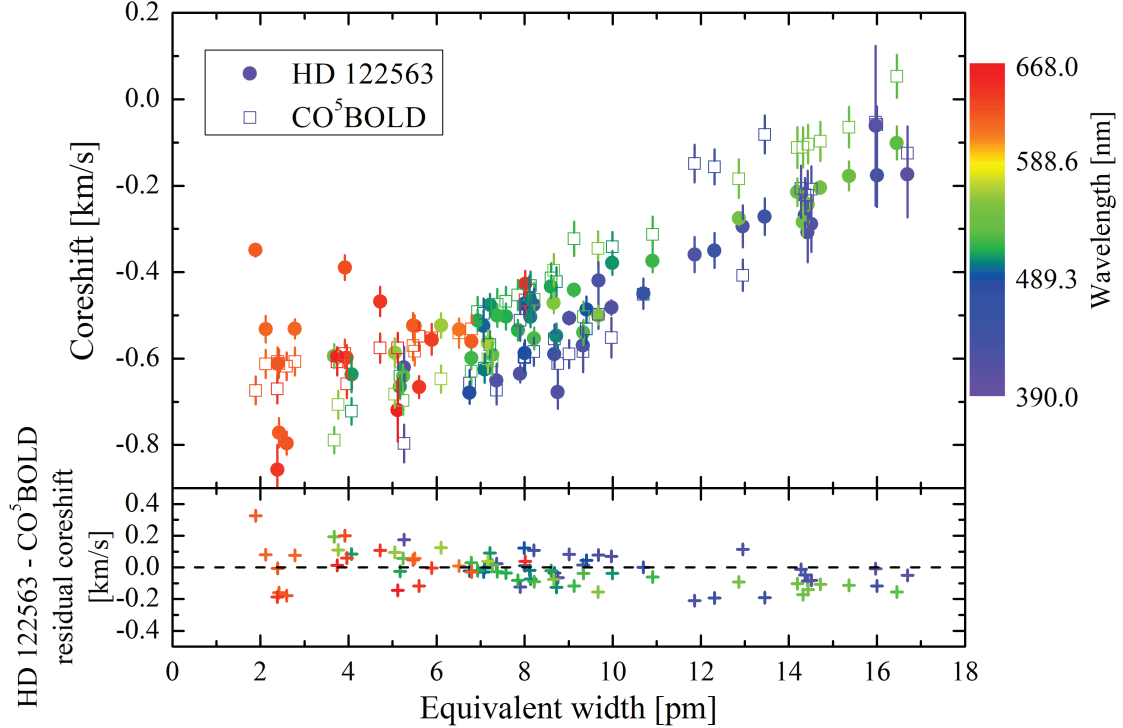


**Fig. 3.1. Top panel:** observed and theoretical coreshifts of Fe I lines in the spectrum of the metal-poor red giant HD 122563, plotted versus line equivalent width,  $W$ . Errors of the observed coreshifts take into account uncertainties in the laboratory wavelengths, instrumental wavelength calibration, and photon noise. Error bars of the theoretical coreshifts show  $1\sigma$  of the coreshift distribution obtained from the Monte Carlo bootstrap experiment (see text for details). **Bottom panel:** difference between the observed and theoretical coreshifts (i.e., residual coreshifts) plotted versus  $W$ .

The observed coreshifts (corrected for the radial velocity of HD 122563) generally agree well with those predicted using the 3D hydrodynamical CO<sup>5</sup>BOLD models (Fig. 3.1). There are hints for the coreshift dependence on wavelength seen both in the observed and theoretical coreshifts, and these trends may be partly responsible for the scatter in the  $W$ -coreshift plane seen at any given value of  $W$ . The agreement between the observed and theoretical coreshifts is reasonably good in the case of medium strong lines ( $5 \text{ pm} < W < 11 \text{ pm}$ ), with the mean residual coreshift of  $0.015 \pm 0.076 \text{ km/s}$  (error is  $1\sigma$  scatter around the mean value). The situation is slightly worse in the cases of weakest ( $W < 5 \text{ pm}$ ) and strongest ( $W > 11 \text{ pm}$ ) lines, with the mean residual coreshifts of  $+0.09 \pm 0.13 \text{ km/s}$  and  $-0.088 \pm 0.081 \text{ km/s}$ , respectively. These discrepancies are about two times larger than the respective median error of the individual residual coreshift,  $0.044 \text{ km/s}$  (weak lines) and  $0.062 \text{ km/s}$  (strong lines).

Spectral line bisectors may be yet another tool to study velocity fields in stellar atmospheres, especially since they carry the imprints from the velocity fields

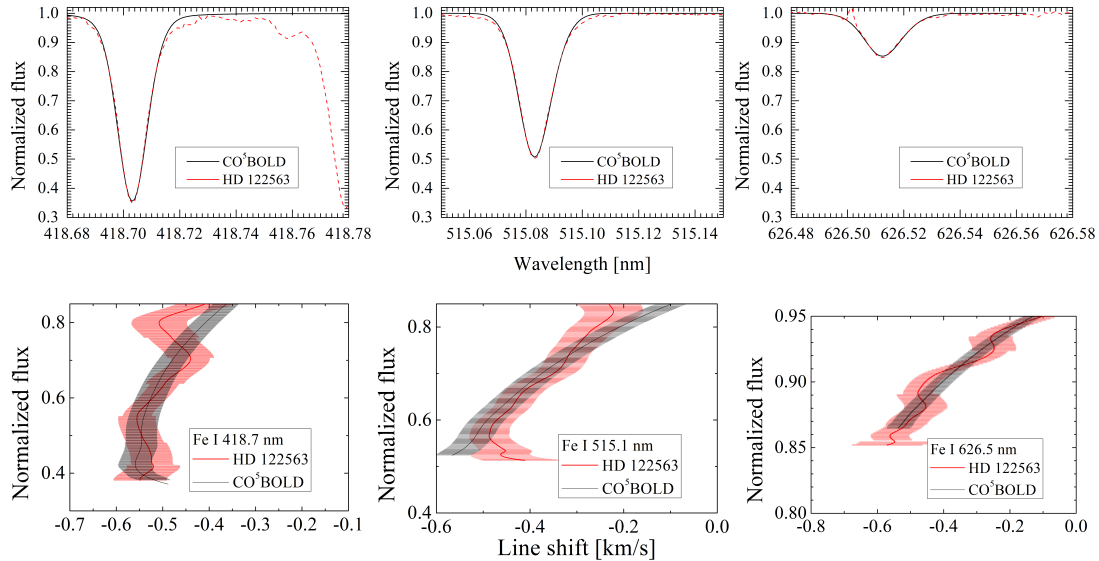


**Fig. 3.2.** Top panels: examples of the observed and best fitting theoretical Fe I line profiles in the red giant HD 122563. Bottom panels: bisectors of the spectral lines shown in the top panel. Gray shade represents the observed bisector uncertainty ( $1\sigma$ ), red shaded region shows the  $1\sigma$  uncertainty of the theoretical bisector.

and temperature inhomogeneities that are present in the formation region of a given spectral line. In our study, observed and theoretical bisectors were compared by correcting theoretical bisectors for the radial velocity of HD 122563. We stress, however, that no additional corrections were applied to the theoretical bisectors, as it is sometimes done in other bisector studies (e.g., Ramírez et al. 2010). One may note that in case of both observed and theoretical bisectors there is a clear relation between the strength of a given spectral line and its bisector shape, with the bisectors of strong lines being nearly vertical and those of weaker lines becoming more curved, with the line cores getting progressively more blueshifted with decreasing line strength (Fig. 3.2).

From the comparison of observed and theoretical bisectors provided in Fig. 3.2 we conclude that there is a reasonably good agreement between the observed and theoretical bisectors of strong lines and lines of intermediate strength (apart from the residual discrepancy in the coreshifts of strong lines). This result is similar to that obtained by Ramírez et al. (2010) using STAGGER models, where the weakest theoretical bisector was blueshifted by 0.1 km/s to match the observed bisector (the blueshifts required in case of stronger lines were smaller, at the level of  $\sim 0.03$  km/s). One should note, however, that the observed bisectors were not changing their shift monotonically. This is most likely because of very weak lines blending with the line of interest, which was not accounted for

when computing theoretical bisectors. Reasonably good agreement between theoretical predictions and observations may therefore suggest that currently available 3D hydrodynamical CO<sup>5</sup>BOLD models are reproducing the global velocity fields in the atmosphere of HD 122563 sufficiently well. Nevertheless, further improvements may be needed in order to obtain better agreement in case of the weakest and strongest spectral lines.



## Chapter 4

# The influence of convection on spectral line strength

Of a particular interest for astronomers are spectral line strengths. They can be used to infer the chemical composition of stars, which in turn can allow to deconstruct the conditions in which a star or a population of stars had formed, thus proving an invaluable tool for astroarchaeology. Having confirmed the ability of CO<sup>5</sup>BOLD model atmospheres to realistically reproduce physical properties of the spectral line forming regions in stellar atmospheres, further focus of this Thesis is on the impact of convection on the spectral line strength.

Spectral line strength is a direct indicator of the number density of a particular chemical element in the stellar atmosphere and therefore investigation of abundances of chemical elements based on different spectral lines may allow to determine chemical composition of the star. However, spectral line strength is influenced by the physical conditions in the line forming region as well. Convective atmospheres are inhomogeneous, therefore, it is not immediately clear how much the strength of a given spectral line can be affected by convection. Obviously, this may have a direct influence on the abundances of chemical elements that are determined using model atmospheres where convection is modeled using different degree of physical realism. In our study we investigated the influence of convection on the formation of spectral lines in the atmospheres of red giant stars.

### 4.1 Line strength under the influence of convection in the atmosphere of a star located at the RGB tip

To study the influence of convection on the formation of spectral lines, we used 3D hydrodynamical model atmospheres that were produced with the CO<sup>5</sup>BOLD model atmosphere package and that are now available as part of the CIFIST model atmosphere grid (Ludwig et al. 2009; the grid is constantly updated with new models). In the first study of this series, Ludwig & Kučinskas (2012), investigated physical properties of convection in the atmosphere of a red giant located

at the RGB tip ( $T_{\text{eff}} \approx 3660$  K,  $\log g = 1.0$ ,  $[M/H] = 0$ ). In this study we investigated the influence of convection on the formation of various atomic lines taking place in the atmosphere of this particular red giant star. Our main goal was to make a detailed comparison between the line strengths predicted by the 3D hydrodynamical and classical 1D models, and discuss the consequences for stellar abundance studies.

#### 4.1.1 Model atmospheres and spectral line synthesis

We used red giant model atmospheres calculated with the 3D hydrodynamical CO<sup>5</sup>BOLD and 1D hydrostatic LHD model atmosphere codes. Both models were computed using the same atmospheric parameters ( $T_{\text{eff}}=3660$  K,  $\log g=1.0$ ,  $[M/H]=0.0$ ), chemical composition, opacities, and equation of state. Additionally, we also used an average  $\langle 3D \rangle$  model. The  $\langle 3D \rangle$  model does not contain explicit information about the horizontal inhomogeneities of thermodynamical and hydrodynamical quantities (e.g. temperature, pressure, velocity) that are present in the full 3D model atmosphere. Therefore, the comparison of the predictions of the full 3D and average  $\langle 3D \rangle$  models allows to estimate the relative importance of the horizontal temperature inhomogeneities on the spectral line formation (see, e.g. Caffau et al. 2011, for a more detailed discussion).

The red giant model atmosphere used in this work was calculated with the 3D radiation hydrodynamics code CO<sup>5</sup>BOLD (Freytag et al. 2012). The model sequence was computed using a grid of  $150 \times 150 \times 151$  mesh points ( $x \times y \times z$ ), which corresponds to a physical box size of  $15.6 \times 15.6 \times 8.6 \text{ Gm}^3$ . Radiative opacities were grouped into five opacity bins. After the initial relaxation to a quasi-stationary state, the model simulations were ran to cover a span of  $\sim 6 \times 10^6$  sec ( $\sim 70$  days) in stellar time. This corresponds to approximately seven convective turnover times. From this sequence of relaxed models we selected fourteen 3D model structures computed at different instances in time (snapshots). Individual snapshots of this 14-snapshot subset were then used to produce average  $\langle 3D \rangle$  model. The same snapshot ensemble was also used for the spectral synthesis calculations. Snapshots of this 14-snapshot selection were separated by  $5 \times 10^5$  sec ( $\sim 6$  days) in stellar time, which allowed us to assume that in this subset they were statistically uncorrelated.

In this study we used fictitious spectral lines, i.e., lines of a particular chemical element for which the central wavelength,  $\lambda_c$ , the excitation potential of the lower level,  $\chi$ , and line equivalent width,  $W$ , were selected arbitrarily. This ap-

proach allowed us to cover a range in  $\lambda_c$  and  $\chi$  to quantify the trends of line formation properties in the 3D hydrodynamical and 1D classical model atmospheres with respect to  $\chi$  and  $W$ . Conceptually, this method can be traced back to the work of Steffen & Holweger (2002) and was applied in several later studies, too (e.g., Collet et al. 2007; Kučinskas et al. 2013; Dobrovolskas et al. 2013).

Synthetic line profiles were calculated for the following tracer species of astrophysical interest:

- neutral atoms: Li I, Na I, Mg I, Al I, K I;
- ionized atoms: Mg II.

More spectral lines of other chemical elements were computed during the course of this project, however, only those computed by the author of this Thesis are described and discussed in what follows below.

Fictitious lines were calculated at three wavelengths,  $\lambda_c = 400, 850,$  and  $1600$  nm. The first two were selected to bracket the wavelength range accessible with modern high-resolution optical spectrographs (e.g., UVES/GIRAFFE@VLT, HARPS@ESO3.6m, HIRES@Keck), whereas the third corresponds to the wavelength of the near-infrared *H*-band of a number of modern spectrographs (e.g., CRIRES@VLT, NIRSPEC@Keck). One should also note that 850 and 1600 nm coincide respectively with the maximum and minimum absorption of the  $H^-$  ion, which is the most important contributor to the continuum opacity in red giant atmospheres in the optical to near-infrared wavelength range. On the other hand, the continuum opacity at 400 nm is dominated by the contribution from metals. Therefore, the choice of the three wavelengths gives a possibility to study the interplay between the different sources of continuum opacity and line formation.

The excitation potentials were selected to cover the range of  $\chi$  combinations possible for real (i.e., non-fictitious) elements/lines. We used  $\chi = 0-6$  eV for the neutral atoms, and  $0-10$  eV for the ions (in both cases with a step of  $\Delta\chi = 2$  eV).

We finally stress that some of the elements/species studied here have only a few real lines that can be used in the spectroscopic diagnostics of red giant stars (e.g., Li I 670.8 nm is the main and in most cases the only tracer of lithium abundance in stars; in case of sodium, in the metal-poor stars only Na D lines are available; and so on). Moreover, we also included several elements whose spectral lines are very difficult to observe. We stress that all these elements were included to help understand the trends and properties of spectral line formation

in the presence of realistically modeled convection, and to identify the physical causes behind them.

3D spectral synthesis calculations are very time-consuming and thus performing them by using the entire 3D model sequence would be impractical. To make the task manageable, synthetic spectral line profiles were computed using 14 3D model structures (snapshots) selected from the sequence of seventy 3D models, fully relaxed to a quasi-stationary state. To speed-up calculations further, spectral synthesis was carried out on a coarser  $x, y$  grid of  $50 \times 50$  points, i.e., using only one third of the grid points of the original 3D model box in each horizontal direction. Full-resolution test calculations performed on the original  $150 \times 150$  grid show that the reduced horizontal resolution has a negligible effect on the properties of synthesized spectral lines.

For all elements investigated here, spectral line profiles corresponding to the 3D hydrodynamical model were calculated for each individual 3D model structure (snapshot) in the 14-snapshot ensemble. A composite 3D line profile was then constructed by co-adding the line profiles corresponding to all fourteen snapshots. Similarly,  $\langle 3D \rangle$  line profiles were calculated using a sequence of  $\langle 3D \rangle$  models obtained according to the prescription given in Sect. 1.1.2. Spectral line profiles were calculated for each of the fourteen  $\langle 3D \rangle$  models and then co-added to produce a composite  $\langle 3D \rangle$  line profile. A microturbulence velocity of  $\xi_{\text{mic}} = 2.0$  km/s was used in the line synthesis calculations with the  $\langle 3D \rangle$  and 1D models. The choice of  $\xi_{\text{mic}}$  was not critical since we used only weak unsaturated lines which are insensitive to the choice of microturbulence velocity (Sect. 4.1.2).

To enable a strictly differential comparison between the predictions of the 3D and 1D models, 3D,  $\langle 3D \rangle$ , and 1D spectral synthesis computations were made with the same spectral synthesis code, `Linfor3D`. Additionally, as stated above, the 3D and 1D models used in the computations shared identical atmospheric parameters, chemical composition, equation of state, and opacities. We therefore tried to minimize the differences in the model calculation procedure and line synthesis computations, so that any discrepancy in the predictions obtained with 3D and 1D models could be traced back to the differences in physical realism invoked in the two types of models.

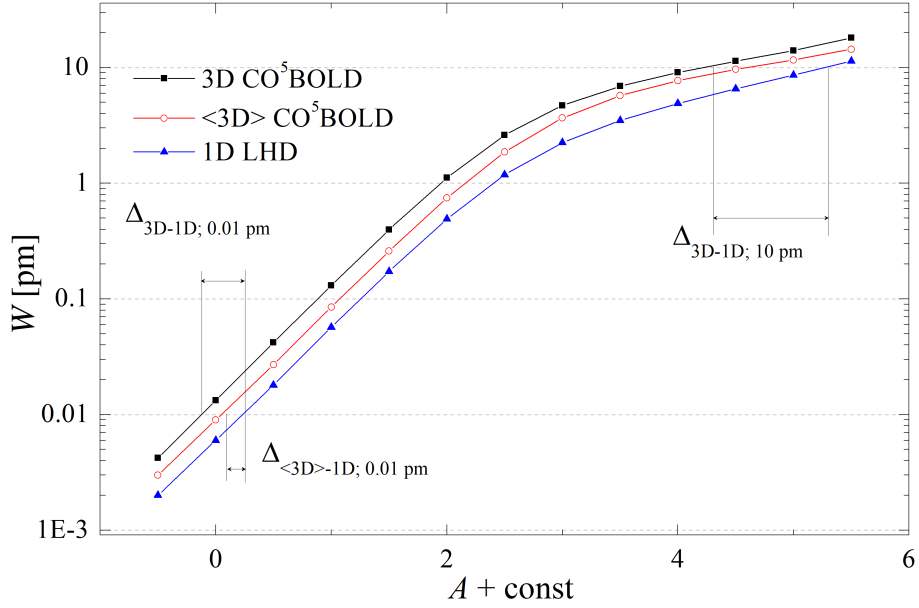


**Fig. 4.1.** Schematical explanation of the definition of abundance correction. Lines are curves-of-growth calculated using identical atomic line parameters but different model atmospheres,  $A$  is abundance,  $W$  is the equivalent width of a spectral line.

#### 4.1.2 3D–1D abundance corrections

The influence of convection on the spectral line formation and the resulting line strengths was investigated with the aid of 3D–1D abundance corrections. The 3D–1D abundance correction,  $\Delta_{3D-1D}$ , was defined as the difference in the abundance  $A(X_i)$  of the element  $X_i$  obtained at a given equivalent width of a particular spectral line with the 3D hydrodynamical and classical 1D model atmospheres,  $\Delta_{3D-1D} = A(X_i)_{3D} - A(X_i)_{1D}$  (Fig. 4.1; see, e.g., Caffau et al. 2011). The contribution to the 3D–1D abundance correction comes from two major constituents: (a) the correction due to the horizontal temperature inhomogeneities in the 3D model,  $\Delta_{3D-\langle 3D \rangle} = A(X_i)_{3D} - A(X_i)_{\langle 3D \rangle}$ , and (b) the correction due to differences between the temperature profiles of the average  $\langle 3D \rangle$  and 1D models,  $\Delta_{\langle 3D \rangle-1D} = A(X_i)_{\langle 3D \rangle} - A(X_i)_{1D}$ . The full abundance correction is a sum of the two constituents,  $\Delta_{3D-1D} = \Delta_{3D-\langle 3D \rangle} + \Delta_{\langle 3D \rangle-1D}$ .

In this part of our study, the 3D–1D abundance corrections were always calculated for weak lines (equivalent width  $< 0.5$  pm). The reason for this choice was that these weak lines are supposed to be on the linear part of the curve-of-growth, where their equivalent width is independent of the microturbulence velocity,  $\xi_{mic}$ , used with the  $\langle 3D \rangle$  and 1D models. Hence, the derived 3D–1D abundance corrections become independent of the choice of the microturbulence velocity.

The 3D component of the abundance correction has some uncertainty due to non-stationary nature of 3D hydrodynamical model atmospheres. We have measured these uncertainties as standard deviations of abundance estimates derived from individual 3D model snapshots, divided by the square root of the number of snapshots ( $\sigma/\sqrt{n}$ ). This procedure gave us an approximate upper limit of the uncertainty. In reality, because the surface of a real star would be covered with many more snapshots than used in our analysis, the abundance dispersion will be smaller. In all cases, uncertainties were  $< 0.01$  dex (0.007 dex at most for resonance lines of neutral atoms), thus we conservatively adopted  $\pm 0.01$  dex as the uncertainty of abundance corrections due to non-stationary nature of 3D hydrodynamical model atmospheres.

### **4.1.3 The influence of thermodynamical structure of atmosphere on spectral line formation**

Convection indeed plays an important role in shaping the upper atmosphere of the red giant studied here: convective up-flows and down-drafts dominate close to the optical surface (optical depth  $\tau_{\text{Ross}} \approx 1$ ), whereas the shock-wave activity is most prominent in the outer atmosphere (see Ludwig & Kučinskas 2012). This alters the thermal structure of the atmosphere, in particular, by causing spatial and temporal variations of the temperature profiles in the 3D model (Fig. 4.2). Since local temperature sets the physical conditions for spectral line formation, it is reasonable to expect that line profiles predicted by the 3D,  $\langle 3D \rangle$ , and 1D models will also be different.

Obviously, there are significant differences between the number densities of chemical species predicted by the 3D hydrodynamical and classical 1D models (Fig. 4.3). To a large extent, this behavior is defined by the atomic properties of individual species, such as ionization potentials in case of atoms. This leads to different sensitivities of the number densities to temperature inhomogeneities. For example, species that are in the minority ionization stage at a given depth in the atmosphere are very sensitive to temperature inhomogeneities, since small changes in the degree of ionization may increase their number densities significantly.

For a given set of spectral line parameters (such as wavelength, excitation potential, and oscillator strength), the line formation region is essentially defined by the temperature. Since differences between the temperature profiles of the average  $\langle 3D \rangle$  and 1D models are small in the entire range of optical depths rel-

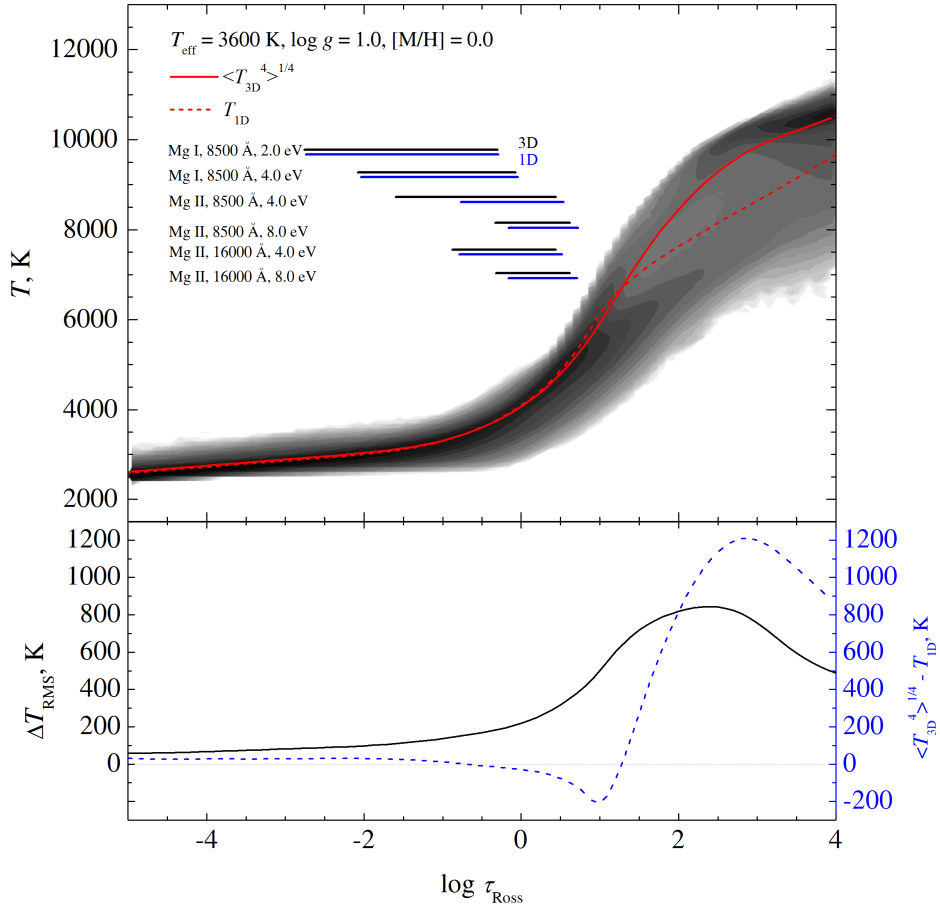


**Fig. 4.2. Top panel:** temperature profiles in the three model atmospheres of a red giant investigated in our study: 3D hydrodynamical (gray scale map showing the logarithmic probability density of the 14-snapshot ensemble), average  $\langle 3D \rangle$  (red solid line, average over the 14-snapshot ensemble), and 1D LHD model atmosphere with  $\alpha_{\text{MLT}}=1.0$  (red dashed line). Horizontal bars indicate approximate formation regions of Mg I and Mg II in the 3D and 1D models, at different wavelengths and line excitation potentials (bars mark the regions where 90% of line equivalent width is acquired, i.e., between 5% and 95% in the cumulative line depression contribution function). **Bottom panel:** RMS horizontal temperature fluctuations computed at a given Rosseland optical depth,  $\tau_{\text{Ross}}$  (black solid line, 14-snapshot ensemble); and the difference between the temperature profiles corresponding to the average  $\langle 3D \rangle$  (14-snapshot ensemble average) and the 1D model (blue dashed line).

evant to the line formation ( $|\Delta T| \lesssim 200$  K when  $\log \tau_{\text{Ross}} \lesssim 1.0$ , Fig. 4.2), this leads to very similar line formation spans in the  $\langle 3D \rangle$  and 1D models. On the other hand, the presence of horizontal temperature inhomogeneities in the line forming layers plays a major role in the 3D line formation process, leading in general to line strengthening with respect to the  $\langle 3D \rangle$  case. The amplitude of the

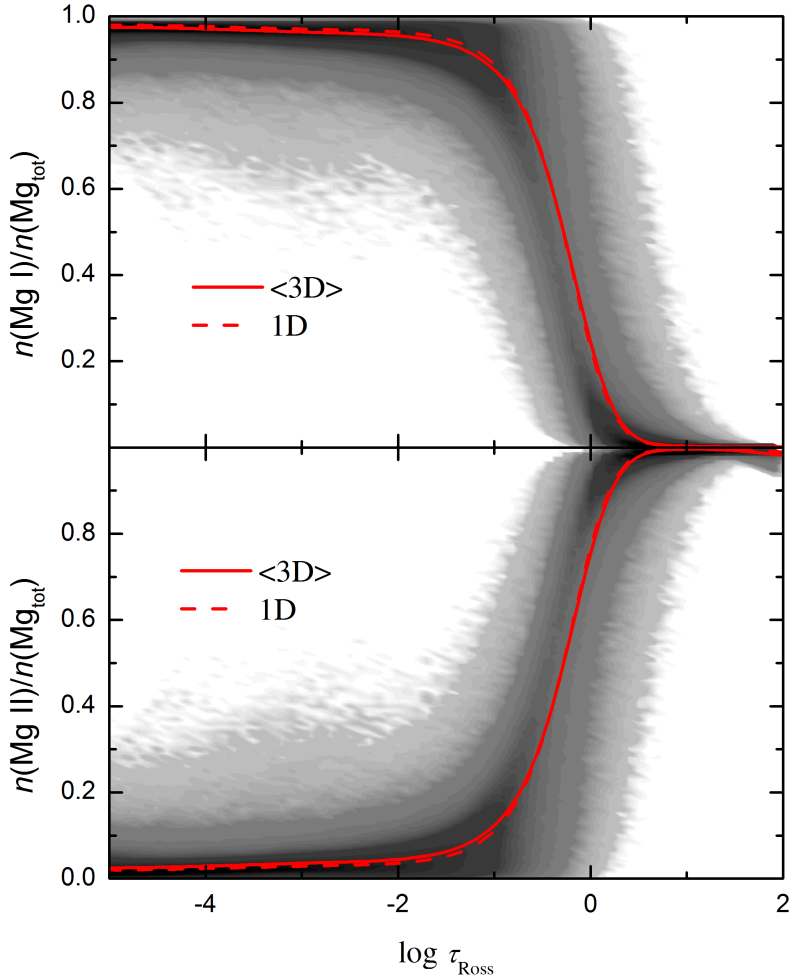


**Fig. 4.3.** Number densities of Mg I and Mg II (top-down), plotted versus  $\log \tau_{\text{Ross}}$  for the three model atmospheres of a red giant: 3D hydrodynamical (density plot), average  $\langle 3\text{D} \rangle$  (solid line, 14-snapshot ensemble average), and 1D LHD model with  $\alpha_{\text{MLT}}=1.0$  (dashed line). The number densities of Mg I and Mg II are provided as fractions of the total iron number density,  $n(\text{Mg}_{\text{tot}})$ .

deviations from the average  $\langle 3\text{D} \rangle$  temperature profile<sup>1</sup> is monotonically decreasing throughout the entire photosphere, from 500 K at  $\log \tau_{\text{Ross}} = +1.0$  to 50 K at  $\log \tau_{\text{Ross}} = -5$  (Fig. 4.2). We thus expect the differences between 3D and  $\langle 3\text{D} \rangle$  line formation to show up most clearly for high-excitation lines, forming in the deep photosphere where the horizontal temperature inhomogeneities are large. At the same time, the differences between the average  $\langle 3\text{D} \rangle$  and 1D temperature profiles will also be most pronounced in this part of the atmosphere, such that the  $\langle 3\text{D} \rangle$ –1D effects should also be strongest for the high-excitation lines.

The abundance corrections obtained for the bulk of neutral atoms are plotted

<sup>1</sup>As defined by the RMS horizontal temperature inhomogeneities.  $\Delta T_{\text{RMS}} = \sqrt{\langle (T - T_0)^2 \rangle_{x,y,t}}$ , where  $\langle \cdot \rangle_{x,y,t}$  denotes temporal and horizontal averaging on surfaces of equal optical depth, and  $T_0 = \langle T \rangle_{x,y,t}$  is the depth-dependent average temperature.

**Table 4.1.** Ionization potentials of various neutral atoms.

Element	$E_{\text{ion}}, \text{eV}$	Element	$E_{\text{ion}}, \text{eV}$
Li I	5.39	Mg I	7.65
Na I	5.14	Al I	5.99
K I	4.34		

Taken from the NIST database, [http://physics.nist.gov/PhysRefData/ASD/levels\\_form.html](http://physics.nist.gov/PhysRefData/ASD/levels_form.html)

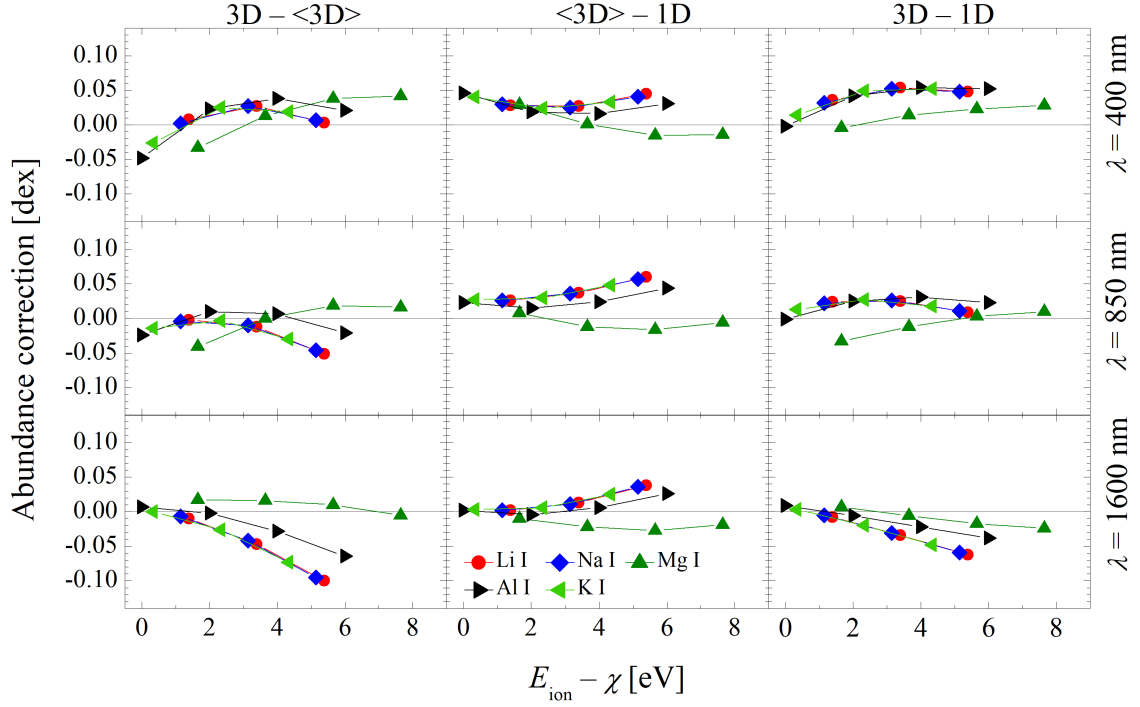


**Fig. 4.4.** Abundance corrections for spectral lines of neutral atoms, plotted versus the difference between their ionization potential and line excitation potential,  $E_{\text{ion}} - \chi$ . Three types of abundance corrections are shown:  $\Delta_{3\text{D}-\langle 3\text{D} \rangle}$  (left column),  $\Delta_{\langle 3\text{D} \rangle-1\text{D}}$  (middle column), and  $\Delta_{3\text{D}-1\text{D}}$  (right column). Abundance corrections are provided at three different wavelengths: 400 nm (top row), 850 nm (middle row), and 1600 nm (bottom row). The ionization potentials of neutral atoms used in plotting this figure are provided in Table 4.1.

in Fig. 4.4 versus the difference between their ionization and excitation potentials,  $E_{\text{ion}} - \chi$ . This choice of abscissa was motivated by the fact that for chemical elements that are almost completely ionized in the line-forming regions, it is the *difference*  $E_{\text{ion}} - \chi$  (and of course the thermodynamical conditions) that defines the number density of the neutral atoms per unit mass. The line opacity of this minority species is thus proportional to the combined Saha-Boltzmann factor,  $\kappa_{\ell} \sim \exp\{+(E_{\text{ion}} - \chi)/kT\}$  (cf. Gray 2005, in the analysis of the tempera-

ture dependence of the line strength). The abundance correction curves shown in Fig. 4.4 must therefore fall on top of each other for all neutral atoms of elements that are strongly ionized (i.e. those with sufficiently low ionization potential,  $E_{\text{ion}} \lesssim 6$  eV). Indeed, this is clearly the case for the abundance corrections of Li I, Na I, and K I, which are in their minority ionization stage throughout the entire atmosphere of this particular red giant. For this type of atoms, the total abundance correction,  $\Delta_{3\text{D}-1\text{D}}$ , and its constituents,  $\Delta_{3\text{D}-\langle 3\text{D} \rangle}$  and  $\Delta_{\langle 3\text{D} \rangle-1\text{D}}$ , are confined to the range of  $-0.1 \cdots + 0.05$  dex, with comparable contributions (of different sign) from the  $\Delta_{3\text{D}-\langle 3\text{D} \rangle}$  and  $\Delta_{\langle 3\text{D} \rangle-1\text{D}}$  corrections. All corrections are more negative in the near-IR at  $\lambda$  1600 nm than in the red at  $\lambda$  850 nm.

For elements with higher ionization potentials, neutral atoms gradually turn into majority species, and the abundance correction curves in Fig. 4.4 begin to separate. The two type of lines behave radically different, and this can be clearly distinguished in the  $\Delta_{3\text{D}-1\text{D}}$  versus  $E_{\text{ion}} - \chi$  plot. This behavior is simply a consequence of the combined action of ionization and excitation. The point is that the ionization factor dominates over the excitation factor as long as the neutral atoms are a *minority species*, and thus the line opacity decreases with increasing temperature; low-excitation lines are then most temperature-sensitive. The reverse is true for a neutral *majority species*. Here the excitation factor dominates over the ionization factor, and the line opacity increases with increasing temperature,  $\kappa_\ell \sim \exp\{-\chi/kT\}$  (cf. Gray 2005, Chapter 13, Case 1). In this situation, high-excitation lines are most temperature-sensitive.

The largest (most negative) 3D corrections are obtained for Li I, reaching down to  $\Delta_{3\text{D}-\langle 3\text{D} \rangle} \approx -0.10$ . The high-excitation fictitious lines of this element have the most temperature-sensitive Boltzmann factor and at the same time form in the deep photosphere where the temperature inhomogeneities are more pronounced than in the higher photospheric layers where the lines of the minority species originate. Surprisingly, the corrections for all atoms of majority type are much smaller at  $\lambda$  1600 nm than at  $\lambda$  850 nm. Why it is so we explain in the following subsection as this effect is more pronounced for lines of ionized atoms.

Figure 4.5 displays the abundance corrections for a selection of ionized atoms, showing a rather uniform dependence on excitation potential  $\chi$ . Let us consider the ions that represent the majority ionization stage. Their line opacity (per unit mass) depends on temperature as  $\kappa_\ell \sim \exp\{-\chi/kT\}$ . Owing to its rather low first ionization potential, Mg II is present in its majority ionization

stage throughout the entire atmosphere of this red giant (Mg II is only considered for understanding the behavior of elements that are nearly 100% ionized; Mg II lines are inaccessible to observations in real red giant atmospheres). The corrections vanish for ground-state lines and increase steadily in amplitude toward the high-excitation lines. At  $\chi = 10$  eV,  $\Delta_{3D-\langle 3D \rangle}$  amounts to  $\approx -0.6$  dex, while  $\Delta_{\langle 3D \rangle-1D}$  reaches  $\approx +0.2$  dex, hence  $\Delta_{3D-1D} \approx -0.4$  dex.

Abundance corrections in Fig. 4.5 scale with the excitation potential. This reflects sensitivity of the line opacity to the local temperature which may be expressed as  $\partial \log \kappa_\ell / \partial \log T = \chi / (kT)$ , and which applies in case of majority species<sup>2</sup>. As a result, abundance corrections, which are smallest at  $\chi = 0$ , become larger as  $\chi$  increases. The average  $\langle 3D \rangle$  model is not as hot as the 1D model in the line forming regions, which results in positive  $\Delta_{\langle 3D \rangle-1D} \sim -\chi (\log T_{\langle 3D \rangle} - \log T_{1D})$  correction. On the other hand, the  $\Delta_{3D-\langle 3D \rangle}$  component is negative, because non-linear dependence of line opacity on temperature results in mean opacity of 3D hydrodynamical model atmosphere to be higher than the line opacity obtained from the horizontally averaged temperature profile of the average 3D –  $\langle 3D \rangle$  model atmosphere.

Usually, the abundance corrections should not depend on wavelength. Temperature sensitivity of the line opacity is only weakly dependent on wavelength due to stimulated emission but the latter is minor in the regime of red giant atmospheres. However, the abundance corrections are significantly larger at  $\lambda$  850 nm than in the near-IR at  $\lambda$  1600 nm. This is despite the fact that near-IR lines form generally deeper (Fig. 4.2, lower panel), where horizontal temperature inhomogeneities are larger. The explanation for these apparently contradictory facts is that continuum opacity also affects the spectral line strengths. In fact, continuum opacity is insensitive to temperature variations at  $\lambda$  850 nm. However, at near-IR wavelengths  $H^-$  bound-free absorption becomes important. It has similar temperature sensitivity to that of the line opacity, essentially making the *ratio*  $\kappa_\ell / \kappa_c$  of line and continuum opacities less temperature-sensitive. This effectively makes the abundance corrections at the near-IR wavelengths smaller than those at  $\lambda$  850 nm.

We recall that in this work the 3D–1D corrections were calculated for very weak spectral lines. While such corrections provide a convenient way to estimate the importance of 3D hydrodynamical effects in the spectral line formation,

---

<sup>2</sup>Chemical species that are in the majority ionization stage at a given depth in the atmosphere.

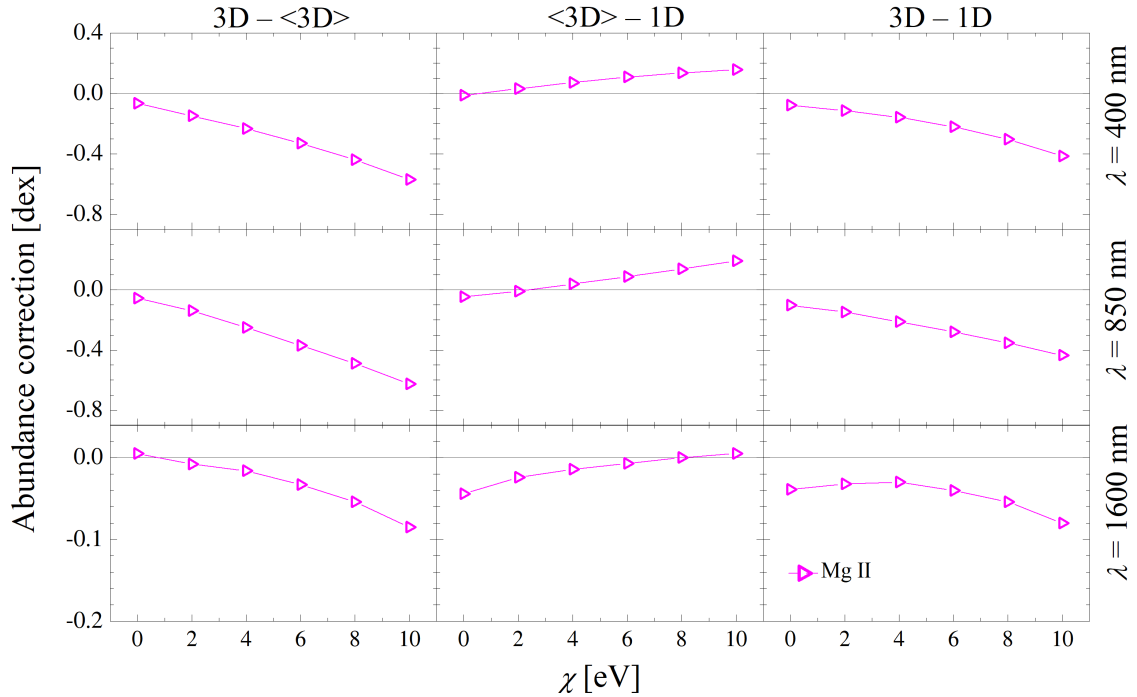


**Fig. 4.5.** Abundance corrections for spectral lines of ionized atom Mg II, plotted versus the line excitation potential,  $\chi$  (other notations as in Fig. 4.4).

abundance corrections for stronger lines may be different because of saturation effects, leading to differences in formation depths and introducing a sensitivity to velocity fields (see Appendix B.3 of Kučinskas et al. 2013).

Theoretical 3D abundance corrections were derived from the comparison of the equivalent width of the same (artificial) spectral line computed with a 3D model and a 1D model atmospheres. Since the 3D and the 1D models use identical stellar parameters, atomic data, and numerical methods (as far as possible), the resulting *differential* 3D corrections should be applicable to any 1D model, irrespective of the physical details.

For given stellar parameters ( $T_{\text{eff}}$ ,  $\log g$ ,  $[M/H]$ ) and a given element and ionization stage, the 3D abundance correction depends only on the energy of the lower level of the transition, the wavelength of the line, and, in principle, also on the mixing-length parameter used for the 1D model,  $\Delta_{3D-1D}(\chi, \lambda, \alpha_{\text{MLT}})$ , provided that the line is *weak* (on the linear part of the curve-of-growth). In this case, the corrections given in Figs. 4.4 and 4.5 can be readily applied to the 1D LTE abundance determinations performed with any standard 1D mixing-length model atmosphere:  $A(X_i)_{3D} = A(X_i)_{1D} + \Delta_{3D-1D}$ .

In the general case of stronger lines, the 3D corrections depend in addition on the the equivalent width of the line,  $W$ , and on the microturbulence parameter

**Table 4.2.** Parameters of the 3D hydrodynamical CO<sup>5</sup>BOLD red giant models representing stars located at the lower part of RGB.

$\langle T_{\text{eff}} \rangle$ , K	$\log g$ , CGS	[M/H]	Grid dimension, Mm	Resolution, grid points
4970	2.5	0	573×573×243	160×160×200
4990	2.5	-1	573×573×245	160×160×200
5020	2.5	-2	584×584×245	160×160×200
5020	2.5	-3	573×573×245	160×160×200

used for the 1D model,  $\xi_{\text{mic}}$ ,  $\Delta_{3\text{D}-1\text{D}}(\chi, \lambda, W, \xi_{\text{mic}}; \alpha_{\text{MLT}})$ . We do not provide the dependence of  $\Delta_{3\text{D}-1\text{D}}$  on  $W$  and  $\xi_{\text{mic}}$  in this work. The given corrections for the weak line limit can then only serve as an indication of the line’s susceptibility to 3D effects.

## 4.2 Line strength under the influence of convection in the atmospheres of stars located in the lower part of RGB

As a continuation of work done while studying spectral line formation in the atmosphere of a red giant located at the RGB tip, in this Section we present results obtained using red giant model atmospheres near the bottom of RGB. Besides studying of how the influence of convection on the spectral line formation changes with  $T_{\text{eff}}$  and  $\log g$  we also investigate how does the spectral lines form at different metallicities, from solar from solar to extremely metal-poor.

### 4.2.1 Model atmospheres and spectral line synthesis

In this part of our analysis we used 3D hydrodynamical CO<sup>5</sup>BOLD and 1D hydrostatic LHD model atmospheres of red giants located in the lower part of the RGB. These model atmospheres had identical atmospheric parameters, chemical composition, opacities, and equation of state. We used 3D hydrodynamical model atmospheres from the CIFIST model atmosphere grid (Ludwig et al. 2009). Model atmospheres were computed using a Cartesian grid of 160×160×200 grid points in  $x, y, z$  direction, respectively.

Parameters of the 3D model atmospheres are listed in Table 4.2. One may immediately notice that effective temperatures of these model atmospheres (i.e., averages corresponding to the selected snapshot ensembles,  $\langle T_{\text{eff}} \rangle$ ) are not identical. This is because the radiative flux (and thus,  $\langle T_{\text{eff}} \rangle$ ) is not an input parameter

in CO<sup>5</sup>BOLD model calculations. The total radiative flux, which in the end defines the average effective temperature of the model,  $\langle T_{\text{eff}} \rangle$ , is controlled by adjusting the entropy flux at the lower boundary of the model box. Therefore, there is always a small mismatch between the average effective temperatures of different models computed for the same target  $T_{\text{eff}}$  although we ensured that the difference between the actual and target  $T_{\text{eff}}$  would never exceed 30 K.

For the spectral line synthesis we selected a smaller subset of 3D atmospheric structures computed at different instants of time (snapshots). At all metallicities, these subsets consisted of 20 snapshots, spaced with a step of  $\sim 8$  hours over the interval of  $\sim 4.7 - 6.5$  days in stellar time. Since the convective time scales in the red giant models studied here were equal to  $\sim 5 - 15$  hours, such spacing of the 3D snapshots allowed to consider them statistically independent. In this study we also used averaged  $\langle 3D \rangle$  models (computed as described in Chapter 1).

In order to investigate the influence of convection on the spectral line formation we utilized fictitious spectral lines. For these lines, their central wavelengths, excitation potentials,  $\chi$ , and oscillator strengths,  $\log(gf)$  (here  $g$  is the statistical weight of the level,  $f$  is the oscillator strength), were freely chosen to spread over the range of values covered by real spectral lines. As it was already mentioned in Sect. 4.1.2 above, such approach allowed us to study connections between the atomic line parameters and line formation properties in the presence of realistically modeled convection and has been already applied in a number of earlier studies (e.g., Steffen & Holweger 2003; Collet et al. 2007).

In this study, equivalent widths of synthetic spectral lines were fixed to  $W \leq 0.5$  pm. Because such lines are very weak, their strengths should be independent of the choice of microturbulence velocity,  $\xi_{\text{mic}}$ , used in the spectral line synthesis with the  $\langle 3D \rangle$  and 1D model atmospheres. In such situation, differences in the line strengths predicted by the 3D and 1D model atmospheres can be attributed to purely 3D hydrodynamical effects, allowing to investigate their role in the spectral line formation.

In this Thesis, the Linfor3D code, which is used to solve the radiative transfer equation under the assumption of LTE, was employed for spectral synthesis of all spectral lines. As in the previous parts of this Thesis, in order to speed up spectral line synthesis calculations, we used only every third point of the original 3D model structure along the  $x$  and  $y$  spatial directions. We verified that such simplification has left the resulting elemental abundances essentially unchanged (i.e., with respect to the calculations performed using the full model box). Line

profiles were computed with a typical wavelength resolution of 130 – 150 points per profile. In case of the 3D hydrodynamical model atmospheres, spectral line profiles of every chemical element studied here were calculated for each of the twenty 3D model snapshots, at each of the four metallicities. The obtained individual spectral line profiles were then co-added to obtain the final 3D line profile at each metallicity. Similarly, in case of the average 3D models line profiles were calculated for every horizontally averaged 3D model structure from the 20-snapshot selection; the final  $\langle 3D \rangle$  line profile was then obtained by co-adding all twenty individual line profiles. All 1D line profiles were also calculated using the `Linfor3D` code (see Sect. 2.1). A microturbulence velocity of  $\xi_{\text{mic}} = 1.0$  km/s was used in all  $\langle 3D \rangle$  and 1D spectral synthesis calculations, although we note again that the choice of  $\xi_{\text{mic}}$  does not change the line strength of very weak lines studied here.

One may envision that, alternatively, all 3D model snapshots could be averaged to produce a single  $\langle 3D \rangle$  model for the synthesis of  $\langle 3D \rangle$  spectral lines, i.e., instead of using individual averaged 3D models for each 3D snapshot as we did in this study. Test computations done in Dobrovolskas et al. (2013) showed, however, that in case of Fe I and Fe II lines with  $\chi = 0 - 6$  eV differences in the line profiles computed using the two different approaches would lead to differences in the elemental abundances of less than 0.03 dex. Therefore, for the purposes of present study the choice in the procedure used to compute the  $\langle 3D \rangle$  line profiles was of minor importance.

The role of 3D hydrodynamical effects in spectral line formation was studied by utilizing 3D–1D abundance corrections (as defined in Sect. 4.1.2, p. 46). The 3D–1D abundance correction is sensitive to the effects related to both the horizontal temperature inhomogeneities and differences in temperature stratifications of the 3D and 1D model atmospheres. The size of these effects can be measured separately, by utilizing information content of the averaged  $\langle 3D \rangle$  models. Since the  $\langle 3D \rangle$  model does not contain information about the horizontal inhomogeneities of thermodynamic quantities and velocity fields, the  $\Delta_{3D-\langle 3D \rangle} \equiv A(X_i)_{3D} - A(X_i)_{\langle 3D \rangle}$  correction can be used to measure the effect of horizontal temperature inhomogeneities. Similarly, the  $\Delta_{\langle 3D \rangle-1D} \equiv A(X_i)_{\langle 3D \rangle} - A(X_i)_{1D}$  correction provides information about the role of differences between the temperature profiles of the average  $\langle 3D \rangle$  and 1D models. Obviously, the final abundance correction is a sum of the two constituents,  $\Delta_{3D-1D} \equiv \Delta_{3D-\langle 3D \rangle} + \Delta_{\langle 3D \rangle-1D}$ .

3D–1D abundance corrections were calculated for a number of neutral and

singly ionized elements: Li I, Na I, Mg I, Mg II, Al I, K I, Ca I, Ca II. These elements allow to sample different nucleosynthetic channels, for example, proton capture (Na, Al, K) and synthesis of  $\alpha$  elements (Mg, Ca). Lithium is a special element in this context, in a sense that it was produced during the Big-Bang nucleosynthesis and by several other processes afterwards.

The 3D–1D abundance corrections for neutral and ionized atoms were calculated at three wavelengths,  $\lambda = 400, 850$  and  $1600$  nm. The last of the three wavelengths sampled is very similar to that of minimum of  $H^-$  bound-free absorption while  $\lambda = 850$  nm is located close to  $H^-$  absorption peak. This allows to sample different depths in stellar atmospheres, due to the difference of how opaque the atmosphere is because of  $H^-$  ion absorption. The line excitation potentials,  $\chi = 0, 2, 4,$  and  $6$  eV, were chosen to cover the range of  $\chi$  up to ionization potentials of the investigated chemical elements.

Finally, we note that some species studied here have either only few observable spectral lines or their lines may be simply too weak to be detected (as it is the case with, e.g., Li I). We stress (again) that such elements were included in the present analysis because we aimed to understand the general properties of spectral line formation in the presence of convection, especially the trends of abundance corrections in a wider range of atomic line parameters. Obviously, in all such cases the exact values of abundance corrections in a wide atomic parameter range may only be of academic interest.

#### **4.2.2 The influence of thermodynamical structure of atmosphere on spectral line formation**

The 3D–1D abundance corrections for neutral atoms are plotted in Fig. 4.6 for  $\lambda = 400$  nm, Fig. 4.7 for  $\lambda = 850$  nm, and Fig. 4.8 for  $\lambda = 1600$  nm. The three abundance corrections,  $\Delta_{3D-(3D)}$ ,  $\Delta_{(3D)-1D}$ , and  $\Delta_{3D-1D}$  are plotted against metallicity at four line excitation potentials,  $\chi = 0, 2, 4,$  and  $6$  eV.

One may notice immediately that the obtained abundance corrections depend strongly on the metallicity of the model atmosphere. At  $[M/H] = 0.0$ , the corrections are generally small and gradually grow with decreasing metallicity, up to  $-0.8$  dex at  $[M/H] = -3.0$  (Figs. 4.6 – 4.8). They are largest for the resonance lines and decrease with increasing excitation potential, diminishing to  $< \pm 0.1$  dex irrespective of the metallicity of the model atmosphere. These tendencies are affected by two factors: ionization potential of the given atom and properties in the line formation region. Spectral lines with higher excita-

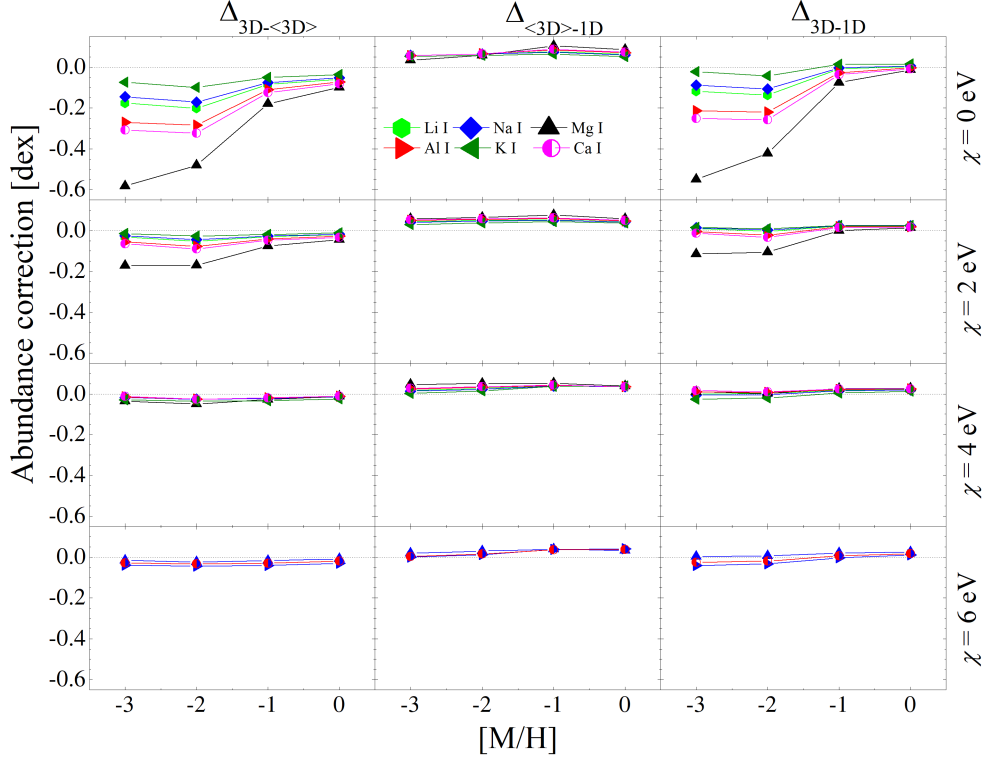


**Fig. 4.6.** Abundance corrections for the spectral lines of neutral atoms at  $\lambda = 400$  nm, plotted versus metallicity:  $\Delta_{3D-\langle 3D \rangle}$  (left column),  $\Delta_{\langle 3D \rangle-1D}$  (middle column), and  $\Delta_{3D-1D}$  (right column). Corrections are given at several different excitation potentials, as indicated on the right side of each row of the figure panels.

tion potentials form deeper in the atmosphere, while the resonance lines form in the outermost layers (Figs. 4.9 – 4.10). In general,  $\langle 3D \rangle$  and 1D model atmospheres have very similar temperature-optical depth relations throughout the line forming regions. Horizontal temperature inhomogeneities (as measured by  $\Delta T_{\text{RMS}} = \sqrt{\langle (T - T_0)^2 \rangle_{x,y,t}}$ , which is computed by averaging temperature temporally and horizontally on surfaces of equal optical depth, here  $T_0 = \langle T \rangle_{x,y,t}$  is the average temperature at a given optical depth), are small and change little with the optical depth (in comparison with inhomogeneities in the more metal-poor models investigated, see Fig. 4.9). This results in all abundance corrections,  $\Delta_{3D-\langle 3D \rangle}$ ,  $\Delta_{\langle 3D \rangle-1D}$ , and  $\Delta_{3D-1D}$ , being small and insensitive to  $\chi$ . However, this does not apply to more metal-poor model atmospheres with differences in the temperature profiles of the  $\langle 3D \rangle$  and 1D models being larger in the outer layers (Fig. 4.10). Same applies to the horizontal inhomogeneities as well. As a consequence, abundance corrections at these metallicities become larger for elements whose formation extends into the outer atmospheric layers where both horizontal inhomogeneities and differences between the  $\langle 3D \rangle$  and 1D temperature profiles

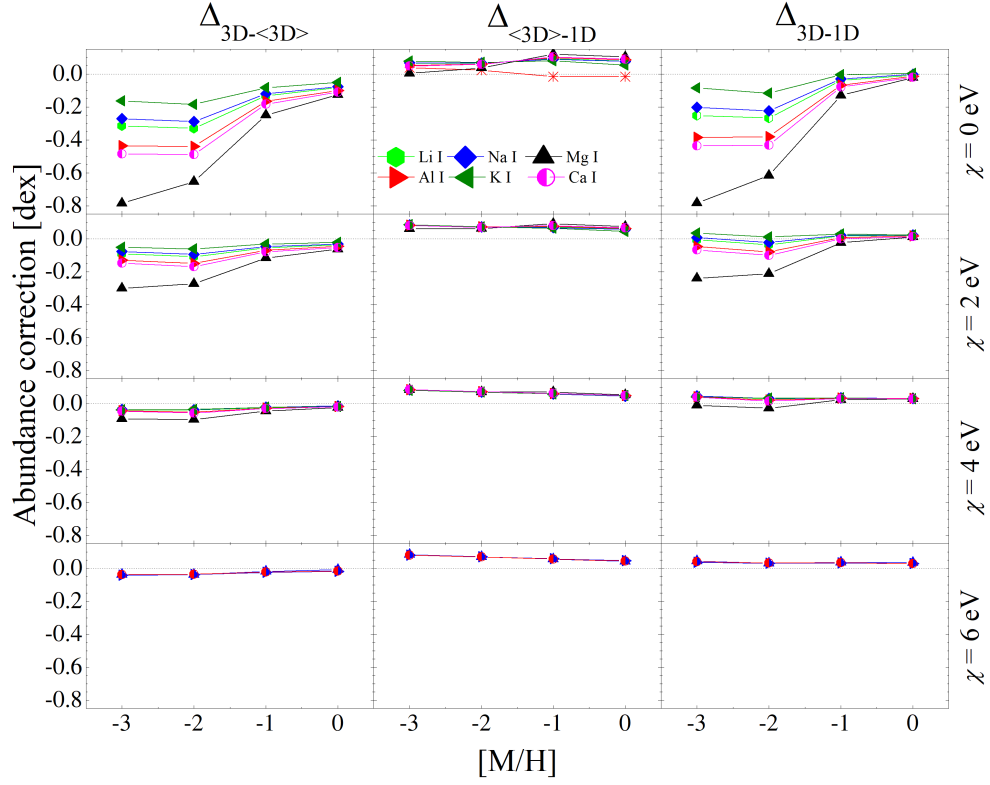


**Fig. 4.7.** The same as in Fig. 4.6 but at  $\lambda = 850$  nm.

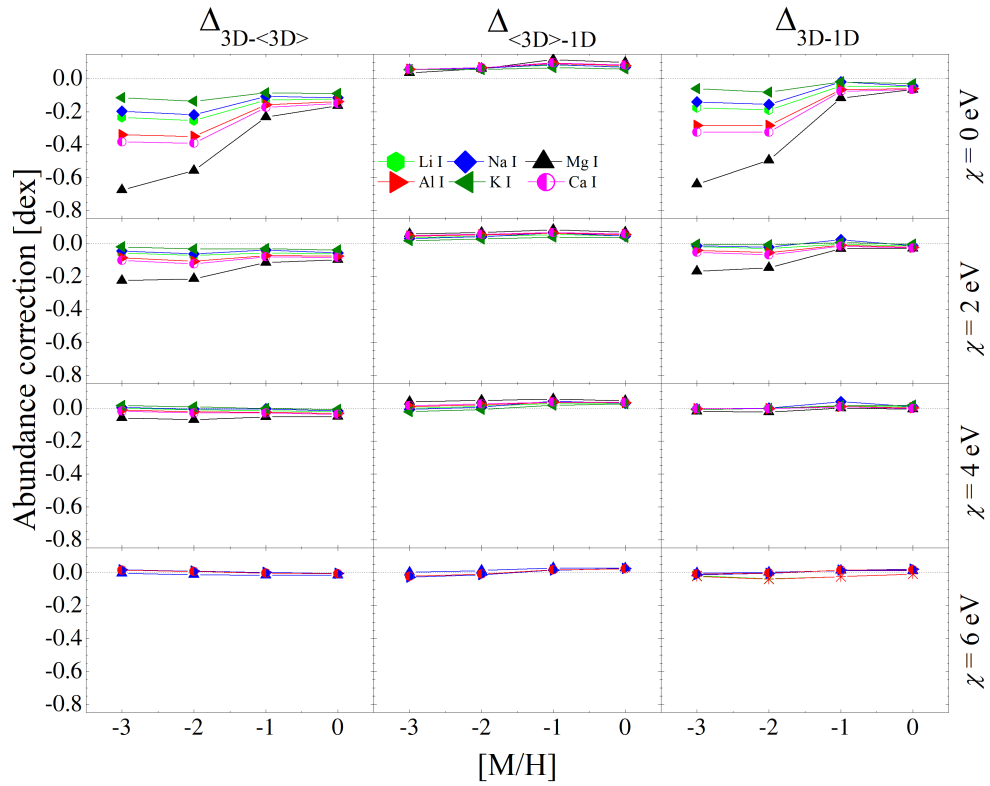


**Fig. 4.8.** The same as in Fig. 4.6 but at  $\lambda = 1600$  nm.

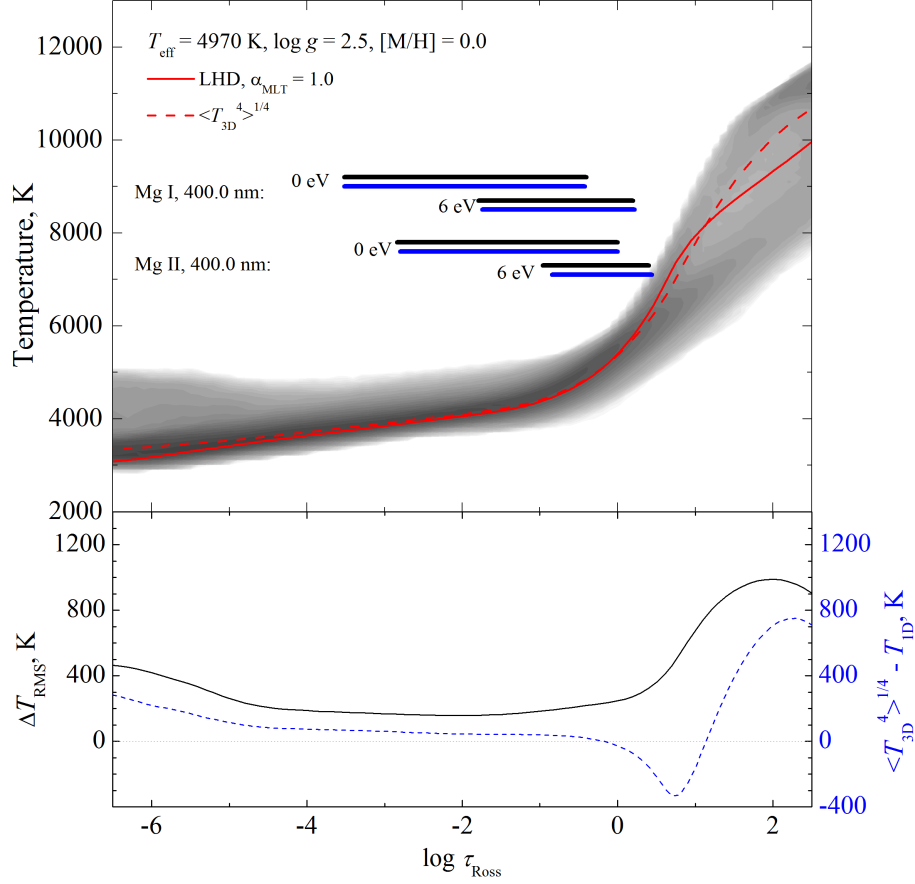


**Fig. 4.9.** **Top panel:** temperature profiles in the red giant model with  $T_{\text{eff}}/\log g/[M/H] = 4970/2.5/0.0$ , plotted versus the Rosseland optical depth,  $\tau_{\text{Ross}}$ , and shown for the following model atmospheres: 3D hydrodynamical (density plot), average  $\langle 3D \rangle$  (dashed line), and 1D (solid line). Horizontal bars mark the approximate location of the Mg I and Mg II line formation regions in the 3D (black) and 1D (blue) atmosphere models, at  $\lambda = 400$  nm and  $\chi = 0$  and 6 eV (bars mark the regions where the equivalent width,  $W$ , of a given spectral line grows from 5% to 95% of its final value). **Bottom panel:** RMS horizontal temperature inhomogeneities in the 3D model (solid line), and difference between the temperature profiles of the  $\langle 3D \rangle$  and 1D models (dashed line), shown as functions of the Rosseland optical depth. In both panels, all quantities related to the 3D and  $\langle 3D \rangle$  models were obtained using the subset of twenty 3D model snapshots utilized in the 3D spectral line synthesis calculations (see Sect. 4.2.1).

are largest. The impact of horizontal inhomogeneities on the spectral line formation in these atmospheric layers is larger than that due to differences in the temperature profiles. Therefore, as  $\Delta_{3D-\langle 3D \rangle}$  correction is significantly larger than  $\Delta_{\langle 3D \rangle-1D}$ , especially for the most metal-poor model atmospheres. In most cases, these corrections are of opposite sign and partly compensate when combined into the total correction,  $\Delta_{3D-1D}$ .

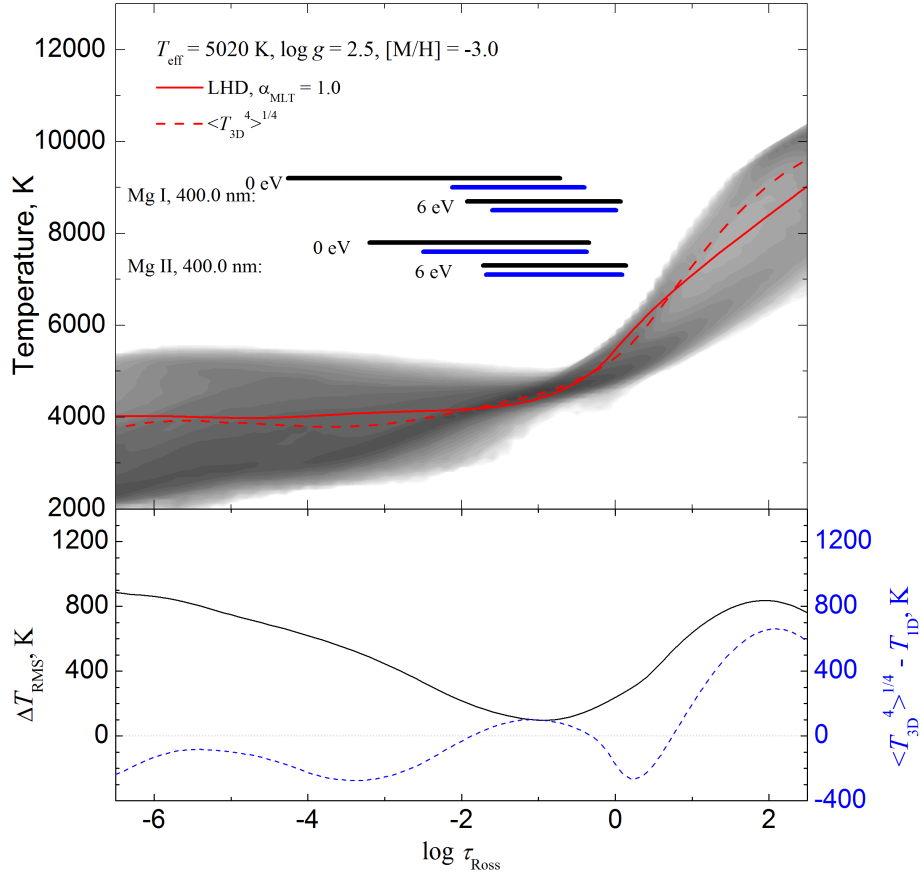


**Fig. 4.10.** Same as in Fig. 4.9 but for the red giant model with  $T_{\text{eff}}/\log g/[M/H] = 5020/2.5/-3.0$ .

Importantly, the abundance corrections obtained for different chemical elements differ significantly (Figs. 4.6 – 4.8). For example, at the metallicity of  $[M/H] = -3.0$ , the range in abundance corrections obtained for different elements spans an interval of  $-0.8$  dex to  $+0.1$  dex. This is because both excitation and ionization potentials play an important role in defining the process of spectral line formation. For example, elements with the lowest ionization potentials (Li I, Na I, K I) are almost fully ionized throughout the entire atmosphere, irrespective of the metallicity, and are the minority species (i.e., in a sense that their number densities in the neutral stage are significantly smaller than those in the first ionization stage). As it was already shown in Sect. 4.1.3, for such conditions, the line opacity,  $\kappa_\ell$ , can be approximated as  $\kappa_\ell \sim 10^{\theta(E_{\text{ion}}-\chi)}$ , where  $\theta = 5040/T$  and  $E_{\text{ion}}$  is the ionization potential of a given element. Therefore, at low excitation potentials line opacity becomes very sensitive to changes in temperature. As a result, low  $\chi$  lines are significantly affected by temperature inhomogeneities in

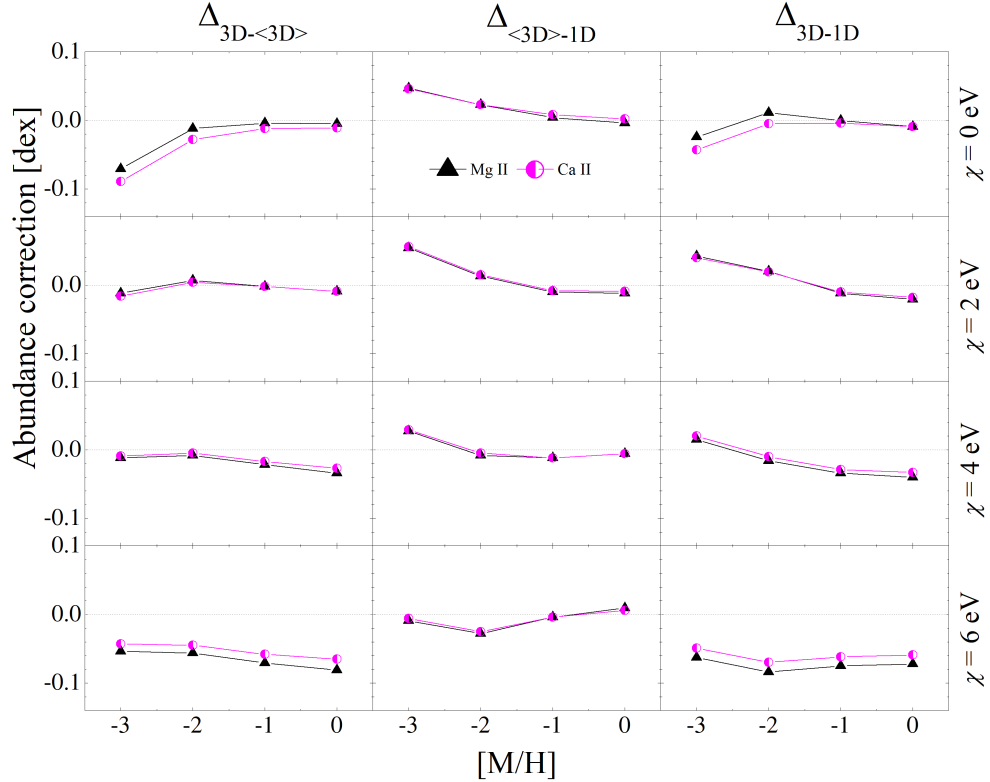


**Fig. 4.11.** The same as in Fig. 4.6 but for lines of ionized atoms at  $\lambda = 400$  nm, plotted versus metallicity and excitation potential.

the outer atmospheric layers of low metallicity model atmospheres, which result in large  $\Delta_{3D-(3D)}$ , and consequently, large  $\Delta_{3D-1D}$  corrections.

On the other hand, abundance corrections show little sensitivity to the line wavelength: the difference in abundance corrections at different  $\lambda$  does not exceed 0.1 dex. This is in contrast to our findings for the cooler red giant located close to the RGB tip ( $T_{\text{eff}} = 3600$  K,  $\log g = 1.0$ , and  $[M/H] = 0.0$ ; see Sect. 4.1) in which case the abundance corrections for IR lines were significantly lower than those obtained in the optical wavelength range.

The 3D–1D abundance corrections for neutral atoms are plotted in Fig. 4.11 for  $\lambda = 400$  nm, 4.12 for  $\lambda = 850$  nm, and 4.13 for  $\lambda = 1600$  nm. Three abundance corrections are given,  $\Delta_{3D-(3D)}$ ,  $\Delta_{(3D)-1D}$ , and  $\Delta_{3D-1D}$ , plotted at different values of metallicity and excitation potential,  $\chi$ .

Contrary to the situation with neutral atoms, abundance corrections of all ionized atoms are small and do not exceed  $\pm 0.01$  dex. Also, there is only very weak dependence on both metallicity and excitation potential. Spectral lines of ionized atoms form deeper in the atmosphere than those of neutral atoms do. In these atmospheric layers, horizontal inhomogeneities and differences between

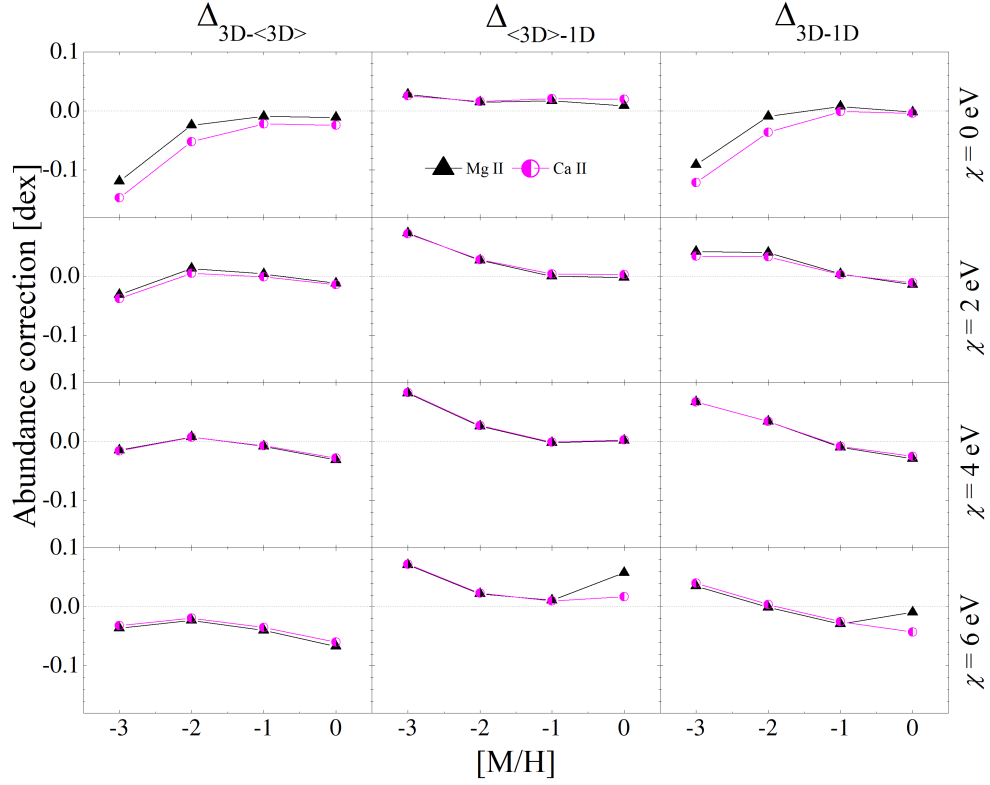


**Fig. 4.12.** The same as in Fig. 4.11 but at  $\lambda = 850$  nm.

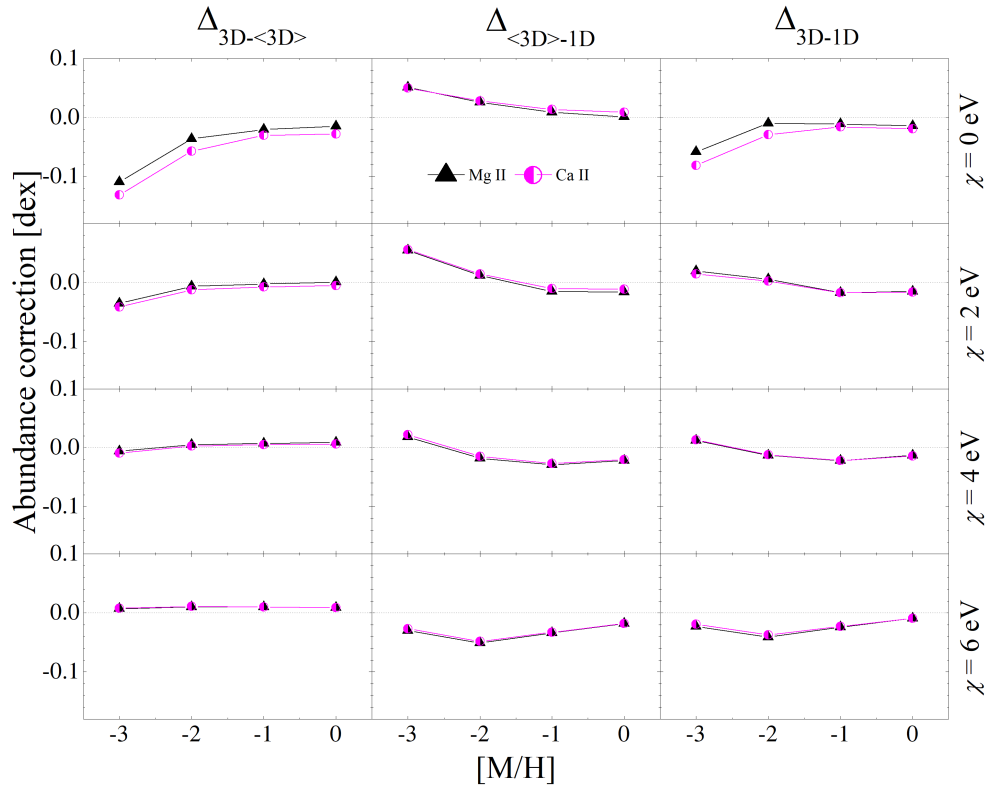


**Fig. 4.13.** The same as in Fig. 4.11 but at  $\lambda = 1600$  nm.

the temperature profiles of  $\langle 3D \rangle$  and 1D model atmospheres are smallest. As a result, abundance corrections show little dependence on  $[M/H]$  and  $\chi$ . High excitation lines of ions are expected to have largest sensitivity to temperature inhomogeneities for elements that are mostly ionized throughout the stellar atmosphere. Nevertheless, lines of such elements form in the deeper atmosphere where horizontal temperature inhomogeneities are small and thus have minor effect on the line strengths.

Importantly,  $\Delta_{3D-\langle 3D \rangle}$  and  $\Delta_{\langle 3D \rangle-1D}$  corrections usually are of opposite sign, especially at the lowest  $[M/H]$ , which leads to smaller total  $\Delta_{3D-1D}$  corrections. As  $\kappa_\ell$  is a non-linear function of temperature, horizontal inhomogeneities lead to the formation of stronger lines and, therefore, to negative  $\Delta_{3D-\langle 3D \rangle}$  corrections. However, temperature in the average  $\langle 3D \rangle$  model atmosphere is slightly lower than that in the 1D model throughout the entire line formation region. This results in stronger lines in 1D than in  $\langle 3D \rangle$  and, thus, leads to positive  $\Delta_{\langle 3D \rangle-1D}$  corrections. Just like with neutral lines, abundance corrections are essentially independent of line wavelength.

Generally, abundance corrections plotted in Figs. 4.6–4.13 are comparable to those obtained by Collet et al. (2007) for stellar atmospheres with parameters similar to those studied here. However, the corrections obtained in this work are almost always slightly lower. This can be a result of using different model atmosphere codes for computing 3D hydrodynamical model atmospheres used in the two studies, i.e., CO<sup>5</sup>BOLD in our investigation and STAGGER in Collet et al. (2007). Other differences include different opacities and their binning schemes, equations-of-state, etc. The reference 1D model atmospheres differ, too. While 1D hydrostatic LHD model atmospheres share the same microphysics (opacities, equation of state) as used in the computations of 3D hydrodynamical CO<sup>5</sup>BOLD model atmospheres, MARCS model atmospheres that were used by Collet et al. (2007) for computing 3D–1D corrections utilized different opacities and equation of state from those that were employed in the computations of the 3D hydrodynamical STAGGER models. Therefore, our results may in fact provide a more reliable picture of the spectral line formation under the influence of convection in the atmospheres of the red giant stars.



## Chapter 5

# The influence of convection and non-equilibrium radiative transfer on the formation of Li I 670.8 nm resonance doublet

Although convection has been shown to influence significantly the strengths of spectral lines of various chemical elements forming in the red giant atmospheres (Chapter 4), the combined effect of convection and non-equilibrium radiative transfer is yet to be investigated for a comparable range of chemical elements. Given that the spectral line formation in NLTE conditions is affected by non-local radiation field, one would expect a complex interplay between the 3D and NLTE effects in the spectral line formation. This may have various consequences in the light of stellar abundance analysis. For example, the detailed investigation of the interplay between convection and NLTE may reveal that adding 3D LTE–1D LTE and 1D NLTE–1D LTE abundance corrections, as is sometimes done to account for both 3D and NLTE effects, may be inaccurate.

We therefore performed a detailed study of the influence of convection and NLTE effects on the formation of Li I resonance doublet in the atmospheres of MS, TO, SGB and RGB stars. This line is the main tracer of primordial lithium abundance which is especially important in the cosmological context. From the perspective of convection effects discussed in the previous sections, low ionization potential of Li and the fact that the only indicator of its abundance in stellar spectra is a resonance line, makes the understanding of 3D and NLTE effects especially important.

### 5.1 Model atmospheres and spectral line synthesis

The 3D hydrodynamical models used in this part of our work were taken from the CIFIST CO<sup>5</sup>BOLD model atmosphere grid (Ludwig et al. 2009). All simulation runs covered  $\sim 13 - 480$  convective turnover times, as measured by the Brunt-Vaisälä timescale. We used 3D hydrodynamical and 1D hydrostatic models of the representative MS, TO, SGB, and RGB stars, in each case computed for the same  $\log g$ , at two different effective temperatures and metallicities (see

**Table 5.1.** 3D hydrodynamical CO<sup>5</sup>BOLD model atmospheres used in the study of Li I resonance doublet.

Model	$T_{\text{eff}}$ K	$\log g$	[M/H]	Grid size , Mm $x \times y \times z$	Grid resolution $x \times y \times z$
RGB #1	4480	2.5	0.0	851×851×295	140×140×150
RGB #2	4970	2.5	0.0	573×573×243	160×160×200
RGB #3	4480	2.5	-2.0	851×851×292	140×140×150
RGB #4	5020	2.5	-2.0	584×584×245	160×160×200
SGB #1	4920	3.5	0.0	59.7×59.7×30.2	140×140×150
SGB #2	5430	3.5	0.0	49.0×49.0×35.9	140×140×150
SGB #3	4980	3.5	-2.0	59.7×59.7×30.2	140×140×150
SGB #4	5500	3.5	-2.0	49.0×49.0×35.9	140×140×150
TO #1	5480	4.0	0.0	20.3×20.3×10.6	140×140×150
TO #2	6490	4.0	0.0	29.0×29.0×14.9	140×140×150
TO #3	5470	4.0	-2.0	20.1×20.1×10.6	140×140×150
TO #4	6530	4.0	-2.0	29.6×29.6×14.9	140×140×150
MS #1	6230	4.5	0.0	7.00×7.00×4.02	140×140×150
MS #2	4980	4.5	0.0	4.94×4.94×2.48	140×140×141
MS #3	6320	4.5	-2.0	7.00×7.00×4.02	140×140×150
MS #4	5010	4.5	-2.0	5.08×5.08×2.49	140×140×141

Table 5.1). This choice of the model parameters allowed us to bracket the range in  $T_{\text{eff}}$ ,  $\log g$ , and [M/H] typical of real stars observed in various Galactic populations (see Fig. 5.1). At the same time, this provides an opportunity to obtain a rough estimate of the size of 3D/1D and/or NLTE/LTE effects in real stellar atmospheres that are covered by our parameter range, by interpolating our results obtained at the bracketing values of stellar parameters. Atmospheric parameters of the 3D hydrodynamical CO<sup>5</sup>BOLD model atmospheres used in this study are given in Table 5.1, with their positions in the  $\log g - T_{\text{eff}}$  plane shown in Fig. 5.1. At each point in the  $\log g - T_{\text{eff}}$  diagram, calculations were performed using two models of different metallicity, [M/H] = 0.0 and -2.0, to assess the differential effect of metallicity on the lithium spectral line formation. The NLTE–LTE departure coefficients were computed using three types of model atmospheres:

- 3D hydrodynamical, calculated with the CO<sup>5</sup>BOLD code (Freytag et al. 2012);
- averaged ⟨3D⟩ atmospheres;
- 1D hydrostatic atmospheres, calculated using the LHD code (Caffau et al. 2008).

In most astrophysical situations, the only spectral line available for lithium

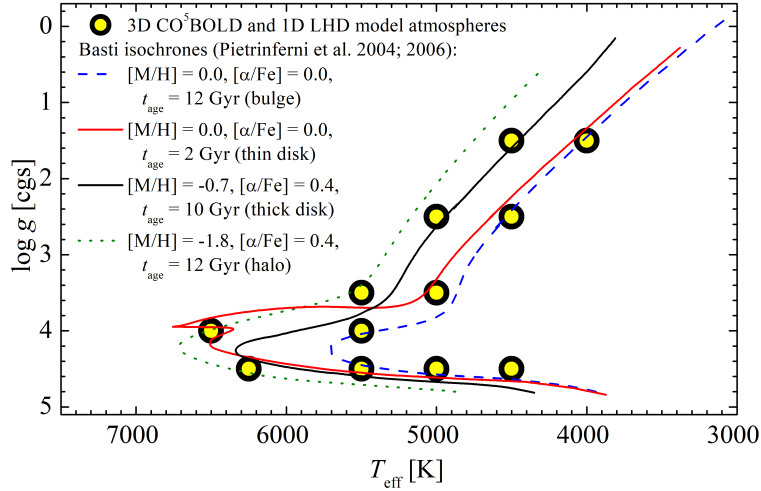


**Fig. 5.1.** 3D hydrodynamical CO<sup>5</sup>BOLD model atmospheres used in this study, plotted in the  $\log g - T_{\text{eff}}$  plane (large filled circles). Several isochrones are shown as lines to indicate the approximate loci of stars in various Galactic populations.

diagnostics in the UV–IR stellar spectra is the Li I 670.8 nm resonance doublet. We therefore focused on this single tracer by computing its synthetic 3D and 1D profiles with the Linfor3D spectral synthesis code, both in LTE and NLTE. The doublet structure of the Li I 670.8 nm resonance doublet was accounted for when computing the bound-bound radiative rates, while assuming identical NLTE departure coefficients for the two fine structure sublevels of the 2p level. The analysis was done using weak (equivalent width  $W = 0.5$  pm), and strong ( $W = 8$  pm) lines. These line strengths bracket the typical EWs of the Li I 670.8 nm resonance doublet observed in stars with the atmospheric parameters similar to those studied in this work. However, as we will see in Sect. 5.2, there is little sensitivity of the abundance corrections to the line strength for all model atmospheres.

The interplay between 3D hydrodynamical and NLTE effects was studied with the help of abundance corrections. The latter were defined as differences in Li abundance that would be determined from the Li I 670.8 nm resonance doublet of a given strength using different model atmospheres, in NLTE and/or LTE. First, we computed the following abundance corrections:  $\Delta_{3\text{D NLTE} - 1\text{D LTE}}$ ,  $\Delta_{1\text{D NLTE} - 1\text{D LTE}}$ , and  $\Delta_{3\text{D LTE} - 1\text{D LTE}}$ . Then, the latter two corrections were used to obtain the  $\Delta_{3\text{D} + \text{NLTE}} \equiv \Delta_{1\text{D NLTE} - 1\text{D LTE}} + \Delta_{3\text{D LTE} - 1\text{D LTE}}$  abundance correction, i.e., the total correction expected when the 1D NLTE abundances are corrected for 3D effects by adding the 3D–1D LTE abundance correction. Finally, we also calculated the  $\Delta_{\langle 3\text{D} \rangle \text{NLTE} - 1\text{D LTE}}$  abundance correction obtained by using the average  $\langle 3\text{D} \rangle$  and 1D model atmospheres. All obtained abundance correc-

tions are listed in Table 5.2.

We note that in this work we frequently used 1D LTE abundance estimates as the reference point for computing and assessing various abundance corrections. This choice may be well justified if one is interested in knowing how much the lithium abundances, which were obtained using various more sophisticated approaches, would differ from those determined in 1D LTE. At the same time, this may offer a convenient way to “correct” the 1D LTE abundances for 3D and/or NLTE effects. Nevertheless, it is clearly the full 3D NLTE approach that provides the highest realism in modeling lithium spectral line formation in stellar atmospheres. As such, ideally the 3D NLTE methods should be applied to obtain the most reliable lithium abundances from the measured equivalent widths of the Li I 670.8 nm lines.

## 5.2 The influence of convection and NLTE effects on the strength of Li I 670.8 nm resonance doublet

The results provided in Table 5.2 and Fig. 5.2 show that, in general, the full  $\Delta_{3\text{D NLTE} - 1\text{D LTE}}$  correction (Col. 6) is different from the  $\Delta_{3\text{D} + \text{NLTE}}$  ( $\equiv \Delta_{1\text{D NLTE} - 1\text{D LTE}} + \Delta_{3\text{D LTE} - 1\text{D LTE}}$ ) correction (Col. 5,) at all metallicities and in all model atmospheres studied here. We note, however, that while these differences between corrections are generally small at solar metallicity (MS #2 is a clear exception), they do indeed become significant at  $[M/H] = -2.0$ . In the latter case, the full 3D NLTE correction is small and, depending on the line strength, amounts to  $\Delta_{3\text{D NLTE} - 1\text{D LTE}} = -0.06 \dots + 0.12$  dex. At the same time, the  $\Delta_{3\text{D} + \text{NLTE}}$  correction is always large and negative, and may reach, for example, to  $\sim -0.18 \dots - 0.23$  dex and  $\sim -0.31 \dots - 0.50$  dex for RGB and TO stars, respectively. On the other hand, the  $\Delta_{(3\text{D})\text{NLTE} - 1\text{D LTE}}$  and the  $\Delta_{1\text{D NLTE} - 1\text{D LTE}}$  abundance corrections are in many cases very similar to the full  $\Delta_{3\text{D NLTE} - 1\text{D LTE}}$  correction: the differences are  $|\Delta_{3\text{D NLTE} - 1\text{D LTE}} - \Delta_{(3\text{D})\text{NLTE} - 1\text{D LTE}}| \leq 0.04$  dex and  $|\Delta_{3\text{D NLTE} - 1\text{D LTE}} - \Delta_{1\text{D NLTE} - 1\text{D LTE}}| \leq 0.08$  dex. Although these discrepancies are small, one should note that full  $\Delta_{3\text{D NLTE} - 1\text{D LTE}}$  corrections are of similar size, too, especially at  $[M/H] = -2.0$ . As a consequence, at lower metallicities the differences  $\Delta_{3\text{D NLTE} - 1\text{D LTE}} - \Delta_{(3\text{D})\text{NLTE} - 1\text{D LTE}}$  and  $\Delta_{3\text{D NLTE} - 1\text{D LTE}} - \Delta_{1\text{D NLTE} - 1\text{D LTE}}$  may become comparable to (or even exceed) the magnitude of the full  $\Delta_{3\text{D NLTE} - 1\text{D LTE}}$  corrections.

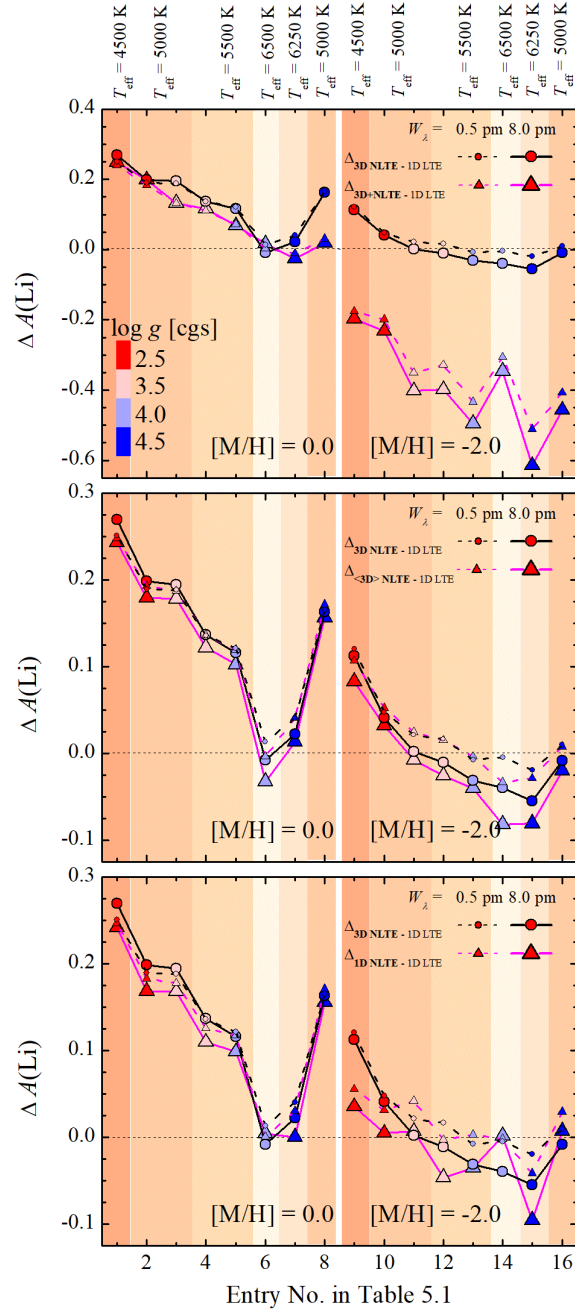


**Fig. 5.2.**  $\Delta_{3\text{D}^{\text{NLTE}} - 1\text{D}^{\text{LTE}}}$  (shown in all panels),  $\Delta_{3\text{D}^{\text{NLTE}} - 1\text{D}^{\text{LTE}}}$  (top),  $\Delta_{(3\text{D})^{\text{NLTE}} - 1\text{D}^{\text{LTE}}}$  (middle) and  $\Delta_{1\text{D}^{\text{NLTE}} - 1\text{D}^{\text{LTE}}}$  (bottom) abundance corrections for the lithium 670.8 nm resonance doublet in the spectra of MS, TO, SGB, and RGB stars, at  $[\text{M}/\text{H}] = 0.0$  and  $-2.0$ , in the order they appear in Table 5.2. Different background shades denote  $T_{\text{eff}}$  of the model atmospheres while different symbol colors mark different values of  $\log g$ .

**Table 5.2.** Abundance corrections for the lithium 670.8 nm resonance doublet in the spectra of MS, TO, SGB, and RGB stars, at  $[M/H] = 0.0$  and  $-2.0$ . The microturbulence velocity used in the  $\langle 3D \rangle$  and 1D line synthesis was set to 2 km/s.

Entry No.	$W$	$\Delta_{1DNLTE-1DLTE}$	$\Delta_{3DLTE-1DLTE}$	$\Delta_{3D+NLTE}$	$\Delta_{3DNLTE-1DLTE}$	$\Delta_{\langle 3D \rangle NLTE-1DLTE}$
	pm	dex	dex	dex	dex	dex
(1)	(2)	(3)	(4)	(5)	(6)	(7)
1	RGB #1: $T_{\text{eff}} = 4480$ K, $\log g = 2.5$ , $[M/H] = 0.0$					
	0.5	0.247	-0.008	0.239	0.251	0.248
	8.0	0.242	0.007	0.249	0.269	0.243
2	RGB #2: $T_{\text{eff}} = 4970$ K, $\log g = 2.5$ , $[M/H] = 0.0$					
	0.5	0.183	0.001	0.184	0.190	0.193
	8.0	0.168	0.030	0.199	0.199	0.180
3	SGB #1: $T_{\text{eff}} = 4920$ K, $\log g = 3.5$ , $[M/H] = 0.0$					
	0.5	0.178	-0.047	0.131	0.189	0.187
	8.0	0.168	-0.036	0.132	0.195	0.178
4	SGB #2: $T_{\text{eff}} = 5430$ K, $\log g = 3.5$ , $[M/H] = 0.0$					
	0.5	0.126	-0.015	0.111	0.136	0.136
	8.0	0.110	0.007	0.117	0.137	0.122
5	TO #1: $T_{\text{eff}} = 5480$ K, $\log g = 4.0$ , $[M/H] = 0.0$					
	0.5	0.117	-0.045	0.072	0.121	0.120
	8.0	0.099	-0.030	0.068	0.116	0.103
6	TO #2: $T_{\text{eff}} = 6490$ K, $\log g = 4.0$ , $[M/H] = 0.0$					
	0.5	0.001	0.002	0.003	0.013	-0.004
	8.0	0.004	0.012	0.016	-0.008	-0.033
7	MS #1: $T_{\text{eff}} = 6230$ K, $\log g = 4.5$ , $[M/H] = 0.0$					
	0.5	0.030	-0.041	-0.011	0.040	0.041
	8.0	0.000	-0.026	-0.026	0.022	0.013

*Continued on next page*

Entry No.	$W$	$\Delta_{\text{IDLTE-1DLTE}}$	$\Delta_{\text{3DLTE-1DLTE}}$	$\Delta_{\text{3D+NLTE}}$	$\Delta_{\text{3DNLTE-1DLTE}}$	$\Delta_{\text{(3D)NLTE-1DLTE}}$
	pm	dex	dex	dex	dex	dex
(1)	(2)	(3)	(4)	(5)	(6)	(7)
8	MS #2: $T_{\text{eff}} = 4980$ K, $\log g = 4.5$ , $[\text{M}/\text{H}] = 0.0$					
	0.5	0.171	-0.140	0.031	0.166	0.172
	8.0	0.155	-0.137	0.019	0.163	0.157
9	RGB #3: $T_{\text{eff}} = 4480$ K, $\log g = 2.5$ , $[\text{M}/\text{H}] = -2.0$					
	0.5	0.056	-0.231	-0.176	0.121	0.107
	8.0	0.035	-0.232	-0.197	0.113	0.083
10	RGB #4: $T_{\text{eff}} = 5020$ K, $\log g = 2.5$ , $[\text{M}/\text{H}] = -2.0$					
	0.5	0.031	-0.230	-0.199	0.048	0.052
	8.0	0.005	-0.237	-0.232	0.041	0.032
11	SGB #3: $T_{\text{eff}} = 4980$ K, $\log g = 3.5$ , $[\text{M}/\text{H}] = -2.0$					
	0.5	0.042	-0.393	-0.351	0.021	0.025
	8.0	0.007	-0.409	-0.402	0.002	-0.008
12	SGB #4: $T_{\text{eff}} = 5500$ K, $\log g = 3.5$ , $[\text{M}/\text{H}] = -2.0$					
	0.5	-0.003	-0.325	-0.328	0.017	0.015
	8.0	-0.046	-0.352	-0.398	-0.011	-0.026
13	TO #3: $T_{\text{eff}} = 5470$ K, $\log g = 4.0$ , $[\text{M}/\text{H}] = -2.0$					
	0.5	0.003	-0.437	-0.434	-0.008	-0.004
	8.0	-0.036	-0.460	-0.495	-0.031	-0.040
14	TO #4: $T_{\text{eff}} = 6530$ K, $\log g = 4.0$ , $[\text{M}/\text{H}] = -2.0$					
	0.5	-0.002	-0.304	-0.306	-0.004	-0.004
	8.0	0.002	-0.348	-0.346	-0.040	-0.082
15	MS #3: $T_{\text{eff}} = 6320$ K, $\log g = 4.5$ , $[\text{M}/\text{H}] = -2.0$					
	0.5	-0.040	-0.470	-0.510	-0.019	-0.029
	8.0	-0.094	-0.520	-0.614	-0.055	-0.081
16	MS #4: $T_{\text{eff}} = 5010$ K, $\log g = 4.5$ , $[\text{M}/\text{H}] = -2.0$					
	0.5	0.030	-0.437	-0.407	0.010	0.008
	8.0	0.007	-0.464	-0.457	-0.008	-0.020

The behavior of different abundance corrections shown in Table 5.2 is relatively easy to understand. As seen from Fig. 5.3 and 5.4, the metal content plays a significant role in shaping the structure of the photospheric layers where the Li I line forms in RGB and TO stars. At solar metallicity, the mean temperature of the 3D models of RGB and TO stars is close to the 1D radiative equilibrium solution, and the amplitude of the horizontal temperature inhomogeneities in both cases is moderate,  $\Delta T_{\text{RMS}} < 350$  K ( $\Delta T_{\text{RMS}} = \sqrt{\langle (T - T_0)^2 \rangle_{x,y,t}}$ , where the angled brackets indicate temporal and horizontal averaging on surfaces of equal optical depth, and  $T_0 = \langle T \rangle_{x,y,t}$  is the depth-dependent average temperature). In the metal-poor TO model atmosphere, the mean temperature of the 3D model is significantly lower than that predicted in 1D (up to 700 K), and at the same time the horizontal temperature inhomogeneities are substantial, increasing with height to  $\Delta T_{\text{RMS}} > 800$  K (Fig. 5.4, second panels from top). Assuming LTE, both effects lead to significant line strengthening in 3D with respect to 1D in the metal-poor case. This happens because line opacity is a very sensitive non-linear function of temperature. Therefore, even if temperature had a symmetric distribution around the mean value at a given optical depth, the contribution from the low- $T$  regions (e.g., inter-granular lanes) towards the total opacity would be more important than that from the high- $T$  regions (e.g., granules). As a consequence, the net increase of line opacity in the former would outweigh the net decrease of line opacity in the latter. This would make lines appear stronger in 3D than in  $\langle 3D \rangle$  or 1D and would result in negative  $\Delta_{3\text{DLTE} - \langle 3D \rangle \text{LTE}}$  and  $\Delta_{3\text{DLTE} - 1\text{DLTE}}$  abundance corrections (see, e.g., Steffen & Holweger 2002; Kučinskas et al. 2013). The situation is similar in the atmosphere of RGB star, although the line strengthening in 3D is slightly smaller in this case. This is because the difference between the temperature profiles of the average  $\langle 3D \rangle$  and 1D model atmospheres is small and only the temperature inhomogeneities contribute to the line strengthening. Qualitatively, the effect is similar in all other model atmospheres studied here. Note, however, that the situation is different in NLTE (see below).

Comparison of the line contribution functions obtained in LTE (see Fig. 5.3 and 5.4) reveals their close similarity at  $[M/H] = 0.0$ . Consequently, one may infer that the effect of the horizontal temperature inhomogeneities is small at solar metallicity. Nevertheless, the line contribution functions in 3DLTE and  $\langle 3D \rangle$  LTE are significantly different at  $[M/H] = -2.0$ , both in RGB and TO

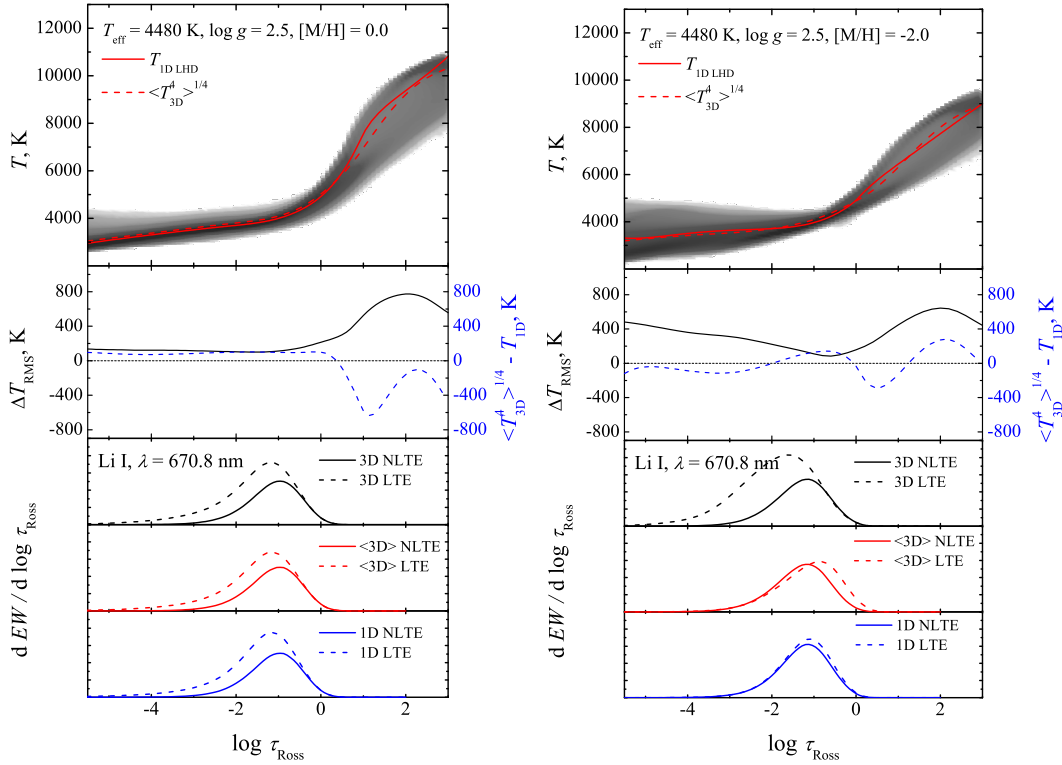


**Fig. 5.3.** Thermodynamic structures and Li 670.8 nm resonance doublet formation properties in two model atmospheres of red giant stars ( $T_{\text{eff}} = 4480$  K,  $\log g = 2.5$ ), at  $[M/H] = 0.0$  (left) and  $[M/H] = -2.0$  (right). **From top to bottom:** (1) temperature profiles in the 3D hydrodynamical (probability density, grayscale), average  $\langle 3D \rangle$  (dashed red line), and 1D LHD (solid red line) model atmospheres; (2) horizontal temperature inhomogeneities in the 3D model ( $\Delta T_{\text{RMS}}$ , solid black line) and differences between the temperature profiles of the  $\langle 3D \rangle$  and 1D LHD model atmospheres (blue dashed lines); (3–5) contribution functions of the Li 670.8 nm resonance doublet (i.e., rate of the line equivalent width growth,  $dEW/d \log \tau_{\text{Ross}}$ , as a function of Rosseland optical depth) in 3D NLTE/LTE (black),  $\langle 3D \rangle$  NLTE/LTE (red), and 1D NLTE/LTE (blue). For each metallicity, the lithium abundance is fixed such that  $W(1D \text{ LTE}) = 0.5$  pm.

stars, which shows that the role of horizontal inhomogeneities now becomes substantial and dominates over the effect of the reduced mean temperature. In the metal-poor 3D hydrodynamical models, the inhomogeneities produce regions in the atmosphere where temperature drops significantly below that predicted by the 1D model. This leads to larger concentration of Li I in the 3D models, and thus, to stronger lines in 3D LTE (i.e., with respect to those in 1D LTE) and negative  $\Delta_{3D \text{ LTE} - 1D \text{ LTE}}$  abundance corrections.

In NLTE (both 1D and 3D), however, atomic level population numbers are more sensitive to the average radiation field than to local temperature (e.g., Cayrel & Steffen 2000; Asplund et al. 2003). As a consequence, Li I gets significantly over-ionized in the outer atmosphere. Therefore, the mean concentration

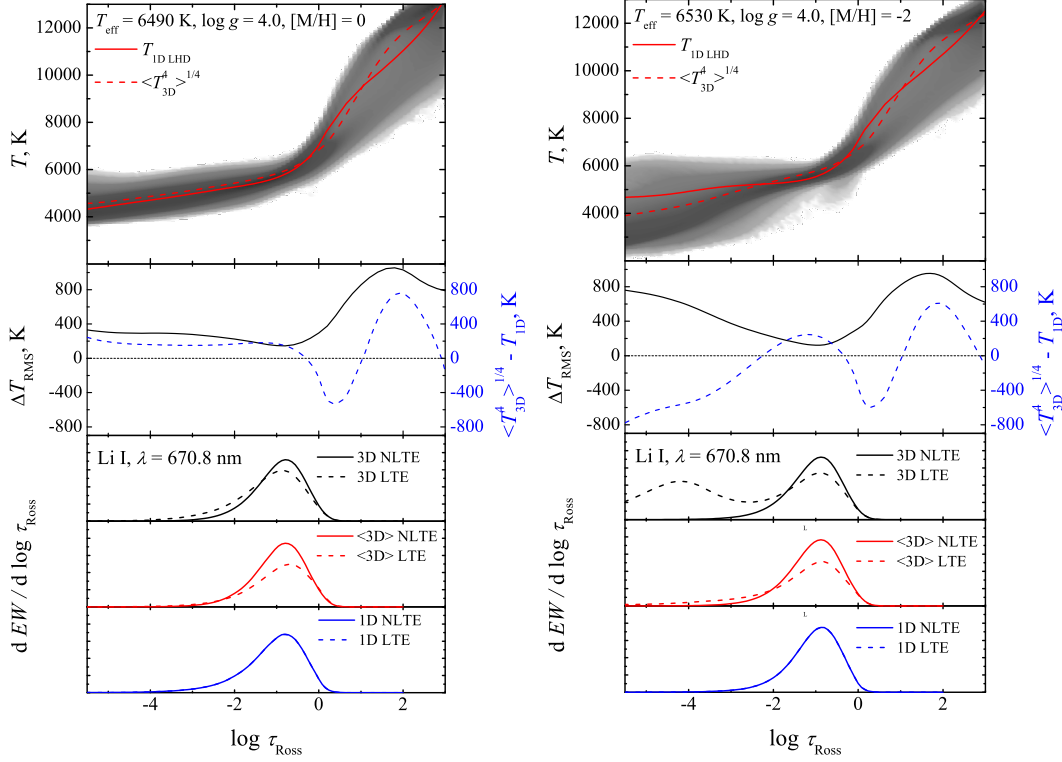


**Fig. 5.4.** Same as in Fig. 5.3, but for TO stars.

of Li I with respect to what would be expected in LTE is reduced. This leads to weaker spectral lines in 3D NLTE than in 3D LTE, and thus, significantly reduced  $\Delta_{3\text{D NLTE}} - 1\text{D LTE}$  abundance corrections which are similar in magnitude to  $\Delta_{1\text{D NLTE}} - 1\text{D LTE}$  corrections.

It is important to note that, in general, the choice of microturbulence velocity used in the spectral line synthesis with the average  $\langle 3\text{D} \rangle$  and 1D model atmospheres may influence the corresponding abundance corrections. Fortunately, the resonance line of lithium observed in stars covered by our atmospheric parameter range is relatively weak, and so the influence of microturbulence on the line strength is, in fact, minor. Our tests show that the difference in the abundance correction obtained at microturbulence velocities of 1.0 km/s and 5.0 km/s is small,  $\lesssim 0.05$  dex. The difference in abundance corrections computed at more typical values of 1.0 and 2.0 km/s was less than 0.02 dex, irrespective of whether the line formation was treated in NLTE or LTE, even for lines as strong as  $W \approx 8$  pm. This illustrates that saturation of the stronger line of the Li I 670.8 nm doublet is not significant in the range of  $W$ s investigated. However, in the Li-rich stars, this line may become saturated and may thus experience an enhanced sensitivity to microturbulence and larger non-LTE effects due to photon losses (e.g., Lind et al. 2009).

The size of uncertainties involved in 3D NLTE spectral synthesis (excluding uncertainties in atomic data) can be very roughly estimated by comparing Li abundance corrections,  $\Delta_{3\text{DNLTE} - 1\text{DLTE}}$ , computed in this work with those obtained using the interpolation formula from Sbordone et al. (2010, Eq. B.1). This formula is based on the 3D NLTE and 1D LTE spectral synthesis computations obtained using a grid of 3D hydrodynamical CO<sup>5</sup>BOLD and 1D hydrostatic LHD model atmospheres of dwarfs and subgiant stars ( $T_{\text{eff}} \approx 5470 \dots 6560$  K,  $\log g = 3.5 \dots 4.5$ ,  $[M/H] = -2.0$ ). Spectral synthesis computations of Sbordone et al. (2010) utilized departure coefficients computed with a simpler Li model atom and an older version of the NLTE3D code, treating continuum scattering as true absorption. Their formula is supposed to have an internal precision of  $\approx \pm 0.005$  dex as long as extrapolation towards the values of equivalent widths and atmospheric parameters that are not covered in their simulations is avoided (see Fig. 6 and 7 in Sbordone et al. 2010). For this comparison we used models #12, 13, 14, and 15 from our grid, because their atmospheric parameters fall in the range covered by the simulations of Sbordone et al. (2010). We find that corrections obtained in this work differ from those computed using the formula of Sbordone et al. (2010) by  $-0.027 \pm 0.012$  dex on average for lines with  $W = 5$  pm and by  $-0.055 \pm 0.017$  dex for lines with  $W = 8$  pm, without a notable systematic dependence on atmospheric parameters. The larger disagreement in the case of stronger lines is not unexpected since, in the present calculations of the departure coefficients, we have taken the doublet fine structure of the 670.8 nm line into account, while the single component approximation used by Sbordone et al. (2010) is only valid for weak lines, and consequently Sbordone et al. (2010) do not recommend using their interpolation formula when saturation effects become important.

### 5.3 The influence of scattering on the Li I 670.8 nm resonance doublet strength

To check the importance of continuum scattering for the Li I statistical equilibrium solution, we computed an additional set of synthetic spectra where the departure coefficients were computed by treating scattering as true absorption. While we refer to the treatment of scattering as “consistent”<sup>1</sup>, we note that simplifications are still involved, such as assuming that scattering is isotropic. Key

---

<sup>1</sup>By “consistent” it is meant that part of scattered radiation is scattered back along the ray direction.

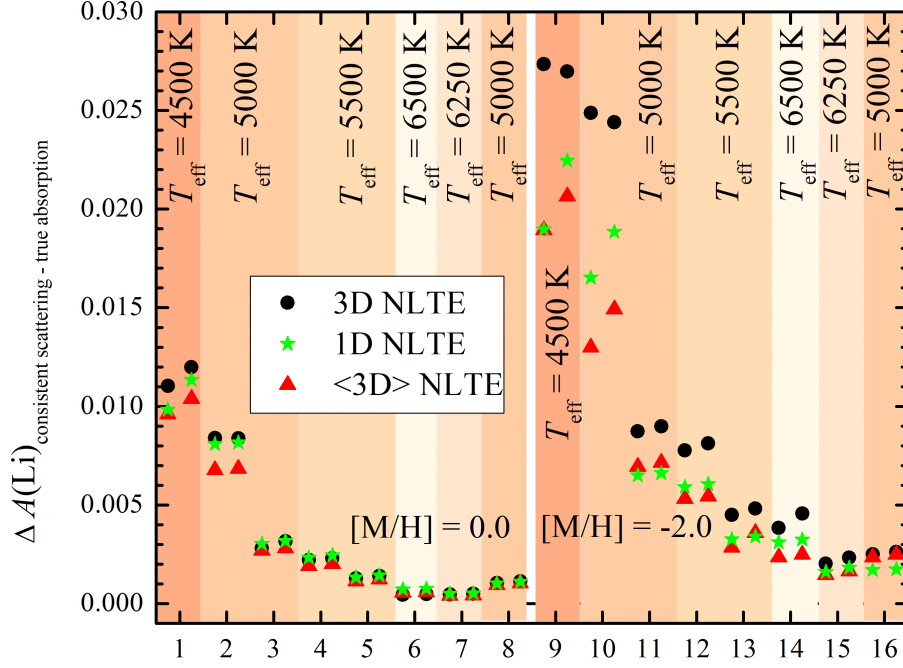


**Fig. 5.5.** Changes in  $A(\text{Li})$  when different treatments of continuum scattering are applied in the calculations of departure coefficients (consistent scattering minus true absorption). Differently shaded areas represent different model atmospheres as they are listed in Table 5.2. Symbols on the left side of each shaded region represent spectral lines with  $W = 0.5$  pm, while symbols on the right represent those with  $W = 8.0$  pm.

difference in the treatment of scattering as true absorption is that scattered fraction of light is reintroduced into the radiation field, thus requiring iterative solution of radiative transfer equation.

It appears nevertheless that the effect of scattering on the estimates of Li abundance in 3D,  $\langle 3D \rangle$ , and 1D is relatively small<sup>2</sup>, as shown in Fig. 5.5: at solar metallicity, the differences in abundance increase from about 0.001 dex in the dwarfs to up to 0.012 dex in the giants, while a more pronounced effect of scattering is seen in the metal-poor stars, where the abundance differences range from 0.005 dex in the dwarfs to 0.028 dex in the giants. This is because, especially in the metal-poor giants, the opacity coefficients of continuum scattering and absorption become comparable in magnitude. However, the effect on the abundance corrections (e.g.,  $\Delta_{3D\text{NLTE}} - \Delta_{1D\text{NLTE}}$ ) is much smaller and does not exceed 0.002 dex, except for the two metal-poor giants. Qualitatively, these results are similar to those obtained by Hayek et al. (2011) who found that the impact of scattering on the formation of fictitious Fe I resonance lines in the atmosphere of

<sup>2</sup>Convergence limits for the computations of  $J_\nu$  and  $W$  were set at 0.01 % and 0.001 %, respectively, to ensure the precision of 0.001 dex or better in the computed abundance corrections.

red giant star is negligible at 500 nm ( $[M/H] = -2.0$  and  $0.0$ ), both in 3D and 1D, with the resulting differences in the abundance corrections of  $< 0.015$  dex. In general, we find that 3D spectral line formation is slightly more sensitive to scattering effects compared to 1D, such that the abundance corrections are slightly more positive when continuum scattering is treated consistently. It is important to note that these results should not be used as corrections to account for scattering effects. The absolute values of these abundance corrections are below our upper limit of the expected uncertainty of 0.01 dex due to non-stationary nature of 3D model atmospheres.



## Summary and conclusions

We studied the influence of convection and radiative transfer on the formation of spectral lines in the atmospheres of different types of stars, covering a wide range in the atmospheric and spectral line parameters. For this purpose we used 3D hydrodynamical model atmospheres, which allowed to model convection in an explicit way. We also used 1D hydrostatic model atmospheres where convection was modeled using various simplifying assumptions.

The obtained results show that coreshifts and bisectors of Fe I lines predicted by the current 3D hydrodynamical CO<sup>5</sup>BOLD model atmospheres agree reasonably well with those observed in the metal-poor red giant HD 122563, despite the minor discrepancies in cases of the weakest and strongest spectral lines. These results are compatible with those obtained in a similar study of line asymmetries in HD 122563 carried out using 3D hydrodynamical STAGGER model atmospheres (Ramírez et al. 2010), pointing to the consistency in the predictions made with two different 3D hydrodynamical model atmosphere codes. These results suggest that the current level of physical realism of the 3D hydrodynamical model atmospheres is sufficient to warrant further applications of the 3D model atmospheres in solving various astrophysical problems, to further test their realism and identify problems where additional improvements may be needed.

We have investigated the influence of convection on the spectral line formation in the atmosphere of a red giant located at the RGB tip ( $T_{\text{eff}} = 3660$  K,  $\log g = 1.0$ ,  $[M/H] = 0.0$ ). The influence of convection on the line formation was investigated by measuring the differences in abundances that would be obtained using 3D hydrodynamical and 1D hydrostatic model atmospheres from the same weak fictitious spectral line of a given chemical element.

In 3D hydrodynamical model atmospheres, convection and related dynamical phenomena cause significant horizontal temperature inhomogeneities seen at different optical depths in the atmosphere. This results in significant horizontal variations in the number densities of minority chemical species, causing significant deviations from the predictions of the classical 1D models. Typically, abundance corrections for the neutral atoms do not exceed  $\Delta_{3\text{D}-1\text{D}} \approx \pm 0.1$  dex. The abundance corrections are smaller in the near-infrared at  $\lambda 1600$  nm than those in the optical spectral range. The strong wavelength dependence of the 3D

corrections is related to the fact that continuum opacity is much more temperature dependent at  $\lambda$  1600 nm (mainly  $H^-$  free-free absorption) than at  $\lambda$  850 nm (mainly  $H^-$  bound-free absorption).

The same technique was applied to study line formation in the atmospheres of red giant stars located in the lower part of the RGB ( $T_{\text{eff}} \approx 5000$  K,  $\log g = 2.5$ ), at four different metallicities,  $[M/H] = 0.0, -1.0, -2.0, -3.0$ . Abundance corrections in this case were computed for Li I, Na I, Mg I, Al I, K I, Ca I, Ca II. The abundance corrections for the low-excitation lines of neutral atoms show significant dependence on both metallicity and line excitation potential, especially at low metallicities where differences in the abundances obtained with the 3D and 1D model atmospheres,  $\Delta_{3D-1D}$ , may reach  $-0.8$  dex. For ionized atoms, the abundance corrections are small at all metallicities and excitation potentials ( $\leq \pm 0.1$  dex) and vary little with either  $[M/H]$  or  $\chi$ . The obtained abundance corrections show little variation with wavelength. This is in contrast to what was obtained in case of cooler red giant located at the RGB tip, for which the corrections at 1600 nm were significantly smaller than in the optical wavelength range.

To quantify the combined effects of convection and non-equilibrium radiative transfer, we investigated the formation of Li I resonance line ( $\lambda = 670.8$  nm) in the atmospheres of MS, TO, SGB, and RGB stars. Our results show that both effects are important in the Li I line formation. We also find that the application of the combined  $\Delta_{3D+NLTE}$  correction may lead to erroneous results in the case of lithium at sub-solar metallicities, with all model atmospheres studied here. On the other hand, both  $\langle 3D \rangle$  NLTE and 1D NLTE approaches provide a good approximation to the full 3D NLTE solution.

Our results suggest that, in most cases,  $\langle 3D \rangle$  NLTE or 1D NLTE modeling may be sufficient for deriving lithium abundances accurate to  $\sim 0.1$  dex, i.e., with respect to those that would be expected in 3D NLTE. Nevertheless, since the full  $\Delta_{3DNLTE-1DLTE}$  correction, in certain cases, is only slightly larger than 0.1 dex, application of  $\Delta_{1DNLTE-1DLTE}$  or  $\Delta_{\langle 3D \rangle NLTE-1DLTE}$  corrections may lead to systematical bias that is comparable to the size of the  $\Delta_{3DNLTE-1DLTE}$  correction itself. This may be obviously unacceptable when high accuracy/reliability in lithium abundances is needed. Ideally, the full 3D NLTE analysis should be preferred over any of the approximate approaches.

We stress that the results obtained in the Thesis apply to study stars with the atmospheric parameters within the range of those that were investigated in our

study. However, it is still unclear how convection would influence line formation for spectral lines forming in stellar atmospheres characterized by significantly different sets of parameters. Nevertheless, our current results clearly suggest that it is extremely important to take into account the combined effects of convection and non-equilibrium radiative transfer together, because as our study of Li I line formation has shown, the complex interplay between the two effects can not be modeled using other, simplified approaches. The use of  $\langle 3D \rangle$  NLTE or 1D NLTE approaches, moreover, cannot be extended in a straightforward fashion to other chemical elements: the importance of different physical processes leading to the departures from LTE may vary from one chemical element to another. As we have seen from the results obtained in our study (which are in line with the earlier findings of, for example, Asplund et al. 2003), the 3D–1D and NLTE–LTE abundance corrections generally tend to compensate each other, so that the total  $\Delta_{3DNLTE - 1DLTE}$  abundance correction is small. This, however, seems not to be the case with other elements where this kind of compensation does not occur. For example, in their study of NLTE Fe I spectral line formation based on a comparison with the observed spectra, Mashonkina et al. (2013) find the  $\langle 3D \rangle$  NLTE approach is only applicable to a limited subset of Fe I lines. Therefore, verification with the full 3D NLTE approach is needed on a case-by-case basis before any simplified approach may be applied with confidence to the abundance analysis of other elements in the atmospheres of real stars.



## References

- Allen, C. W. 1973, *Astrophysical quantities*, University of London, Athlone Press, London
- Amarsi, A. M., Asplund, M., Collet, R., & Leenaarts, J. 2016, *MNRAS*, 455, 3735
- Asplund, M., Nordlund, Å., Trampedach, R., Allende Prieto, C., & Stein, R. F. 2000, *A&A*, 359, 729
- Asplund, M., Carlsson, M., & Botnen, A. V. 2003, *A&A*, 399, L31
- Asplund, M., Grevesse, N., Sauval, A. J., Allende Prieto, C., & Kiselman, D. 2004, *A&A*, 417, 751
- Asplund, M., Grevesse, N., & Sauval, A. J. 2005, *ASPC*, 336, 25
- Barklem, P. S., Belyaev, A. K., & Asplund, M. 2003, *A&A*, 409, L1
- Behara, N. T., Bonifacio, P., Ludwig, H.-G., et al. 2010, *A&A*, 513, 72
- Böhm-Vitense, E. 1958, *ZAp*, 46, 108
- Brott, I., & Hauschildt, P. H. 2005, in: 'The Three-Dimensional Universe with Gaia', eds. C. Turon, K.S. O'Flaherty, & M.A.C. Perryman, *ESA SP 576*, 565
- Caffau, E., Ludwig, H.-G., Steffen, M., et al. 2008, *A&A*, 488, 1031
- Caffau, E., Ludwig, H.-G., Steffen, M., Freytag, B., & Bonifacio, P. 2011, *SoPh*, 268, 255
- Castelli, F., & Kurucz, R. L. 2003, in: 'Modeling of Stellar Atmospheres', *Proc. IAU Symp. 210*, eds. N.E. Piskunov, W. W. Weiss, & D. F. Gray, poster A20 (CD-ROM); synthetic spectra available at <http://cfaku5.cfa.harvard.edu/grids>
- Castelli, F. 2005, *Memorie della Societa Astronomica Italiana Supplementi*, 8, 34
- Cayrel, R., & Steffen, M. 2000, *Proc. IAU Symp.*, 198, 437

Cayrel, R., Steffen, M., Chand, H., et al. 2007, *A&A*, 473, L37

Collet, R., Asplund, M., & Trampedach, R. 2007, *A&A*, 469, 687

Creevey, O. L., Thévenin, F., Boyajian, T. S., et al. 2012, *A&A*, 545, A17

Cunto, W., Mendoza, C., Ochsenbein, F., & Zeipen, C. J. 1993, *A&A*, 275, L5

Dobrovolskas, V., Kučinskas, A., Ludwig, H.-G., et al. 2010, Proc. of 11th Symposium on Nuclei in the Cosmos, Proceedings of Science, ID 288 (arXiv:1010.2507)

Dobrovolskas, V., Kučinskas, A., Steffen, M., et al. 2013, *A&A*, 559, A102

Freytag, B., Steffen, M., Ludwig, H.-G., et al. 2012, *J. Comp. Phys.*, 231, 919

González Hernández, J. I., Bonifacio, P., Caffau, E., et al. 2009, *A&A*, 505, 13

Gray, D. F. 1983, *PASP*, 95, 252

Gray, D. F. 2005, *The Observation and Analysis of Stellar Photospheres*, 3rd Edition, Cambridge University Press

Grevesse, N., & Sauval, A. J. 1998, *Space Sci. Rev.*, 85, 161

Gustafsson, B., Edvardsson, B., Eriksson, K., et al. 2008, *A&A*, 486, 951

Hayek, W., Asplund, M., Collet, R., & Nordlund, A. 2011, *A&A*, 529, A158

Holzreuter, R., & Solanki, S. K. 2013, *A&A*, 558, A20

Ivanauskas, A., Kučinskas, A., Ludwig, H.-G., & Caffau, E. 2010, Proc. of 11th Symposium on Nuclei in the Cosmos, Proceedings of Science, ID 290 (arXiv:1010.1722)

Kervella, P., Verhoelst, T., Ridgway, S. T., et al. 2009, *A&A*, 504, 115

Kučinskas, A., Hauschildt, P. H., Ludwig, H.-G., et al. 2005, *A&A*, 442, 281

Kučinskas, A., Steffen, M., Ludwig, H.-G., et al. 2013, *A&A*, 549, A14

Kupka, F., Piskunov, N., Ryabchikova, T. A., Stempels, H. C., & Weiss, W. W. 1999, *A&AS*, 138, 119

Lambert, D. L. 1993, *Phys. Scr.*, 47, 186

- van Leeuwen, F. 2007, *A&A*, 474, 653
- Lind, K., Asplund, M., & Barklem, P. S. 2009, *A&A*, 503, 541
- Lind, K., Asplund, M., Collet, R., & Melendez, J. 2012, *Mem. Soc. Astron. ItalianaSuppl.*, 22, 124
- Lind, K., Melendez, J., Asplund, M., Collet, R., & Magic, Z. 2013, *A&A*, 554, A96
- Ludwig, H.-G. 1992, *Non-gray Radiation Transport in Numerical Simulations of Stellar Convection*, Ph.D. Thesis, University of Kiel
- Ludwig, H.-G. & Kučinskas, A. 2012, *A&A*, 547, A118
- Ludwig, H.-G., Jordan, S., & Steffen, M. 1994, *A&A*, 284, 105
- Ludwig, H.-G., Allard, F., & Hauschildt, P. H. 2002, *A&A*, 395, 99
- Ludwig, H.-G., Caffau, E., Steffen, M., et al. 2009, *Mem. Soc. Astron. Italiana*, 80, 711
- Mashonkina, L., Gehren, T., Shi, J.-R., Korn, A. J., & Grupp, F. 2011, *A&A*, 528, A87
- Mashonkina, L., Ludwig, H.-G., Korn, A., Sitnova, T., & Caffau, E. 2013, *Memorie della Societa Astronomica Italiana Supplementi*, 24, 120
- Mihalas, D. 1978, *Stellar Atmospheres*, Freeman and Company, p. 186
- Mucciarelli, A., Salaris, M., & Bonifacio, P. 2012, *MNRAS*, 419, 2195
- Nave, G., Johansson, S., Learner, R. C. M., Thorne, A. P., & Brault, J. W. 1994, *ApJS*, 94, 221
- Nordlund, Å. 1982, *A&A*, 107, 1
- Osorio, Y., Barklem, P. S., Lind, K., & Asplund, M. 2011, *A&A*, 529, A31
- Pietrinferni, A., Cassisi, S., Salaris, M., & Castelli, F. 2004, *ApJ*, 612, 168
- Pietrinferni, A., Cassisi, S., Salaris, M., & Castelli, F. 2006, *ApJ*, 642, 797
- Prakapavičius, D., Steffen, M., Kučinskas, A., et al. 2013, *Mem. Soc. Astron. ItalianaSuppl.*, 24, 111

- Ramírez, I., Collet, R., Lambert, D. L., Allende Prieto, C., & Asplund, M. 2010, *ApJ*, 725, L223
- van Regemorter, H. 1962, *ApJ*, 136, 906
- Sbordone, L., Bonifacio, P., Caffau, E., et al. 2010, *A&A*, 522, 26
- Seaton, M. J. 1962, *Proc. Phys. Soc.*, 79, 1105
- Short, C. I., & Hauschildt, P. H. 2006, *ApJ*, 641, 494
- Steffen, M., & Holweger, H. 2002, *A&A*, 387, 258
- Steffen, M., & Holweger, H. 2003, *IAUS, Modelling of Stellar Atmospheres*, 210, 15P
- Steffen, M., Ludwig, H.-G., & Freytag, B. 1995, *A&A*, 300, 473
- Steffen, M., Cayrel, R., Bonifacio, P., Ludwig, H.-G., & Caffau, E. 2010, *Proc. IAU Symp.*, 268, 215
- Steffen, M., Cayrel, R., Caffau, E., et al. 2012, *Mem. Soc. Astron. Italiana*, 22, 152
- Steffen, M., Prakashavičius, D., Caffau, E., et al. 2015, *A&A*, in press
- Vögler, A., Bruls, J. H. M. J., & Schüssler, M. 2004, *A&A*, 421, 741

## Appendix A. Selecting a representative snapshot subsample from a time sequence of 3D hydrodynamical model atmospheres

The 3D hydrodynamical CO<sup>5</sup>BOLD models are computed as time series of 3D structures (snapshots), therefore some time can be saved by selecting a smaller set of snapshots to be used in the spectral line synthesis calculations instead of using the entire simulation run. The snapshots are selected by comparing certain properties of the entire simulation time series and a snapshot sub-sample: effective temperature,  $T_{\text{eff}}$ , and its RMS, vertical velocity,  $v_z$ , and its RMS, residual mass vertical velocity,  $v_{z\text{mass}}$ , all computed as functions of Rosseland optical depth  $\tau_{\text{Ross}}$ . This is usually done manually. We therefore developed a technique which allows to make the snapshot selection in a semi-automatic way. This is done by randomly selecting a number of snapshot combinations to find the snapshot sample with the properties which best match those of the entire model run. This step is carried out with the help of an IDL code *picksnaps*. This technique was used only in selecting snapshot sub-samples used in in Sect. 3, while the other 3D model atmospheres had their snapshots preselected using the same principles by hand.

### General idea

The purpose of the *picksnaps* is to find a snapshot selection (specifically, indexes of snapshots within the entire model sequence), which would represent best the entire simulation run. Automation is implemented via selecting multiple snapshot combinations in a random manner and evaluating how well their averaged properties fit the averaged properties of the entire simulation run. The quality of the fit is found via a figure of merit which is calculated using several fit parameters. The code outputs the paths to snapshots whose selection has the highest quality parameter value and produces graphs that allow the user to directly compare the properties of the trial model selection and those of the entire model sequence. The selection procedure is described in the following section.

### Algorithm

The algorithm can be divided into three main parts: producing the snapshot selections, evaluating the quality parameter for the given selection, and making

graphs for the user to check the results.

Snapshot numbers are divided into groups based on which part of the simulation the snapshots cover and one of them is selected out of every group<sup>3</sup>. Snapshots which are either extreme in their  $v_{z\text{mass}}$  at  $\tau_{\text{Ross}} = 1$  (i.e., with the material moving fastest through the optical surface before decelerating) or are closer in time to neighboring selected snapshot than 1/3 of time interval chosen to set distance in time between the two consequent snapshots in the selected ensemble, are excluded from selection. One set of randomly selected snapshots is further referred to as a trial snapshot sample.

When trial snapshot sample is selected, match parameters are calculated. Match parameters include  $v_{z\text{mass}}$  (mean of the vertical velocity times density divided by the mean density,  $\langle v_z \rho \rangle_z / \langle \rho \rangle_z$ ) and its RMS at  $\tau_{\text{Ross}} = 1; 0.1; 0.001$ ,  $T_{\text{eff}}$  (radiation flux division by Stefan-Boltzmann constant to the power of 0.25,  $\sqrt[4]{F/\sigma_{\text{SB}}}$ ) and its RMS. First, these values are calculated for the entire simulation run and then for every considered trial snapshot sample. For every trial snapshot sample, the absolute differences in the match parameters between those of the entire simulation run and the trial snapshot sample are saved into a temporary array. Then, for every match parameter, an average absolute difference between the entire simulation time series and the trial snapshot sample is saved to have a measure of how good or bad the randomly selected trial snapshot sample is for that parameter. Then, a figure of merit is determined for every trial snapshot sample by evaluating how accurately every match parameter of the snapshot trial sample corresponds the entire time series' match parameter, using for this the average difference between the match parameters:

$$\begin{aligned}
q_i = & \frac{|\langle T_{\text{eff}} \rangle_{\text{all}} - \langle T_{\text{eff}} \rangle_i|}{(\langle T_{\text{eff}} \rangle_{\text{all}} - \langle T_{\text{eff}} \rangle_i)\text{RMS}} - \frac{|T_{\text{eff}}\text{RMS}_{\text{all}} - T_{\text{eff}}\text{RMS}_i|}{(T_{\text{eff}}\text{RMS}_{\text{all}} - T_{\text{eff}}\text{RMS}_i)\text{RMS}} \\
& - \sum_{j=1;0.1;0.001} \frac{|\langle v_{z\text{mass}}(\tau = j) \rangle_{\text{all}} - \langle v_{z\text{mass}}(\tau = j) \rangle_i|}{\langle v_{z\text{mass}}(\tau = j) \rangle_{\text{all}} - \langle v_{z\text{mass}}(\tau = j) \rangle_i}\text{RMS} \\
& - \sum_{j=1;0.1;0.001} \frac{|v_{z\text{mass}}(\tau = j)\text{RMS}_{\text{all}} - v_{z\text{mass}}(\tau = j)\text{RMS}_i|}{(v_{z\text{mass}}(\tau = j)\text{RMS}_{\text{all}} - v_{z\text{mass}}(\tau = j)\text{RMS}_i)\text{RMS}}, \tag{A.1}
\end{aligned}$$

where  $q$  is the figure of merit (0 would indicate a perfect fit, larger values will be

<sup>3</sup>IDL built-in function *randomu* is used as a randomizer.

obtained when the fit is worse),  $i$  is an index of a trial snapshot sample, subscripts under averages and RMS values indicate which set of data was used, RMS without the subscript is calculated over all snapshot trial samples in a single run,  $v_{z\text{mass}}$  is residual mass vertical velocity,  $\tau$  is Rosseland optical depth. The paths to snapshots in the trial sample with the smallest  $q$  are saved as the best fitting trial snapshot sample.

From the first glance, it may appear that parameters associated with  $T_{\text{eff}}$  might be under-weighted compared to  $v_z$ . In fact, this is not the case because properties of  $v_z$  are in general more difficult to reproduce. As an alternative, one can enter  $T_{\text{eff}}$  and  $v_z$  tolerance limits for custom weighing. In this case, all denominators in formula A.1 are replaced by these tolerance parameters and all  $T_{\text{eff}}$  parameters are given the same weight as  $v_z$ . However, using custom weighing is not advised as, typically, it does not give better results than weighing by RMS.

To check how accurately the best trial snapshot sample represents the entire simulation run a few average properties are displayed in a generated output file. Also, plots are made for  $T_{\text{eff}}$  and its RMS,  $T_{\text{eff}}$  histograms,  $v_z$  at  $\tau_{\text{Ross}} = 1$  versus time,  $v_z$ ,  $v_z$  RMS,  $v_{z\text{mass}}$  and  $v_{z\text{mass}}$  RMS versus  $\tau_{\text{Ross}}$ .

## Running the code

The code is called as IDL procedure, meaning that within one line, the name of the procedure (*picksnaps*) is stated and then it is followed by the input parameters separated with commas. An example of a command line to run the code may be:

```
picksnaps, 10.^1.6, 20, './', indexout, /save_data, /copy_ss
```

First input parameter is surface gravity in  $\text{cm/s}^2$ . Second parameter is either a number of snapshots, which will be selected, or an integer array with the indices of preselected snapshots in the subfolder containing *full* files. The latter option is useful when one wants to make plots for a previously or manually made snapshot selection. Third input parameter is a string with a path where model files are located. Last mandatory input parameter is an empty integer array where snapshot indexes of the best snapshot sample will be stored. Optional parameters are:

- "niter" - a number of trial snapshot samples randomly selected in a single run. If not set, 10000 snapshot samples will be selected;
- if both "ttol" and "vtol" are set, snapshot selection is based on custom weighing on these values. "ttol" is  $T_{\text{eff}}$  tolerance in K, "vtol" is  $v_z$  tolerance in km/s;

- adding `"/save_data"` as a parameter saves graphs generated on the screen and `"readme.txt"` with additional information about the model and the snapshot sample in the folder where the code was executed;
- adding `"/copy_ss"` as a parameter copies *full* files of the best trial snapshot selection to a subfolder named `"sel_nss"`, with  $n$  being a number of snapshots within the snapshot sample. If additional data was saved with `"/save_data"`, it is moved to the `"sel_nss"` subfolder;
- if all *mean* files have their corresponding *full* files, `"/quick"` optional parameter can be used to skip loading *full* files for finding their counterpart within *mean* files. This skips the most expensive part of the procedure in terms of the computation time.

## Appendix B. Atomic data for the model atom of lithium

The data we used to construct the updated model atom of Li I are provided in Tables B.1 (Col. 1 – level index, Col. 2 – atomic term configuration, Col. 3 – energy of the level, Col. 4 – statistical weight of the level) and B.2 (Col. 1 – transition index, Cols. 2-3 – indexes of the lower and upper levels of the transitions, Col. 4 – level configurations between which the transition occurs, Col. 5 – vacuum wavelength of the transition, Cols. 6-7 – Einstein coefficients, Col. 8 – oscillator strength). We list atomic parameters of the energy levels and/or transitions, as well as the sources from which the data were taken.

**Table B.1.** Energy levels of the Li I model atom. All data are from the NIST database: [http://physics.nist.gov/PhysRefData/ASD/level\\_form.html](http://physics.nist.gov/PhysRefData/ASD/level_form.html).

Level #	Configuration	Energy [eV]	Statistical weight
1	2s	0.000	2
2	2p	1.848	6
3	3s	3.373	2
4	3p	3.834	6
5	3d	3.879	10
6	4s	4.341	2
7	4p	4.522	6
8	4d	4.541	10
9	4f	4.542	14
10	5s	4.749	2
11	5p	4.837	6
12	5d	4.847	10
13	5f	4.848	14
14	6s	4.958	2
15	6p	5.008	6
16	6d	5.014	10
17	6f	5.014	14
18	7s	5.079	2
19	7p	5.110	6
20	7d	5.114	10
21	8s	5.156	2
22	8p	5.177	6
23	8d	5.179	10
24	9s	5.208	2
25	9p	5.222	6
26	9d	5.224	10

**Table B.2.** Radiative bound-bound transitions of the Li I model atom. Data is taken from the NIST database [http://physics.nist.gov/PhysRefData/ASD/line\\_form.html](http://physics.nist.gov/PhysRefData/ASD/line_form.html).

Transition #	Lower level	Upper level	Transition configuration	$\lambda$ vacuum [Å]	Transition probability		
					$A_{ji}$	$B_{ij}$	$f_{ij}$
1	1	2	2s-2p	6709.7	3.69E+07	8.41E+10	7.47E-01
2	1	4	2s-3p	3233.6	1.00E+06	2.56E+08	4.71E-03
3	1	7	2s-4p	2742.0	1.25E+06	1.94E+08	4.22E-03
4	2	3	2p-3s	8128.6	3.35E+07	1.51E+10	1.10E-01
5	2	5	2p-3d	6105.3	6.86E+07	6.55E+10	6.39E-01
6	2	6	2p-4s	4973.1	1.04E+07	1.07E+09	1.28E-02
7	2	8	2p-4d	4604.1	2.32E+07	9.51E+09	1.23E-01
8	3	4	3s-3p	26887	3.74E+06	5.48E+11	1.22E+00
9	3	7	3s-4p	10795	6.80E+02	6.46E+06	3.56E-05
10	4	8	3p-4d	17550	6.78E+06	1.54E+11	5.22E-01
11	5	7	3d-4p	19281	5.36E+05	5.81E+09	1.79E-02
12	1	11	2s-5p	2563.1	8.87E+05	1.13E+08	2.62E-03
13	1	15	2s-6p	2475.8	5.73E+05	6.57E+07	1.58E-03
14	2	12	2p-5d	4133.7	1.09E+07	3.23E+09	4.65E-02
15	2	14	2p-6s	3986.6	2.59E+06	1.38E+08	2.06E-03
16	2	10	2p-5s	4274.3	4.75E+06	3.11E+08	4.34E-03
17	4	6	3p-4s	24469	7.45E+06	9.16E+10	2.23E-01
18	4	10	3p-5s	13560	2.83E+06	5.92E+09	2.60E-02
19	4	12	3p-5d	12240	3.48E+06	2.68E+10	1.30E-01
20	4	14	3p-6s	11034	1.46E+06	1.65E+09	8.88E-03
21	4	16	3d-5p	10513	1.97E+06	9.60E+09	5.44E-02
22	5	9	3d-4f	18701	1.38E+07	3.18E+11	1.02E+00
23	5	11	3d-5p	12932	2.28E+05	7.45E+08	3.43E-03

Table B.2 continued.

Transition #	Lower level	Upper level	Transition configuration	$\lambda$ vacuum [ $\text{\AA}$ ]	Transition probability		
					$A_{ji}$	$B_{ij}$	$f_{ij}$
24	5	13	3d-5f	12785	4.58E+06	3.37E+10	1.57E-01
25	6	7	4s-4p	68611	7.76E+05	1.89E+12	1.64E+00
26	6	11	4s-5p	24978	3.38E+03	3.98E+08	9.48E-04
27	6	15	4s-6p	18591	1.87E+03	9.07E+07	2.91E-04
28	7	10	4p-5s	54646	2.25E+06	3.08E+11	3.36E-01
29	7	12	4p-5d	38089	1.36E+06	3.15E+11	4.93E-01
30	7	14	4p-6s	28422	9.59E+05	1.85E+10	3.87E-02
31	7	16	4p-6d	25203	8.38E+05	5.63E+10	1.33E-01
32	8	11	4d-5p	41802	2.76E+05	3.04E+10	4.34E-02
33	8	13	4d-5f	40305	2.58E+06	5.95E+11	8.80E-01
34	8	15	4d-6p	26543	1.37E+05	3.87E+09	8.68E-03
35	1	19	2s-7p	2426.2	3.82E+05	4.12E+07	1.01E-03
36	1	22	2s-8p	2395.1	2.66E+05	2.76E+07	6.87E-04
37	1	25	2s-9p	2374.3	1.92E+05	1.94E+07	4.86E-04
38	2	14	2p-6d	3916.4	5.96E+06	3.17E+08	4.73E-03
39	2	18	2p-7s	3836.7	1.56E+06	7.39E+07	1.15E-03
40	2	20	2p-7d	3796.1	3.65E+06	8.37E+08	1.31E-02
41	2	21	2p-8s	3747.7	1.01E+06	4.46E+07	7.09E-04
42	2	23	2p-8d	3722	2.41E+06	3.14E+08	5.02E-03
43	2	26	2p-9d	3672.8	1.68E+06	3.49E+08	5.66E-03
44	3	11	3s-5p	8467.8	4.04E+04	1.85E+08	1.30E-03
45	3	15	3s-6p	7584.5	4.38E+04	1.44E+08	1.13E-03
46	3	19	3s-7p	7137.1	3.60E+04	9.88E+07	8.25E-04
47	3	22	3s-8p	6875	2.79E+04	6.85E+07	5.93E-04
48	4	18	3p-7s	9958	8.62E+05	7.14E+08	4.27E-03
49	4	20	3p-7d	9689	1.23E+06	4.69E+09	2.89E-02
50	4	21	3p-8s	9379	5.54E+05	3.84E+08	2.44E-03
51	4	23	3p-8d	9220	8.09E+05	2.66E+09	1.72E-02

Table B.2 continued.

Transition #	Lower level	Upper level	Transition configuration	$\lambda$ vacuum [Å]	Transition probability		
					$A_{ji}$	$B_{ij}$	$f_{ij}$
52	5	15	3d-6p	10980	1.19E+05	2.38E+08	1.29E-03
53	5	19	3d-7p	10066	7.08E+04	1.09E+08	6.45E-04
54	5	22	3d-8p	9552.4	4.57E+04	6.02E+07	3.75E-04
55	6	19	4s-7p	16115	4.15E+03	1.31E+08	4.85E-04
56	6	22	4s-8p	14838	4.40E+03	1.09E+08	4.36E-04
57	7	18	4p-7s	22230	5.37E+05	4.95E+09	1.33E-02
58	7	20	4p-7d	20934	5.31E+05	2.04E+10	5.81E-02
59	7	21	4p-8s	19541	3.36E+05	2.10E+09	6.41E-03
60	7	23	4p-8d	18862	3.55E+05	9.99E+09	3.16E-02
61	8	9	4d-4f	1.47E+07	6.90E-02	7.68E+11	3.12E-03
62	8	19	4d-7p	21768	7.80E+04	1.22E+09	3.32E-03
63	8	22	4d-8p	19500	4.91E+04	5.50E+08	1.68E-03
64	9	16	4f-6d	26267	2.50E+04	8.15E+08	1.85E-03
65	10	11	5s-5p	1.3965E+05	2.34E+05	4.81E+12	2.05E+00
66	10	15	5s-6p	47816	3.33E+03	2.75E+09	3.42E-03
67	10	22	5s-8p	28968	4.63E+02	8.50E+07	1.75E-04
68	11	12	5p-5d	1.26E+06	4.80E+02	4.03E+12	1.90E-01
69	11	14	5p-6s	1.0287E+05	8.49E+05	7.75E+11	4.49E-01
70	11	16	5p-6d	70335	3.99E+05	5.82E+11	4.93E-01
71	11	18	5p-7s	51221	3.89E+05	4.39E+10	5.10E-02
72	11	20	5p-7d	44824	2.72E+05	1.03E+11	1.37E-01
73	11	21	5p-8s	38887	2.32E+05	1.14E+10	1.75E-02
74	11	23	5p-8d	36288	1.86E+05	3.73E+10	6.12E-02
75	12	13	5d-5f	1.05E+07	6.96E-01	2.85E+12	1.61E-02
76	12	15	5d-6p	77166	1.37E+05	9.51E+10	7.34E-02
77	12	19	5d-7p	47116	7.47E+04	1.18E+10	1.49E-02
78	12	22	5d-8p	37641	4.54E+04	3.66E+09	5.79E-03
79	13	16	5f-6d	75029	4.19E+04	3.18E+10	2.53E-02

Table B.2 continued.

Transition #	Lower level	Upper level	Transition configuration	$\lambda$ vacuum [Å]	Transition probability		
					$A_{ji}$	$B_{ij}$	$f_{ij}$
80	14	15	6s-6p	2.4802E+05	8.88E+04	1.02E+13	2.46E+00
81	14	19	6s-7p	81320	2.17E+03	8.82E+09	6.46E-03
82	15	16	6p-6d	2.15E+06	2.11E+02	8.81E+12	2.44E-01
83	15	18	6p-7s	1.7329E+05	3.74E+05	1.63E+12	5.61E-01
84	15	20	6p-7d	1.1687E+05	1.48E+05	9.91E+11	5.05E-01
85	15	21	6p-8s	83594	1.81E+05	8.87E+10	6.32E-02
86	15	23	6p-8d	72440	1.07E+05	1.71E+11	1.40E-01
87	16	19	6d-7p	1.282E+05	7.08E+04	2.25E+11	1.05E-01
88	16	22	6d-8p	76086	4.16E+04	2.77E+10	2.17E-02
89	18	19	7s-7p	4.0088E+05	3.96E+04	1.93E+13	2.86E+00
90	18	22	7s-8p	1.2760E+05	1.34E+03	2.10E+10	9.81E-03
91	19	20	7p-7d	3.43E+06	9.97E+01	1.69E+13	2.93E-01
92	19	21	7p-8s	2.7045E+05	1.84E+05	3.05E+12	6.73E-01
93	19	23	7p-8d	1.8052E+05	6.38E+04	1.57E+12	5.19E-01
94	20	22	7d-8p	1.9797E+05	3.93E+04	4.60E+11	1.39E-01
95	21	22	8s-8p	6.0779E+05	1.96E+04	3.32E+13	3.26E+00
96	22	23	8p-8d	5.08E+06	5.32E+01	2.94E+13	3.44E-01